Flow-animal interactions in the ocean

Doctoral Dissertation

FLOW-ANIMAL INTERACTIONS IN THE OCEAN

March 2019

Graduate School of Marine Science and Technology
Tokyo University of Marine Science and Technology
Doctoral Course of Applied Marine Environmental Studies

Mamoru Tanaka

Doctoral Dissertation

FLOW-ANIMAL INTERACTIONS IN THE OCEAN

March 2019

Graduate School of Marine Science and Technology
Tokyo University of Marine Science and Technology
Doctoral Course of Applied Marine Environmental Studies

Mamoru Tanaka

Abstract

While marine animals are always exposed to fluid motions, interactions between animals and flows are still controversial. Due to difficulty in measurement, *in situ* observations of animal swimming simultaneously with environmental flow fields are rare. Also, it has been unclear whether animals significantly modify surrounding flow fields. While previous studies have focused on effects of environmental flow field on marine animal (or *vice versa*), in this study, field and laboratory experiments were conducted using novel technologies to investigate "two-way" interactions between flows and animals.

Filed campaigns were conducted to investigate zooplankton avoidance to water disturbance, focusing on diel vertical migration (DVM). DVM of zooplankton has been identified to contribute to vertical flux of carbon in the ocean. While most researchers have worked on mechanism and dynamics of DVM from the view point of biology and/or ecology, several studies have demonstrated that surrounding flow field modify behavior of individual zooplankton (e.g. Seuront et al. 2004). To reveal how zooplankton modify their DVM in response to fluid motions, I analyzed *in situ* data acquired by a cabled observatory that carries a plankton camera (Continuous Plankton Imaging and Classification System, CPICS) and various environmental sensors. The cabled observatory was fixed on the sea floor of 20 m depth near Habu Port at Izu-Oshima Island, Japan. The analysis period was from August 2014 to January 2015. The plankton images were classified at a taxonomic level. The zooplankton taxa were separated into three groups: "strong migrator" (Ostracoda, Mysida, etc.) that appeared only during nighttime, "moderate migrator" (Calanoida, Larvacea, etc.) that appeared at day and night but preferred night, and "non-migrator" (Radiolaria, Aulosphaera) that appeared at day and night evenly. Optical backscatter intensity measured by the turbidity sensor was frequently increased during night throughout the analyzed period, and the nighttime average was over 10-fold higher than that of daytime. Abundance of the strong migrator (individuals L^{-1}) significantly correlated with the optical backscatter intensity ($r^2 = 0.79$, $p < 0.01$), suggesting that the source of the nighttime increases in the optical backscatter intensity was the strong migrator. Hence, I will use the optical backscatter intensity

as a proxy of migrator abundance. Several typhoons passed near the cabled observatory during the analysis period, resulting in increased significant wave height ($H_{1/3}$~4 m at maximum). I compared both the strong migrator abundance and the optical backscatter intensity to orbital velocity induced by the surface gravity wave and found that both were negatively correlated with orbital velocity ($r^2 = 0.32$, $p < 0.01$ and $r^2 = 0.27$, $p < 0.01$, respectively). Since most strong migrator were demersal zooplankton, given the previous studies (e.g. Seuront et al. 2004), the negative correlations suggest that strong migrator actively avoided water disturbances and stayed near the sea floor or in the deeper layers, consequently suppressing their DVM. Additional data that support the main suggestion will be shown in the main text.

To confirm reproducibility of the zooplankton response to surrounding flow field, I analyzed long-term data acquired by two ADCP mooring systems. Filed campaigns were carried out near Izu-Oshima Island and off Eilat, Israel. While the observation site near Izu-Oshima Island has a typical coastal environment in middle latitude, the one off Eilat is in a semi-enclosed gulf (the Gulf of Aqaba) in low latitude where salinity is always >40 PSU throughout the year. Acoustic backscatters were used as a proxy of zooplankton density (Flagg & Smith 1989). Acoustic backscatters during nighttime were significantly higher than that of daytime, suggesting DVM of zooplankton. The nighttime acoustic backscatters were significantly reduced when current velocity increased at the both observational sites, despite the fact that the sites have very different environments. The consistent result from two different locations suggests the generality of the zooplankton avoidance in response to fluid disturbances.

Zooplankton generally display positive phototaxis. Both CPICS and the fluorescence/turbidity sensor carried a light source. To test how zooplankton is attracted by these optic sensors and affect the data, I have conducted tank experiments using a natural zooplankton community and a cultured community composed of nauplius larva of *Artemia salina*. The fluorescence/turbidity sensor was put in an experimental tank with a community. While zooplankton in the both communities were not attracted by the light source of the sensor under room light condition, they are significantly aggregated nearby the light source under dark condition. Altering abundance of the natural community, the effect on the turbidity signal was then tested. The turbidity signal was 1.0 FBU when the abundance was 430 individuals L^{-1}, while the average was 0.1 FBU under the control (without zooplankton). While the turbidity increased to 2.2 FBU when the density was 870

individuals L^{-1}, the turbidity did not show significant increase when the density was altered to 1300 individuals L^{-1}. Second, the effect of environmental flow on the phototactic behavior was tested using the cultured community. While the individuals of *A. salina* are attracted by the light source of the sensor, flows were generated in the tank by stirrers. The flow velocity increased up to 3 cm s^{-1}, and the turbidity data decreased as the individuals hovering around the sensor were flushed away. A significant negative correlation of turbidity against flow velocity was produced by this experiment ($r^2 = 0.40$, $p<0.01$), which was observed by the cabled observatory. Bias due to the phototactic behavior on the *in situ* data is discussed in the main text.

An experimental campaign on fish-generated turbulence was conducted. While organism-generated turbulent mixing (called biomixing) was first time mentioned by Munk (1966) and has been actively discussed for over the last decade, role of biomixing in ocean mixing is still elusive. The most controversial issue is whether organisms can generate turbulent eddies larger than their body size (Visser 2007). To test this issue, several direct observations have been carried out for low-Reynolds-number animals (i.e. zooplankton), but there is no direct observation for high-Reynolds-number animals (i.e. fish). To clarify if fishes can generate turbulent eddies large enough to mix stratified water columns, we conducted an observational experiment in a large aquarium tank containing several thousand Japanese sardines *Sardinops melanostictus*. Turbulence data were collected from inside the sardine school using a turbulence microstructure profiler. While the averaged turbulent kinetic energy dissipation rate was 6.7×10^{-6} W kg^{-1} outside the school, the averaged value inside the school was 2.3×10^{-4} W kg^{-1}: two orders of magnitude higher than typical dissipation rates in the surface mixed layer. The school displayed fast and non-continuous 'avoidance behavior', or fast and long-lasting 'feeding behavior' during the measurements. A noticeable difference between the 2 behaviors was found in turbulent shear spectra: the avoidance behavior spectra showed a power decline in comparison with the Nasmyth empirical spectrum in the inertial sub-range, but the feeding behavior spectra exhibited no power decline, even in the inertial sub-range. In the latter case, the sardine school imparted kinetic energy into scales larger than the average individual body size of 0.173 m. This result is a counter-example to a general hypothesis that swimming organisms cannot impart kinetic energy at scales larger than their individual body size. Ecological significance of the flow-animal interactions is discussed with the results from this study and previous studies.

Acknowledgements

I would like to express my heartfelt thanks to my supervisor Prof Hidekatsu Yamazaki who guided me throughout my PhD and provided invaluable support. I also would like to express my deep appreciation to my advisor Prof Takeyoshi Nagai for his invaluable support since my graduate years.

I gratefully acknowledge Prof Yoshinari Endo and his student Mr. Ryuta Murashige at Tohoku University for manual classification for microscopic plankton (Chapter 2). I would like to express my appreciation to Prof Gregory N. Ivey for his insightful comments for turbulence estimation in Chapters 2 and 3. I am grateful to Prof Amatzia Genin who provided the observation data in Israel (Chapter 3), and his insightful comments are appreciated. I would like to thank Prof J. Rudi Strickler and Prof Rubens M. Lopes who designed the experimental setup (Chapter 4). I am indebted to Dr Tomonari Okada who provided the instrument TM9 and to Yokohama Hakkeijima Inc. who provided a chance to conduct an experiment in the aquarium tank (Chapter 5).

Also, I would like to express my sincere gratitude to Mr. Kunihisa Yamaguchi and all members of Tokyo Metropolitan Government for their positive attitudes and grateful supports through out of my research. Many thanks to Dr Scott Gallager and all members of Coastal Ocean Vision who designed the cabled observatory. Also, many thanks to Mr. Koichi Toda, Mr. Junki Uehara and all divers & local fishermen who worked on deployment and maintenance of the cabled observatory. I am really indebted to all members at Laboratory of Ocean Ecosystem Dynamics: Akiko Takano, Yusaku Kokubu, Hikaru Homma, Eiji Masunaga, Hirokazu Iimura, Yosuke Sagara, Marika Takeuchi, Yuka Saito, Mie Akada, Nagisa Tachikawa, Miwa Iwamura, Miho Yatsunami, Masako Iwasa who helped me in so many situations.

A very special thanks to Lynn L. Allmon for her support, cooperation, encouragement, and love at all times. I want to extend my sincere gratitude to my parents, my brother, Takky (Dec 14th 2017 RIP), and my friends for their encouragement to continue this work. Fund for this work was supported by JST CREST Grant Number JPMJCR12A6.

Contents

Chapter 1

Introduction

1.1 Flows acting on animals

While marine animals are always exposed to fluid motions, interactions between animals and flows are still controversial. Due to difficulty in measurement, there are only a few studies that simultaneously observed zooplankton dynamics and surrounding flow fields in the ocean, while zooplankton has significant roles in the material cycle. (Steinberg & Landry 2017). I will examine the significance of the study on the zooplankton reaction to surrounding flow fields based on previous studies (e.g. Kiørboe 2008, Yamazaki & Squires 1996, Oakey & Elliott 1982).

While the biomass of the marine biosphere is concentrated in the upper 200 m (Katija 2012), flows are ubiquitous in the ocean at any temporal and spatial scales. Thermohaline circulation is the largest circulation in the ocean (Wunsch 2002) and greatly affects the biogeochemical cycle (Sarmiento & Gruber 2006). The Western boundary currents are accompanied by various mesoscale and submesoscale phenomena, inducing strong gradients in temperature, salinity, and nutrients (Capet et al. 2008). The combination of surface tides and bottom topography generates internal tides that induce vertical displacement of pycnocline whose amplitude reaches 100 m (McPhee-Shaw et al. 2004). Kinetic energy of the dynamics shown above are finally converted into turbulent kinetic energy by boundary frictions, shear stresses, wave breakings, and hydraulic jumps (Thorpe 2007).

Zooplankton cannot swim against large-scale flows like the Western boundary currents, but they can sense local flow fields induced by small-scale turbulence. Kiørboe (2013) reported mechanosensory setae on copepod's antennules (Fig. 1.1 left), and copepods seem to distinguish deformation, vorticity, and acceleration of surrounding water using the setae (Fig. 1.1 right, Kiørboe 2008).

Similar organs have been found on antennules of North Atlantic krill as well (Patria & Wiese 2004).

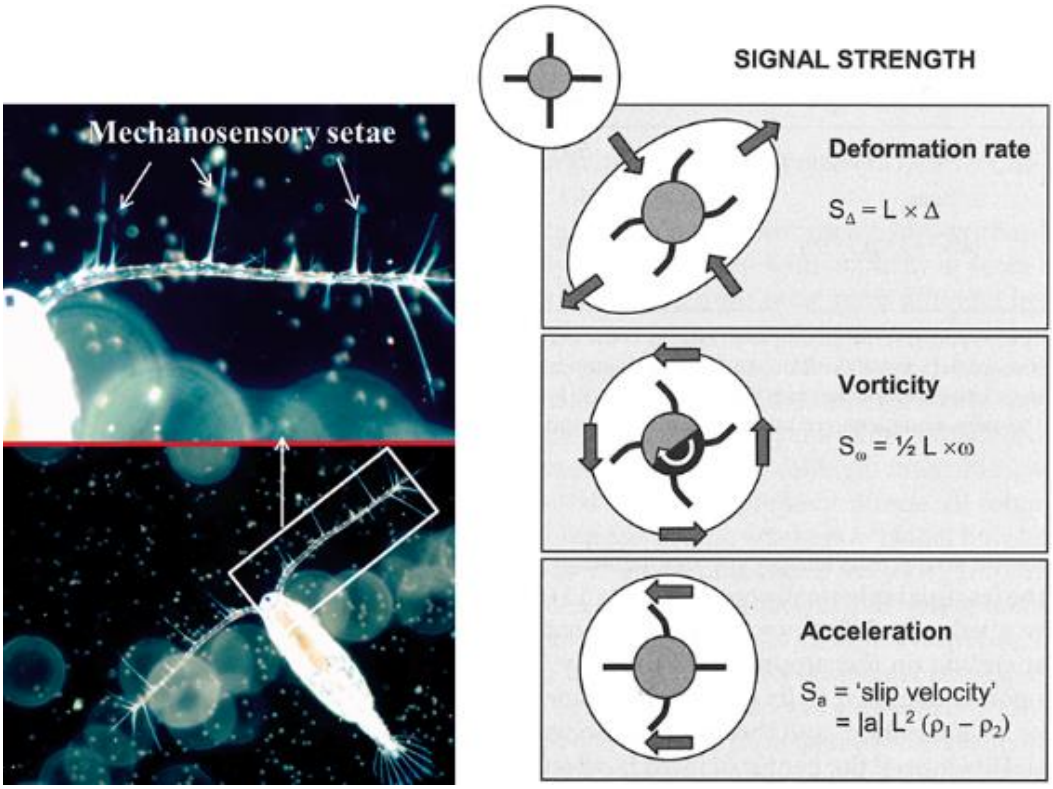

Fig. 1.1: (Left) Mechanosensory setae on the antennules of a copepod species, *Pseudocalanus elongates*. Excerpted from Kiørboe (2013). (Right) Schematic of spherical copepod with extending setae in different flow environments. Excerpted from Kiørboe (2008).

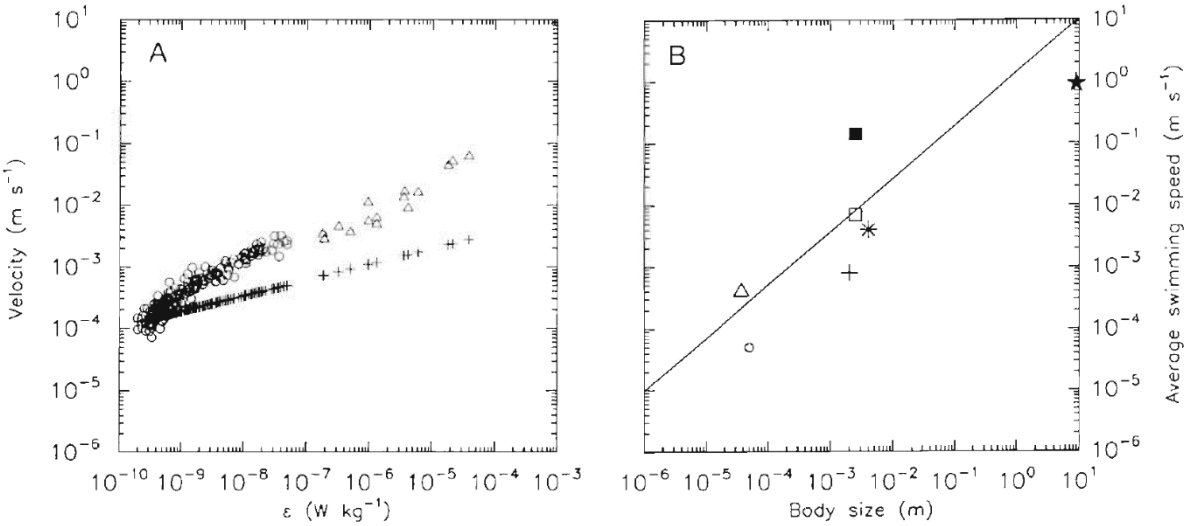

Fig. 1.2: (A) Kolmogorov velocity scale (+) and the rms turbulent velocity scale against observed dissipation rates (ε). (○) Samples from a seasonal thermocline; (△) those from turbulence observed in fjord. (B) Average swimming speed of various organisms against body size. Shown are 2 phytoplankton (△, *Gyrodinium dorsum*; ○, diatom), 3 zooplankton (□, *Euchaeta rimana*; +, *Oithona davisae*; ∗, *Metridia pacifica*) and ★, a shark. (■) Escaping swimming speed for *E. rimana*. Excerpted from Yamazaki & Squires (1996).

As reported by Yamazaki & Squires (1996) who compared zooplankton swimming speeds with turbulent flow speeds and concluded that most zooplankton can swim independently from local turbulence (Fig. 1.2), several field studies have shown modified zooplankton distribution in response to hydraulic dynamics (Gallager et al. 2004, McManus et al. 2005). Gallager et al. (2004) deployed a 3-dimensional Video Plankton Recorder (VPR) with CTD at Georges Bank and showed that zooplankton significantly aggregated only when the motility number (ratio of plankton swimming speed to rms turbulent velocity) was greater than 3. A consistent result with Gallager et al. (2004) was found in a coastal region in Monterey Bay by McManus et al. (2005). They measured current velocity and acoustic backscatter with thermistor chains and found that zooplankton thin layers (indicated by acoustic backscatter) were formed only when Ri > 0.25 and oscillated vertically following vertical displacements of thermocline caused by internal gravity waves. In addition, Seuront et al. (2004) conducted a tank experiment to study zooplankton behavioral response to turbulence. They put zooplankton into a rectangular tank that is 1 m in

length, where a horizontal turbulent gradient was generated by oscillating a grid located at an end. They tracked individual zooplankton swimming passes and found that zooplankton actively escaped from high turbulent levels and moved toward lower turbulent regions. Given the results from Yamazaki & Squires (1996) and Seuront et al. (2004), the zooplankton aggregations observed by Gallager et al. (2004) and McManus et al. (2005) seem to be consequences of zooplankton's active migration toward less turbulent regions.

Why do zooplankton avoid high turbulent levels? Turbulence generally increases encounter rates of zooplankton with their prey (phytoplankton) and predator (fish larva) (Rothschild & Osborn 1988, Yamazaki et al. 1991, MacKenzie & Kiørboe 2000). To examine how turbulence affects zooplankton's Darwinian fitness (ability to reproduce the next generation; such as growth rate, survival rate), Visser et al. (2009) combined zooplankton's feeding manner (suspension, ambush, and cruise feeding), cost of swimming, prey capture rate, and predation risk with a physical model where environmental turbulent level was controlled. The results from the model suggested that behaviors that seek out low turbulent levels increase individual's Darwinian fitness for most zooplankton, and this effect is especially remarkable for the cruising feeders who swim throughout the water to find out prey. Thus, at high turbulent levels, disadvantageous aspects (e.g. predation risk) seem to exceed advantageous aspects (e.g. feeding efficiency).

While Visser et al. (2009) did not consider motility of prey (phytoplankton), a recent experimental work reported a behavioral response of motile phytoplankton cells (*Heterosigma akashiwo*) to turbulence. Sengupta et al. (2017) put the phytoplankton cells into small cylinders (10 mm in length) and flipped the cylinders with a period of 18 s to mimic Kolmogorov-scale eddies corresponding to a turbulent kinetic energy dissipation rate of $\varepsilon = 3 \times 10^{-8}\ \mathrm{W\ kg^{-1}}$. They found that a significant portion of the cells rapidly changed their morphology after the flips (within 60 min), and consequently their swimming direction was altered from upward to downward, resulting in significant cell accumulations at the lower end of the cylinder. They argued that motile phytoplankton cells actively avoid highly turbulent layers. Given that turbulence enhance encounter rates with zooplankton (Yamazaki et al. 1991), the turbulence-avoidance strategy of motile phytoplankton cell is reasonable to survive in the ocean.

According to the previous studies mentioned above, an individual-based zooplankton strategy would be inferred as follows: individual zooplankton can detect surrounding local flow fields (Kiørboe 2008), can swim independently from the flow

fields (Yamazaki & Squires 1996), and select layers with low turbulent levels (Gallager et al. 2004, McManus et al. 2005) to enhance individual's opportunity to reproduction (Visser et al. 2009). Zooplankton has significant roles in the material cycle: they transport carbon between surface layers and deep layers as part of the biological pump (Steinberg & Landry 2017). The carbon transport is mediated by two pathways: 1) particle sinking and 2) diel vertical migration (DVM) (Steinberg & Landry 2017). Zooplankton egest carbon as fecal pellets that are more difficult to be decomposed by bacteria and sink downward faster (tens to hundreds of meters per day for copepods) than other forms, such as marine aggregates (Steinberg & Landry 2017). Thus, the particle sinking has been considered as an important contributor of downward carbon flux for over several decades (Cherry et al. 1978). In contrast to the particle sinking, DVM is recently recognized as an important pathway of carbon transport (Brierley 2014). The most frequently observed pattern of DVM is that, after dusk, zooplankton swim up from deep layers to surface layers and swim down again toward deep layers before dawn (Brierley 2014). Zooplankton graze phytoplankton in the surface layers during nighttime, and the ingested carbon is respired as CO_2, excreted as dissolved organic carbon (urine), egest as particulate organic carbon (fecal pellet) in the deep layers during daytime. This daily active migration results in downward flux of carbon (Steinberg & Landry 2017). The mortality of the migrators in the deep layers is an additional flux (Zhang & Dam 1997, Al-Mutairi & Landry 2001). Observed downward flux due to DVM was up to 41 mg C m^{-2} d^{-1} in the northwestern North Atlantic (Dam et al. 1995) and up to 47 mg C m^{-2} d^{-1} in the northeastern North Pacific (Stukel et al. 2013) that are comparable to that by particle sinking (Sanders et al. 2014).

While zooplankton provide the pathways of carbon as results of their concurrent actions, there is no study that demonstrates (even discusses) how physics (flows) affect the efficiency of the transports. Since DVM consists of individual's active swimming, it is predictable that the pathway by DVM is more easily affected by local flow fields than that by particle sinking. In the interior of the open ocean, away from the boundaries, turbulent kinetic energy (TKE) dissipation rates vary from 10^{-10} to 10^{-7} W kg^{-1} (Thorpe 2005), while strong turbulence of 10^{-6} W kg^{-1} is observed inside surface mixed layer (Oakey & Elliott 1982, Shay & Gregg 1986). Mixed layer depth (MLD) in middle latitude is ~10 m in summer season and reaches 100 m in winter season. Typhoons also increase MLD. Price et al. (1978) reported that storms with wind speeds above 10 m s^{-1} increased MLD by several 10 m in summer season. During night-time, zooplankton would stay in the surface layers

shallower than 50 m (Rousseau et al. 2010) where the water column is easily disturbed by the atmospheric events.

1.2 Animals acting on flows

While zooplankton seem to be affected by local flow fields, recent studies have proposed a concept that swimming marine animals, zooplankton, fish, as well as cetacean, would physically mix the ocean by inducing turbulent flows and vertical convection through drag force while swimming (Katija 2012). Although there are still discussions on the efficiency of the turbulence induced by animals on the mixing (Visser 2007), I will use a term "biologically-induced turbulence" for the turbulence and "biomixing" for the subsequent mixing in this study.

Munk (1966) introduced the concept of biomixing. While he concluded that the biologically-induced turbulence has a negligible contribution to the ocean mixing, Dewar et al. (2006) presented the opposite conclusion. They performed comprehensive calculations on energy budgets stored in the marine biosphere based on observed data that showed more biologically induced flows in the abyssal ocean than Munk (1966) assumed. They estimated that 1% of the total chemical power stored in the marine biosphere (62.7 TW) is converted into mechanical energy which would be used as turbulent mixing. Also, Huntley & Zhou (2004) calculated drag force on body surface of various animals (from zooplankton to cetaceans) to estimate turbulent intensity while swimming at their moderate speeds. Taking account of packing density inside schools or swarms, Huntley & Zhou (2004) estimated that turbulent kinetic energy dissipation rates were in the order of 10^{-5} W kg^{-1}, regardless of body size, which is comparable to that measured in well-mixed surface layers (Thorpe 2007).

Besides the theoretical estimates of Dewar et al. (2006) and Huntley & Zhou (2004), an observational evidence of biomixing has been reported by Kunze et al. (2006). They encountered high turbulent kinetic energy dissipation rates of 10^{-5} to 10^{-4} W kg^{-1} in layers of upward swimming krill during their DVM in Saanich Inlet, Canada (Fig. 1.3 left). Gregg & Horne (2009) also measured elevated turbulent kinetic energy dissipation rates of 10^{-6} to 10^{-5} W kg^{-1} compared to the background value of 10^{-9} W kg^{-1} within schools composed mainly of anchovy in Monterey Bay, USA. These measured turbulent kinetic energy dissipation rates are comparable to the theoretical value of 10^{-5} W kg^{-1} estimated by Huntley & Zhou (2004). Experimental works by Catton et al. (2011) and Patria & Wiese (2004) agreed with Kunze et al. (2006). Catton et al. (2011) conducted small tank experiments to study

fluid motions due to free swimming krill using a laser sheet illumination. They reported that krill aggregations actively transported water parcels downward to successive group members (Fig. 1.3 right), consequently disturbing the water column at a scale of aggregations. Patria & Wiese (2004) also showed induced jets and vortexes behind tethered individual krill (~45 mm in body length) that were paddling their pleopods. Observed flow speeds reached almost 10 cm s^{-1}. Noss & Lorke (2012) conducted a tank experiment to study turbulence and subsequent vertical eddy diffusivity induced by *Daphnia*. Observed turbulent kinetic energy dissipation rates and diffusion coefficients were 10^{-6} W kg^{-1} and 10^{-5} m^2 s^{-1} respectively, and both values were valid for a volume of approximately 1 cm^3, about two orders of magnitude larger than the individual body volume. Wilhelmus & Dabiri (2014) conducted a tank experiment to study fluid motion around individuals of upward swimming *Artemia salina*. They found that downward jets generated by swimming strokes triggered Kelvin-Helmholtz instabilities larger than individual body size.

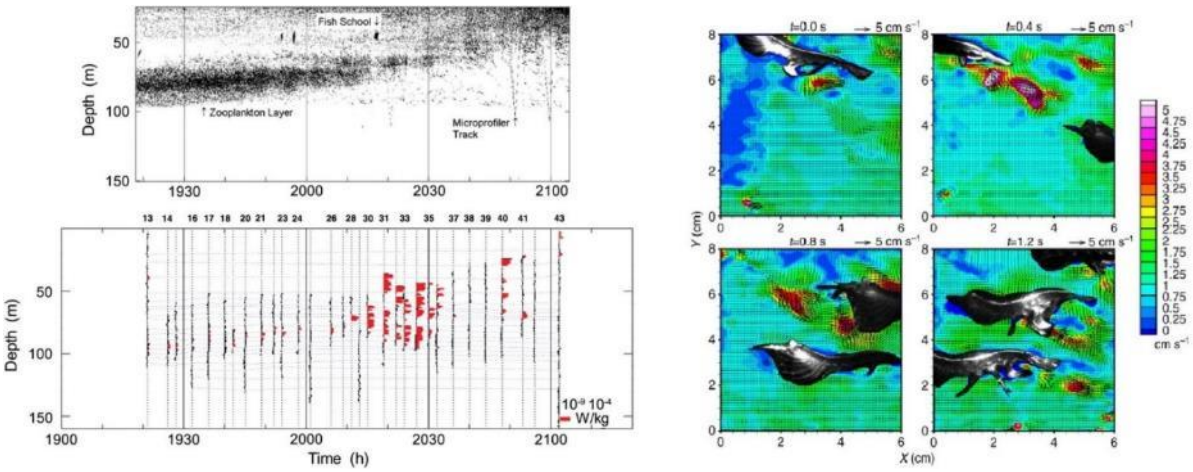

Fig. 1.3: Top left panel shows a nighttime ascent of a krill aggregation observed by an echo sounder. Bottom left panel shows turbulent kinetic energy dissipation rates that seem generated by the krill ascent. Right panels show a flow field generated by a krill aggregation swimming in a tank that was measured by particle image velocimetry. The krill aggregation significantly disturbed the water in the tank, indicating that krill aggregations induce strong turbulent mixing in the ocean like the one shown in the left panels. The left panels were excerpted from Kunze et al. (2006), and the right panels were excerpted from Catton et al. (2011).

While some observational and experimental studies demonstrated the importance of biologically-induced turbulence, some studies contradicted these conclusions. Visser (2007), based on a theoretical approach, pointed out that, even if small animals such as zooplankton induce turbulent flows during their migrations, they scarcely contribute to the ocean mixing since the induced turbulent eddies are too small to significantly disturb the water. His hypothesis was that swimming animals cannot impart kinetic energy at scales larger than their individual body size. As predicted by Visser (2007), Gregg & Horne (2009) reported that vertical eddy diffusivity inside anchovy schools were 100 times smaller than that outside the schools while turbulent kinetic energy dissipation rates were significantly elevated inside the schools. Also, Rousseau et al. (2010) reported an averaged turbulent kinetic energy dissipation rates of 10^{-8} W kg^{-1} within krill layers, a dissipation rate higher by a factor of two than the averaged background value, but three orders of magnitude lower than the theoretical 10^{-5} W kg^{-1} predicted by Huntley & Zhou (2004). Sato et al. (2014) reported no correlation between turbulent kinetic energy dissipation rates and krill DVM based on a long-term data set observed from a cabled observatory (VENUS).

As small animals induce low-Reynolds-number flows, and large animals generate high-Reynolds-number ones (Kunze 2011, 2019), an animal which has a different body size would have a different mechanism to modify flow patterns. Small swimmers have been frequently studied from field campaigns (Simoncelli et al. 2018, Sato et al. 2014, Rousseau et al. 2010, Katija & Dabiri 2009, Kunze et al. 2006) as well as experimental campaigns (Houghton et al. 2018, Wilhelmus & Dabiri 2014, Catton et al. 2011). This relatively large number of studies may depend on accessibility of living body or facility (i.e. small tank). Large swimmers, such as pelagic fish, have been rarely studied. Pujiana et al. (2015) and Gregg & Horne (2009) are the only studies who reported biomixing by marine fish school in detail. Acoustics were utilized to detect/infer the presence of fish school during the measurements for their studies, while the schools seemed to be composed of anchovy (Gregg & Horne 2009) or tuna (Pujiana et al. 2015). Since acoustics does not identify animal behaviors, density, and possible reactions to the sensor during the measurements, a laboratory experiment is desirable to study the relationship between fish behavior and biomixing. As a next step for studying biomixing due to pelagic fish, I will present a direct measurement of biomixing by sardine in an experimental tank in which direct observations of fish behaviors can be conducted.

1.3 Layout of the dissertation

The purpose of this dissertation is 1) to enhance our knowledge regarding how animals are affected by surrounding flow patterns and how animals affect local flow patterns and 2) to summarize the flow-animal interactions in the sense of that "marine animals and surrounding flow fields affect each other" based on results from previous studies and this study.

Chapter 2 presents results from a long-term and continuous data acquired by a cabled observatory deployed near the southern part of Izu-Oshima Island. The cabled observatory carried an in situ microscopic camera and environmental sensors. Observed zooplankton were grouped into "migrator" who appeared only during night-time and "non-migrator" who appeared with no time preference, and the appearance of both taxa significantly decreased with increasing orbital velocity induced by surface gravity wave, suggesting zooplankton's active avoidance to surrounding flow fields.

Chapter 3 presents results from long-term and continuous data acquired by ADCPs moored near the northern part of Izu-Oshima Island and in the Gulf of Aqaba at the northern tip of the Red Sea, where acoustic backscatter intensity recorded by the ADCPs is used as a proxy of zooplankton density. While the acoustic backscatter intensity frequently increased during night-time (suggesting zooplankton DVM), the nighttime acoustic backscatter intensity significantly decreased when flow velocity increased. This trend was found in the both observation sites, although the two observation sites are separated spatially and environmentally.

In Chapter 4, I carried out a tank experiment to test how zooplankton is attracted by light emissions from the optic sensors (i.e. the microscopic camera, the turbidity sensor) used for the cabled observatory and how zooplankton's phototaxis would bias the data. In a small experimental tank that contained an optic sensor, zooplankton individuals are attracted by the light emissions, and the data from the both sensors increased with increasing abundance in the detection volumes of the sensors.

Chapter 5 shows results from a large tank experiment to test biomixing by a school of Japanese sardine. The experiment was carried out in an aquarium, Yokohama Hakkeijima Sea Paradise, that contained several thousand sardines. I used an upward microstructure profiler to measure turbulence near the surface. The averaged turbulent kinetic energy dissipation rate was 2.3×10^{-4} W kg^{-1} inside the school, while that outside the school was 6.7×10^{-6} W kg^{-1}. Also, based on spectrum analysis on the measured turbulent shear, I suggest that sardine school can generate

turbulent eddies that are larger than individual sardine (>1 m), during feeding phase. Chapter 6 summarizes the results from this study and previous studies, proposing ecological implications from the results, and giving perspective and outlook.

Chapter 2

Flow-mediated DVM observed from a cabled observatory

2.1 Introduction

Since diel vertical migration (DVM) of zooplankton has recently been suggested to contribute vertical flux of carbon as part of biological pump (Steinberg & Landry 2017), comprehensive investigation on mechanism and dynamics of DVM is necessary to predict distribution and flux of carbon in the future. According to observational studies (Gallager et al. 2004, McManus et al. 2005), experimental studies (Seuront et al. 2004), and numerous model studies (Visser et al. 2009), most zooplankton in the ocean seem to avoid high turbulent levels. The consistent conclusions among the studies raise the hypothesis of the turbulence-avoidance strategy of zooplankton.

Several studies such as Gallager et al. (2004) and McManus et al. (2005) already have observed zooplankton distributions that were modified by local fluid dynamics in the ocean. However, results from these studies have yet to be verified to answer how local flow fields alter DVM of zooplankton. Gallager et al. (2004) reported that zooplankton significantly aggregated only when the motility number (ratio of plankton swimming speed to rms turbulent velocity) was greater than 3. Also, McManus et al. (2005) made use of acoustic backscatter intensity acquired by moored ADCPs as proxy of zooplankton density. While there are other studies that reported significant correlations between zooplankton dynamics and local flow fields (e.g. Lienesch & Matthews 2000, Grossmann et al. 2014, Shanks et al. 2015), almost no study has discussed the correlations with regard to DVM. Only Bonicelli et al. (2016) found a negative correlation between magnitude of DVM performed by

barnacle larva and significant wave height. In this chapter, I will show an additional data set supporting the hypothesis of the turbulence-avoidance strategy of zooplankton and will suggest the observed DVM was significantly suppressed as results of the strategy. The observed data is the first evidence that zooplankton DVM is directly suppressed by local flow fields.

2.2 Materials and methods

2.2.1 Location

The observation site is in a coastal area of an isolated island, Izu-Oshima Island in Japan (Fig. 2.1), where current is greatly affected by internal gravity waves (Masunaga et al. 2017). The island is about 30 km away from mainland Japan, and there is no river on the island.

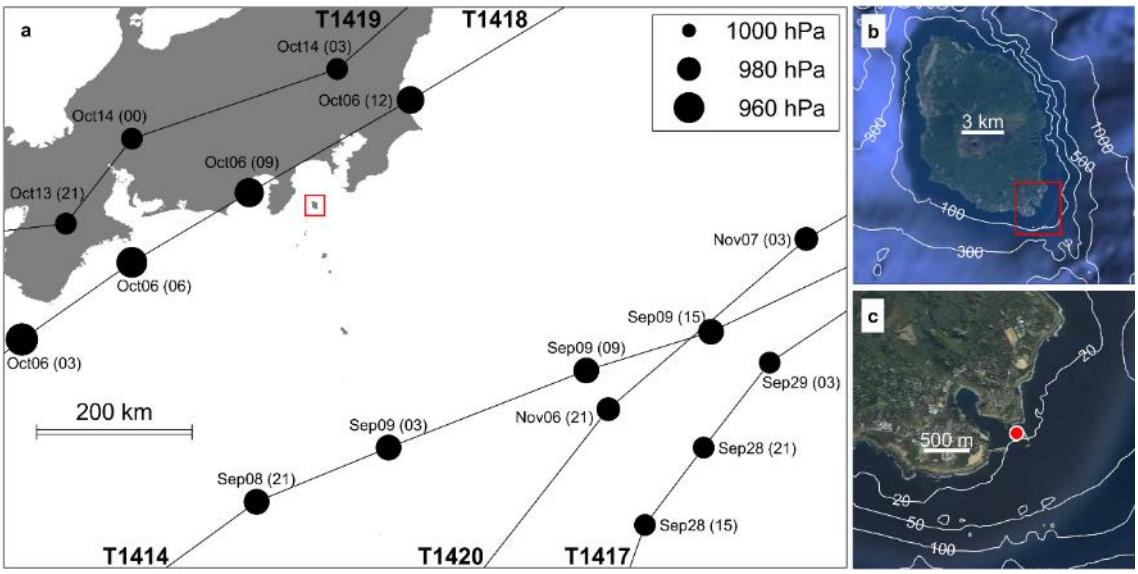

Fig. 2.1. Observation site. (a) Regional map around the observation site. Red frame denotes the location of Izu-Oshima Island. Black lines denote tracks of the typhoons, named as T1414, T1417, T1418, T1419, and T1420, that occurred during the full observation period. Filled circles show air pressure at day shown near each circle where time is in brackets, where larger circles suggest stronger typhoons (lower pressure). (b) Overall picture of the island. (c) Red-filled circle (34° 40' 58.5" N, 139° 26' 39.7" S) denotes the location of the cabled observatory. A small bay near the red-filled circle is a fishing harbor, Habu Port.

2.2.2 Cabled observatory

A cabled observatory (Oshima Coastal Environmental data Acquisition Network System, OCEANS) (Fig. 2.2a) was deployed on Aug. 12th, 2014 at the observation site (Fig. 2.1c). The cabled observatory is fixed on an x-shaped block (~1 m in height), where the bottom depth is about 20 m (Fig. 2.2b). The cabled observatory is connected to a computer cluster in a shore lab by an armored cable composed of power-supply wires and data-transfer optical fibers. The shore lab was provided by the Tokyo Metropolitan Government and located in Habu Port (Fig. 2.1c). Biological, physical, and chemical sensors (Table 2.1) are attached on mounting frame or deployed nearby (Fig. 2.2b). A plankton camera, (Continuous Plankton Imaging and Classification System, CPICS, CoastalOceanVision, Inc.; Fig. 2.3), was used to obtain plankton images at a high resolution. CPICS took images of plankton which passed inside image volume of 11.0 × 15.0 × 2.0 mm^3 (Fig. 2.3b) with a pixel resolution of 6.19 μm $pixel^{-1}$. Shutter frequency was set to 3 Hz, and thus hourly sampling volume was 3.56 L. Reduced flash exposure time of 10 μs allowed for taking unblurred images even under rough conditions (e.g. during storms).

Sensors that are sensitive to biofouling (such as the chlorophyll/turbidity sensor, the PAR sensor, the electrical conductivity sensor (the CT sensor), the SUNA, and the DO sensor; Table 2.1) had a self-cleaning brush or wiper that worked every hour (Fig. 2.4b). In addition, the entire system was cleaned up by professional divers twice (once) a month in the summer (winter) season. Sampling volume for the Vector was located at roughly the same position as the image volume of the CPICS (Fig. 2.3b) to measure flow patterns experienced by plankton. Acoustic frequency of the Aquadopp was 400 kHz, and it has 3 acoustic beams whose beam axes were tilted with an angle of 25 degrees from the body axis (Fig. 2.2b). Number of bins was set to 20, bin size was 1 m, and blanking distance was 1 m to cover the entire water column. As the acoustic transducers were located 1 MAB (meters above the bottom), the 1st layer from the Aquadopp covers 2 to 3 MAB. After Oct. 19th, 2014, the bin size was set to 2.5 m because of human error. For the sake of easy visualization, the data acquired from the 2.5-m bins was interpolated to the 1-m bins. The fluorescence/turbidity sensor emits blue light (340 nm) in order to measure fluorescence, and infrared light (880 nm) was used to measure turbidity (Fig. 2.4). Optical backscattering strength was originally measured as voltage, calibrated by sodium fluorescein and formazin solution to ensure fluorescence and turbidity.

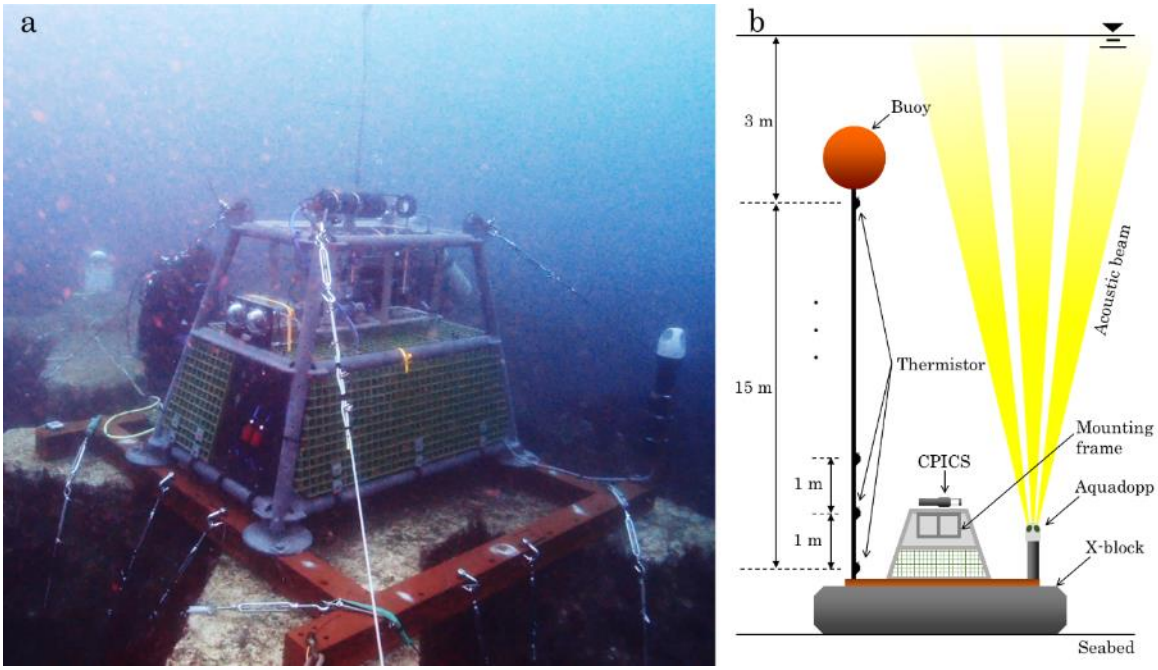

Fig. 2.2. Cabled observatory (OCEANS). (a) Underwater photo taken after the deployment on Aug. 12th, 2014. The dimensions of the cabled observatory are 180 x 120 x 145 cm (width x height x depth). (b) Schematic of the cabled observatory. Sensors are attached on the mounting frame except the Aquadopp and the thermistor chain (Table 2.1). The thermistor chain has 16 thermistors with a 1-m interval. The Aquadopp has 3 acoustic transducers. The schematic is not in scale.

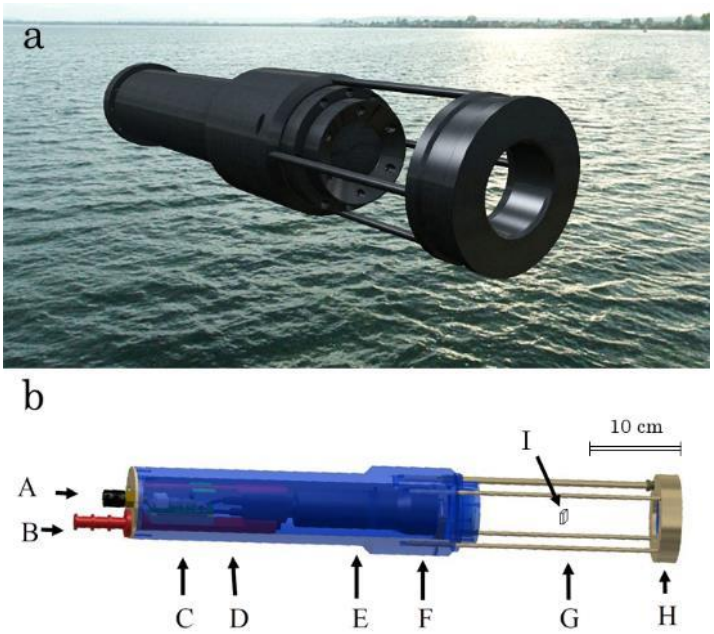

Fig. 2.3. The plankton camera, CPICS. (a) External appearance of the CPICS. (b) Internal structure of the CPICS; (A) Connectors for ethernet, RS232, and power (12–24 VDC), (B) internal cooling to eliminate overheating, (C) multi-core processor, (D) 6 mega pixels color machine vision camera, (E) 0.9 to 10 x telecentric lens, (F) delrin and titanium housing, (G) open flow (1.5 L volume) to image fragile organisms, (H) custom darkfield LED array, and (I) image volume (not in scale).

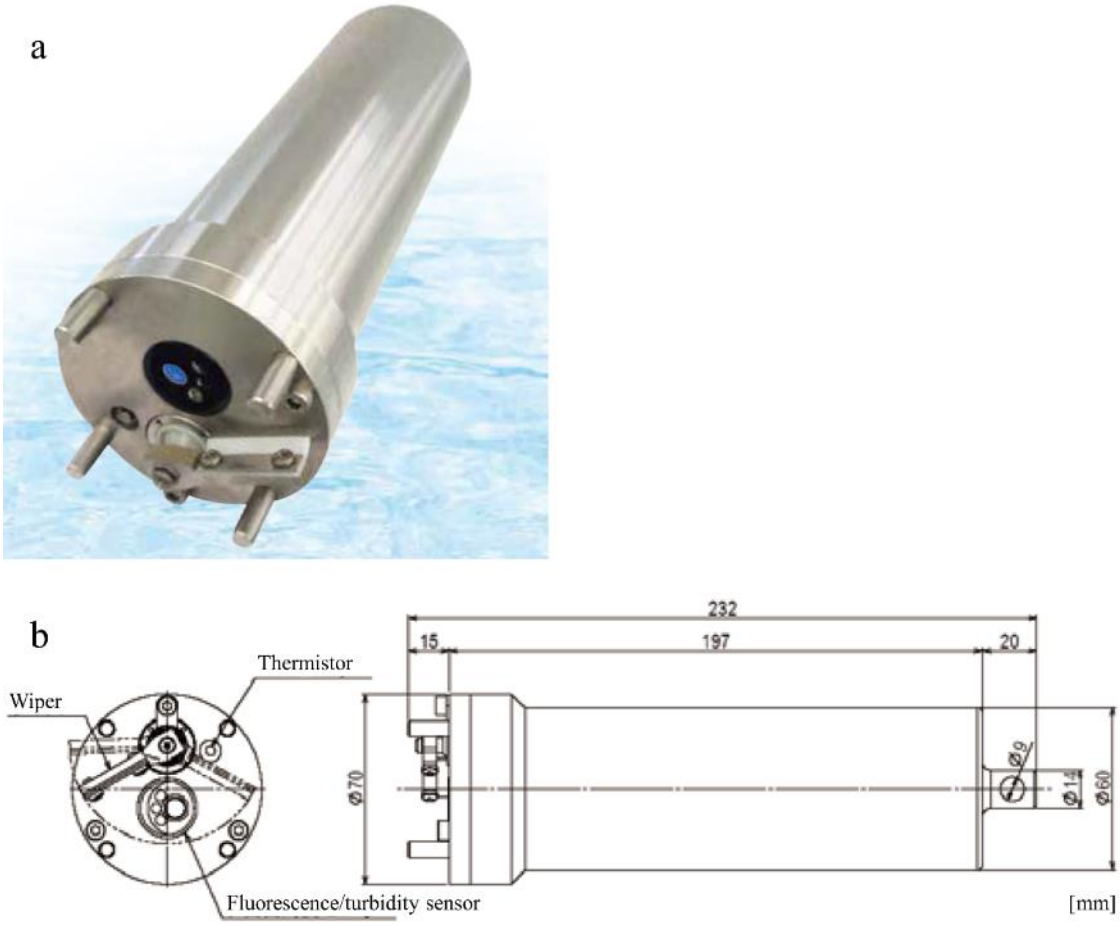

Fig. 2.4. The turbidity/fluorescence sensor. The photos are from the manufacture's website (http://www.jfe-advantech.co.jp/).

Table 2.1. List of sensors mounted on the cabled observatory (OCEANS). The Aquadopp and the thermistor chain are deployed nearby the cabled observatory, while the other sensors are attached on the mounting frame (Fig. 2.2).

Sensor	Object	Unit	Sample rate
Biological			
CPICS	Plankton	Individual(s)	6 Hz (shutter frequency)
Fluorescence/turbidity sensor	Fluorescence	a.u.	1 Hz
”	Turbidity	FBU	”
Physical			
Pressure sensor	Pressure	dbar	1 Hz
Vector	Current	m s^{-1}	8 Hz
Aquadopp	Current (vertical distribution)	m s^{-1}	60 sec
”	Acoustic backscatter (vertical distribution)	counts	”
PAR sensor	PAR	μM s^{-1} m^{-2}	1 Hz
CT sensor	Temperature	deg C	1 Hz
”	Salinity	PSU	”
Thermistor chain	Temperature (vertical distribution)	deg C	1 Hz
Chemical			
SUNA	Nitrate	μM L^{-1}	5 min
DO sensor	DO	mg L^{-1}	1 Hz

2.2.3 Data process and analysis

Plankton images

In-focus objects in the image volume (Fig. 2.3b) were automatically detected by the CPICS software (Fig. 2.5). For the detections, the intensity threshold was set to 1.50, the area threshold was 200 pix^2 which corresponds to a circle of 100 μm in diameter, and the focus threshold was 0.50. Each detected object was automatically extracted into a small image called Region Of Interest (ROI) (Fig. 2.5). The objects were manually identified to taxon level (including both living and non-living). Due to the limited manpower, the identification was done only for the data acquired from September 20th to October 30th. This period was selected in order to include due to storm events (Fig. 2.1a).

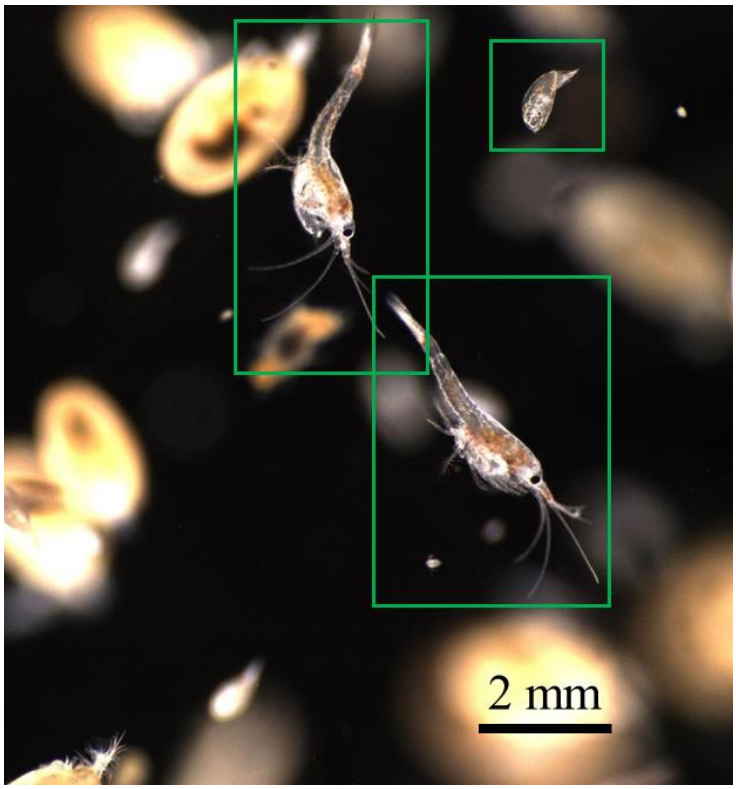

Fig. 2.5. Detection of the ROIs. The green frames indicate the ROIs. The scale bar indicates 2 mm. This underwater microscopic photo was taken on August 18th 20:44 after sunset.

Turbidity data

Optical scattering strength calibrated by formazin solution is generally used as a proxy of turbidity of the water, and the unit is FTU (formazin turbidity unit). However, several turbidity units have been proposed to distinguish directions of optical scattering (i.e. backscatter, side scatter, and forward scatter) (Turbidity -- Units of Measurement, https://or.water.usgs.gov/grapher/fnu.html). Since the sensor receives backscatter of the infrared light by suspended solid, FBU (formazin backscatter unit) is applied in this study. In addition, the measured turbidity reflected presence of zooplankton rather than "turbidity" of the water (see 2.3 Results). Hence, I use the term "optical backscatter" that expresses directly what the sensor actually sensed.

The optical backscatter often showed clipping data: the measured value exceeded the upper detection limit of 1300 FBU. Continuous clipping data for over 10 s (probably caused by drifting seaweeds stuck on the cabled observatory) was replaced by not-a-number (NaN).

Stratification

To ensure vertical distribution of seawater density, first I estimated vertical distribution of salinity. The CT sensor that was attached on the mounting frame of the cabled observatory measured temperature and conductivity simultaneously. Although salinity is independent from temperature, a linear relationship between salinity and temperature was found for a short period (Fig. 2.6). By applying this empirical relationship to temperature measured at different depths by the thermistor chain, I estimated salinity from temperature. To ensure the empirical relationship at a time step t_i, the calculation bin was set to $t_i \pm 1.5\ days$ (3 days in total). The empirical relationship was accepted only when $r^2 > 0.1$ and $p < 0.01$ (Fig. 2.6). From the salinity vertical distribution that passed the statistical tests above, density was calculated from salinity and temperature. Buoyancy frequency N was calculated as follows: $N = \sqrt{-\frac{g}{\rho_0} \cdot \frac{d\rho}{dz}}$, where g is gravity acceleration, ρ_0 is average density, and $d\rho/dz$ is a vertical gradient of density.

To validate the N estimation, I also calculated N from CTD profiles conducted by Tokyo Metropolitan Government. The profiles were done at seven observational points around Izu-Oshima Island in such a way that distance between each point and the nearest shore line was less than 10 km. A set of the seven CTD profiles was acquired once a month, and each set was completed within two days. An

average N for each set was calculated at the depth range corresponding to the thermistor chain.

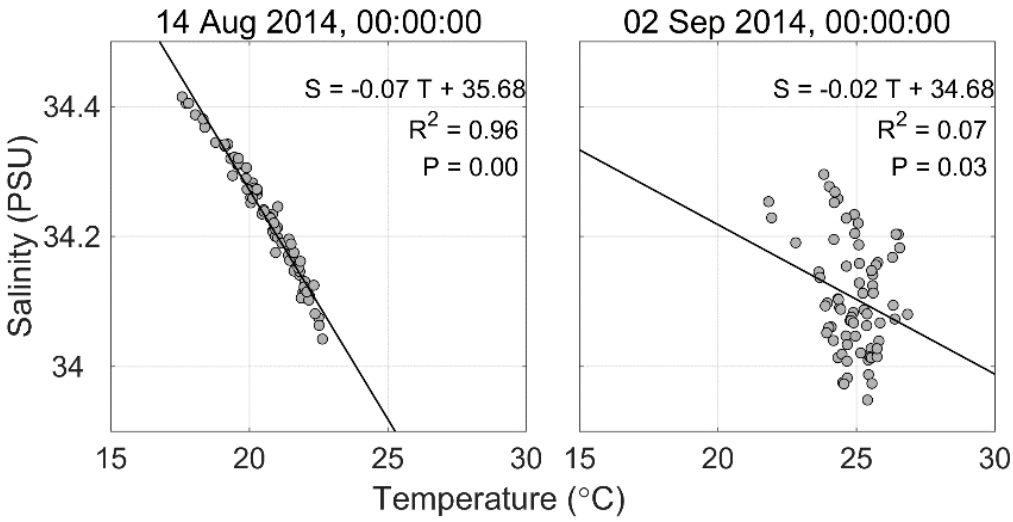

Fig. 2.6. Example of empirical relationship between temperature and salinity. Gray filled circles denote 1-h calculated values. Left panel shows a linear relationship that passes the statistical test of $r^2 > 0.1$ and $p < 0.01$, and right panel shows one that does not pass the test.

Significant wave height

The pressure data was converted to depth from the international equation of state of seawater (Fofonoff & Millard Jr. 1983). Significant wave height $H_{1/3}$ was estimated from $H_{1/3} \cong 4.004\eta_{rms}$, where η_{rms} is the root-mean-square of the surface elevation, assuming the individual wave heights follow the Rayleigh distribution (Goda & Kudaka 2007).

Wave orbital velocity

Wave orbital velocity was estimated based on a linear wave theory. Maximum orbital velocity during a wave phase U_{par} is estimated as follows:

$$U_{\mathrm{par}} = \frac{\pi H}{T}\frac{\cosh(kd)}{\sinh(kh)}, \tag{2.1}$$

where H is the wave height ($\sim H_{1/3}$ in this study), T is the wave period, k is the

radian wavenumber, d is the elevation above the bottom where you want to calculate U_{par}, h is the bottom depth (~20 m). T was defined as an inverse of a peak frequency of power spectrum density of surface elevation that is proportional to the changes in the pressure. A wavenumber k was estimated by solving the dispersion equation $\omega^2 = gk\tanh(kh)$, where ω is radian frequency ($\omega = 2\pi / T$), and g is gravity acceleration. The equation was solved to kh by the Newton-Raphson method (see Soulsby 2006). d was set to 2.22 m that is the same depth as CPICS (Fig. 2.2b). The maximum orbital velocity was also estimated using the Vector data. Orthogonal horizontal velocity components, u and v, include any current phenomena with frequencies less than the Nyquist frequency. Horizontal velocity components, u and v, were decomposed as follow: $u = u' + \bar{u}$ and $v = v' + \bar{v}$, where $\bar{u}$ and $\bar{v}$ are the background components derived by low-pass filtering u and v with a cut-off frequency of 1 / 20 Hz which was significantly low to remove wave components. Hence, the high frequency components, u' and v', include orbital velocity. Maximum orbital velocity during a wave phase U_{obs} was estimated from the following equation (Wiberg & Sherwood 2008):

$$U_{\mathrm{obs}} = \sqrt{2\left(\mathrm{var}(u') + \mathrm{var}(v') - 2\mathrm{var}(U_{\mathrm{noise}})\right)}, \tag{2.2}$$

where $\mathrm{var}(U_{\mathrm{noise}})$ is the noise variance of the instrument (~0.000036 m^2 s^{-2} for the Vector). While u' and v' may contain turbulence, the current due to turbulence is much smaller than the one due to the surface waves and can be negligible in shallow-water regions (Trowbridge 1998). To evaluate currents with frequencies less than 1 / 20 Hz (e.g. tidal flows), background velocity $\bar{U}$ is calculated as $\bar{U} = \sqrt{\bar{u}^2 + \bar{v}^2}$. U_{obs} and $\bar{U}$ were not available from September 16th to October 20th, since the flow pattern at the sampling volume of the Vector was artificially disturbed by a net surrounding the CPICS.

Turbulent kinetic energy dissipation rate

Near-bed turbulent kinetic energy (TKE) dissipation rate (ε, W kg^{-1}) was estimated from friction velocity u_* assuming logarithmic low of the wall (Drost et al. 2018);

$$\varepsilon = \frac{{u_*}^3}{kz}, \tag{2.3}$$

where k is the von Karman constant (= 0.41), and z is the distance from the bottom (= 2.22 m). The bottom friction velocity is expresses as:

$$u_* = \left(\frac{\tau}{\rho}\right)^{1/2}, \tag{2.4}$$

where τ is the bed shear stress, and ρ is the seawater density. Since non-linear interactions between currents and wave orbital velocity modify near-bed stress (Soulsby 1995), τ was estimated from the bed shear stress associated with pure currents τ_c and pure surface waves τ_w, tbased on a method proposed by Drost et al. (2018). τ_c was estimated from the following equation:

$$\tau_c = \rho C_D \bar{U}^2, \tag{2.5}$$

where ρ is the seawater density, C_D is the drag coefficient (= $0.072\mathrm{Re}^{-0.2}$, Hoerner 1965), $\bar{U}$ is the background velocity. For the Reynolds number in the C_D calculation, $\bar{U}$ and the distance from the bottom z (= 2.22 m) were used for the representative velocity and length scales, respectively. Shear stress associated with waves τ_w was estimated from the following equation:

$$\tau_w = \frac{1}{2}\rho f_w u_w^2, \tag{2.6}$$

where f_w is the wave friction factor, and u_w is the maximum orbital velocity (~U_{par}). f_w was estimated following an empirical equation (Swart 1974);

$$f_w = 0.00251 \exp\left[5.21\left(\frac{A}{k_s}\right)^{-0.19}\right] \text{ for } \frac{A}{k_s} > 1.57 \tag{2.7}$$

$$f_w = 0.3 \text{ for } \frac{A}{k_s} \leq 1.57,$$

where k_s is the Nikuradse roughness (= 0.03 m, Drost et al. 2018). Here A is the wave orbital excursion length defines as $A = \frac{u_{w,rms}}{\omega}$, where $u_{w,rms}$ is the rms orbital velocity (Soulsby 2006), and ω is the radian frequency. The bed shear stress τ associated with currents and surface waves was estimated from the following equation;

$$\tau = \tau_c \left[1 + \alpha \left(\frac{\tau_w}{\tau_c + \tau_w}\right)^{\beta}\right], \tag{2.8}$$

where $\alpha = 1.2$ and $\beta = 3.2$ are the empirical coefficients ensured by Soulsby (1995).

Acoustic backscatter

The Aquadopp incidentally records acoustic amplitude Amp (in the unit of "counts"). Amp can be converted to acoustic backscatter by attenuation corrections (Nortek AS, www.nortek-as.com/lib/technical-notes/seditments):

$$\text{acoustic backscatter} = 0.43Amp + 20\log_{10}(R) + 2\alpha_w R, \tag{2.9}$$

where R is the distance between the sampling volume and the transducer along the beam axis, α_w is the absorption coefficients by the water (in dB m^{-1}), and z is the vertical coordinate. α_w was calculated by a simplified absorption formula, taking account of the acoustic frequency of the Aquadop (400 kHz) and environmental data, such as temperature, salinity, and depth (Ainslie and McColm 1998), where salinity was estimated from a linear regression between temperature and salinity measured by the CT sensor (see *Stratification* in this subsection). Even after the Eq. (2.9), acoustic backscatter is biased due to a change in sampling volume. Sampling volume increases with increasing distance from each transducer, depending on the "cone shape" of the acoustic beams (Fig. 2.2b). To correct this bias, acoustic backscatter was normalized (divided) by sampling volume of each bin. Acoustic backscatter ensured above was not calibrated and, hence, is a variable proportional to volume backscattering strength. Data acquired from the 1st layer was not used since the values appeared unrealistic. Also, data acquired from the layers above 10 MAB (from the 9th layer) was not used since these layers are easily contaminated by human's activities (e.g. fishery and construction).

2.3 Results

2.3.1 Physical and biological background

Time series of ROI counts and environmental parameters are shown in Fig. 2.7 during the analysis period. ROIs (counts $hour^{-1}$) have several local peaks, and fluorescence and optical backscatter are highly intermittent. Significant wave height $H_{1/3}$ frequently exceeded 1 m when typhoons approached (Fig. 2.1a).

Buoyancy frequency N estimated at the observation site agreed with the estimated N from the monthly-conducted CTD profiles around Izu-Oshima Island (Fig. 2.7). N^2 was around $N^2 = 10^{-4}$ to 10^{-3} s^{-2} during August and September. While N^2 was below 10^{-4} s^{-2} during the typhoon period (from the end of September to the middle October) (Fig. 2.1a; Fig. 2.7f,m), the stratification was enhanced again ($N^2 \sim 10^{-4}$ s^{-2}) after the typhoon season until around November 5th. The stratification was very weak in the rest of November but was enhanced frequently ($N^2 \sim 10^{-4}$ s^{-2}) in December (Fig. 2.7m).

Temperature spectra had power peaks at diurnal K1 and semi-diurnal M2 frequencies during August and September, as well as the mid-October to the beginning of November (Fig. 2.8a). Internal gravity waves were active at the observation site during these periods (Fig. 2.8b). During the typhoon period and the period after November 5th when the stratification was relatively weak ($N^2 < 10^{-4}$ s^{-2}), internal gravity waves were weak (Fig. 2.8c). Regardless of the condition of the internal gravity waves, background current velocity $\bar{U}$ fluctuated with the temperature fluctuations throughout the analysis period (Fig. 2.8d,e).

During the periods of from August to September and from the middle October to the November 5th, the water mass alternatively changed between warm low-salinity water and cold high-salinity water (Fig. 2.9). On the other hand, when the stratification was temporally enhanced in December, the water mass exchange was between warm high-salinity water and cold low-salinity water (Fig. 2.9). Satellite images by MODIS showed that warm water mass branched off the Kuroshio current axis and reached the observation site in December (Fig. 2.10). The approaches of the warm water masses were synchronized with the re-stratifications of the water column at the observation site in December (Fig. 2.10). While the approaches of the warm water masses modified the water mass characteristics to warmer and more saline even in summer and fall, the dynamic ventilation of the water at the observation site was maintained mainly by internal gravity waves.

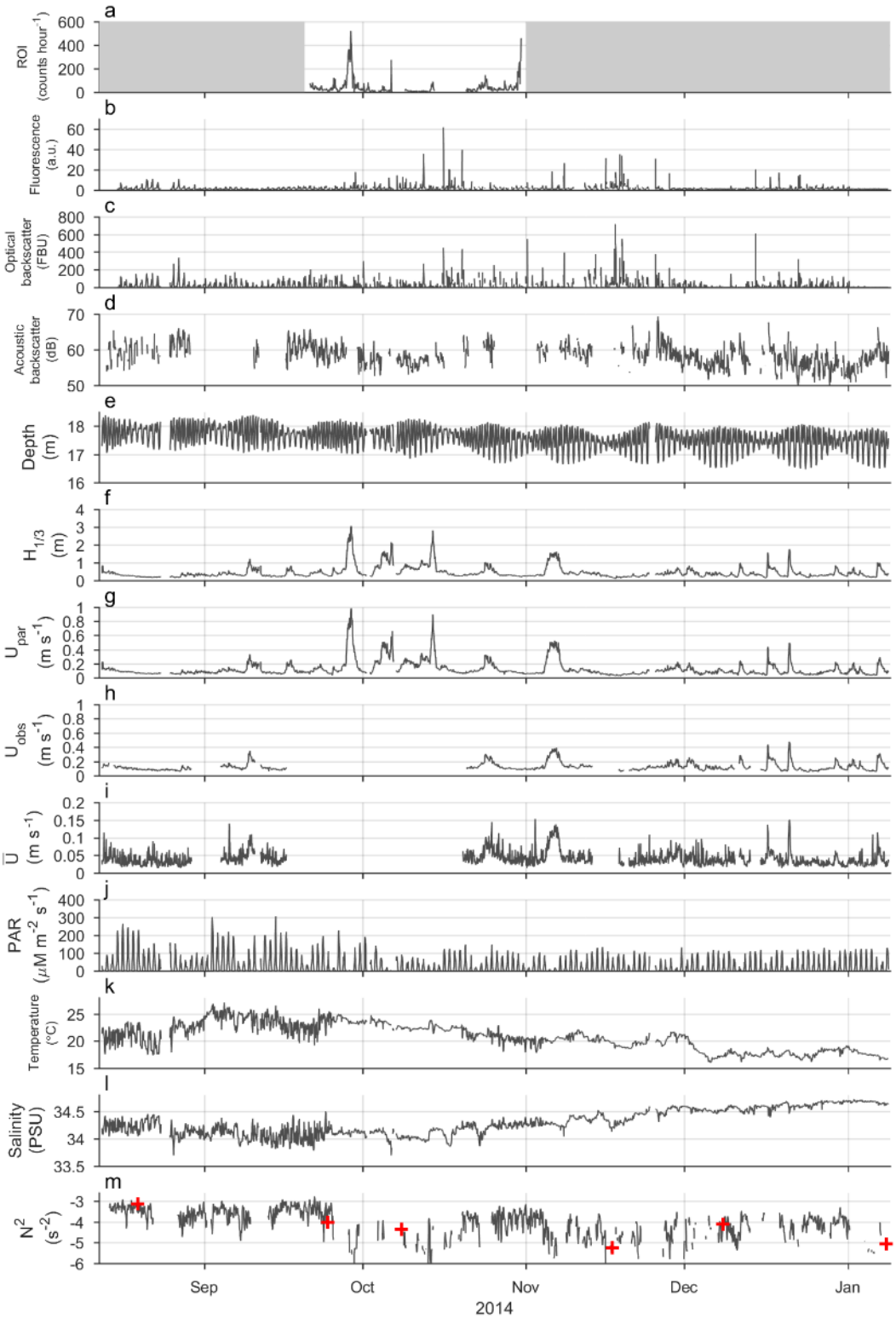

Fig. 2.7. Time series of biological, physical, and chemical parameters over the analysis period. Each parameter is shown as 1-hour averaged value. Gray sections in the top panel denote no-data period. Red crosses in the bottom panel denote data from CTD profiles by Tokyo Metropolitan Government.

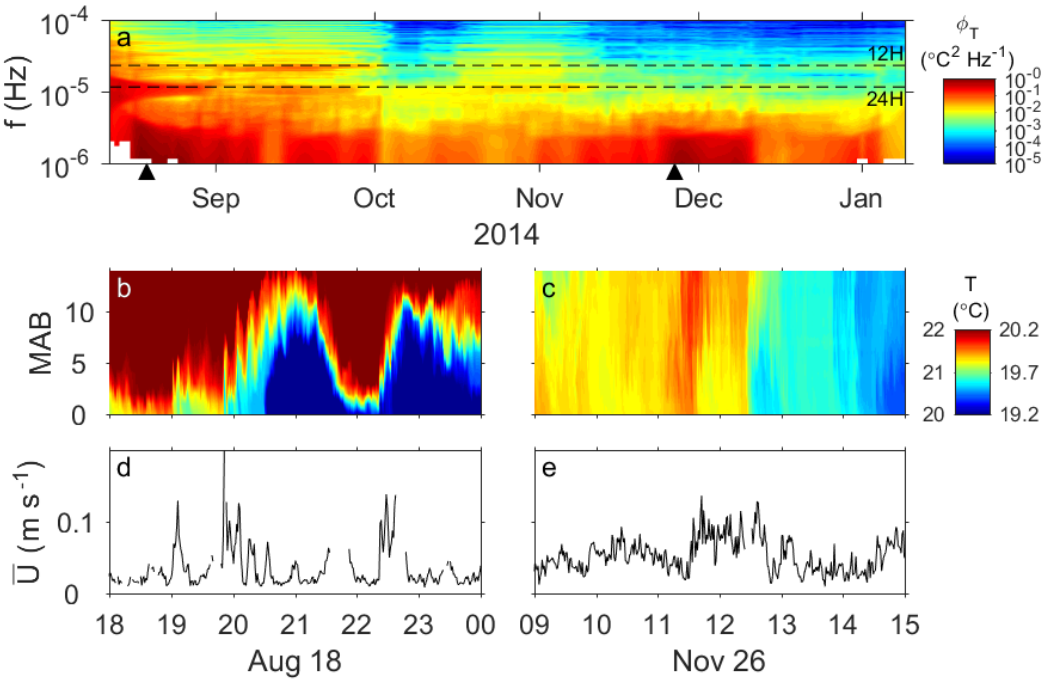

Fig. 2.8. (a) Time series of temperature spectrum through the analysis period. Horizontal dashed lines denote diurnal K1 and semi-diurnal M2 frequencies. (b) Vertical time series of temperature on August 18 (pointed by a black-filled triangle in (a)) with a color range of 20 to 22 °C. Internal gravity waves are remarkable. (c) Same as (b) but for November 26 with a color range of 19.2 to 20.2 °C. Internal gravity waves were not remarkable. (d, e) Background velocity $\bar{U}$ observed on August 18 and November 26.

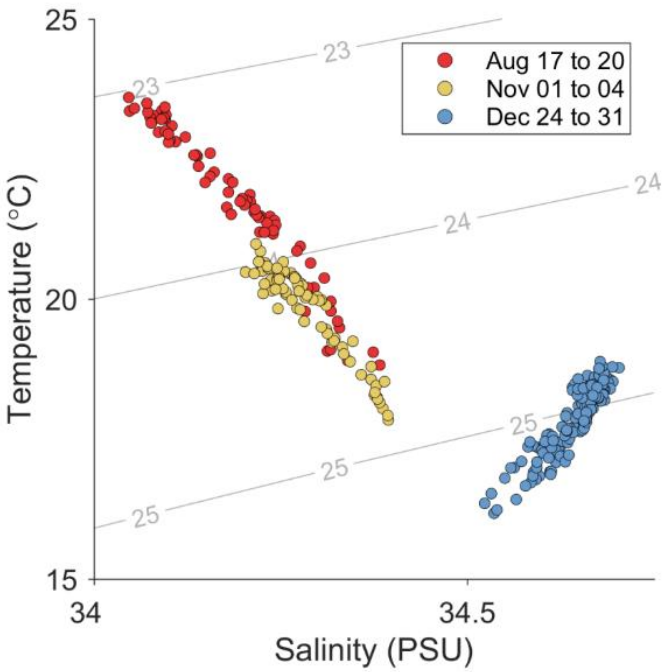

Fig. 2.9. TS diagram obtained from the CT sensor. Data were acquired during several days in August (denoted as red-filled circles), November (yellow-filled circles), and December (blue-filled circles). The stratification was relatively strong $N^2 > 10^{-4}$ s^{-2} during those periods (Fig. 2.7m). Gray lines denote isopycnal lines.

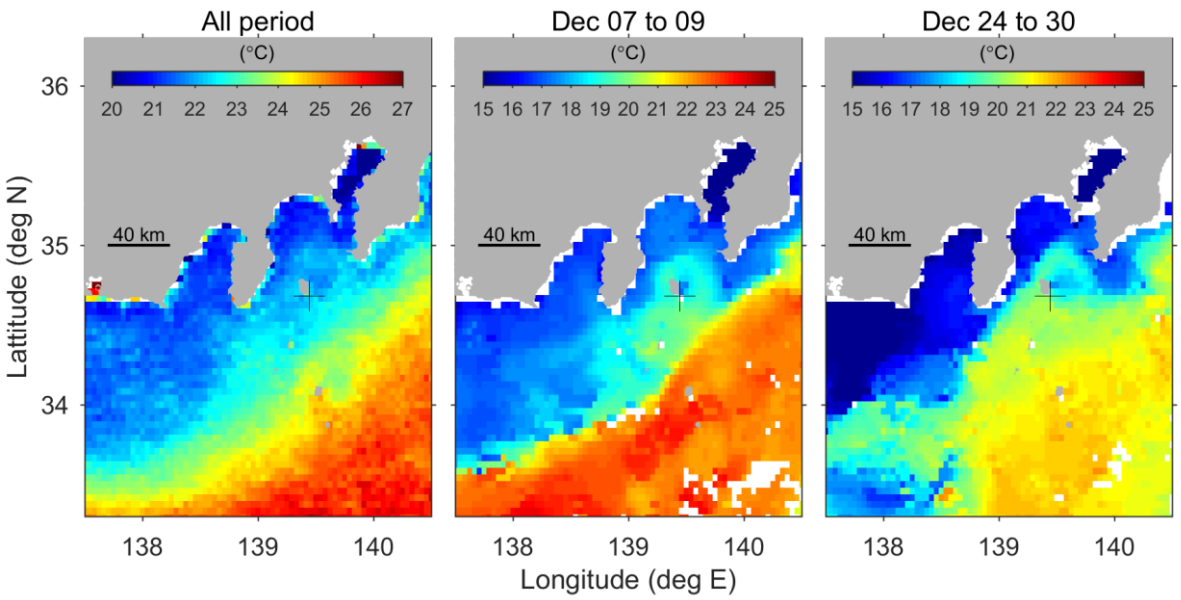

Fig. 2.10. Sea surface temperature (SST) from satellite images by MODIS. (a) SST averaged over the analysis period. The Kuroshio current axis was located about 100 km south from Izu-Oshima Island. (b) SST averaged through December 7th to 9th, and (c) through December 25th to 30th. Warm water masses of 20 to 21 °C branched off the Kuroshio current axis and approached the observation site, and the stratification at the observation site got enhanced ($N^2 \sim 10^{-4}$ s^{-2}) even in December (Fig. 2.7m).

2.3.2 ROI and zooplankton

Over 36000 ROI images were obtained during the manual classification period. The zooplankton images were classified into 17 zooplankton taxa (Fig. 2.11a–q). Zooplankton taxa in total occupied 11.5% of the total ROIs (Table 2.2). Marine snow occupied 58.5% (Fig. 2.11r, Table 2.2), and mineral grain appeared 21.3% (Fig. 2.11s, Table 2.2). Various phytoplankton taxa were also found and classified into a taxon "phytoplankton" in this study (Fig. 2.11t, Table 2.2).

9 zooplankton taxa, such as Ostracoda and Mysida, exclusively appeared during night time (Fig. 2.11a–i, Table 2.3). Hereinafter, these taxa are called "strong migrator". 6 zooplankton taxa, such as Calanoida and Larvacea, appeared during both night and day time, but these taxa were more abundant during night with ratios of 60 to 80% (Fig. 2.11j–o, Table 2.3) (hereinafter "moderate migrator"). 2 zooplankton taxa of Radiolaria and Aulosphaera that have almost no motility appeared during both night and day time evenly (Fig. 2.11p,q, Table 2.3) (hereinafter "non-migrators"). The strong migrator were 67.4%, the moderate migrator appeared 18.4%, and the non-migrators occupied 14.2% in total zooplankton taxa (Table 2.2).

The strong migrator have a peak in their abundance at around October 2nd (Fig. 2.12a), while the non-migrators, marine snow, and phytoplankton have a strong peak at the end of October (Fig. 2.12c,d,f). Both marine snow and mineral grain are strongly correlated with significant wave height $H_{1/3}$ (Fig. 2.12d,e,g).

Table 2.2. Ratio of observed ROIs.

Taxa	% in all taxa
Marine snow	58.5
Mineral garain	21.3
Zooplankton taxa	11.5
Phytoplankton	8.7

Fig. 2.11. Representative ROI for each taxon. (a–q) Zooplankton taxa, (r) marine snow, (s) mineral grain, and (t) phytoplankton. Each zooplankton taxon is named as (a) Ostracoda, (b) Mysida, (c) Polychaeta, (d) Decapoda, (e) Chaetognatha, (f) Monstrilloida, (g) Amphipoda, (h) Isopoda, (i) Cumacea, (j) Calanoida, (k) Larvacea, (l) Harpacticoida, (m) Cyclopoida, (n) Poecilostomatoida, (o) Hydrozoa, (p) Radiolaria, and (q) Aulosphaera. Scale bar indicates 2 mm for the images with an asterisk (*) and 4 mm for the others.

Table 2.3. Correlations of abundance (ind L^{-1}) against currents (U_{par} and $\overline{U}$) and turbulence (ε) for each zooplankton taxon. Single asterisk denotes p<0.05. Double asterisk denotes p<0.01. Letters in brackets next to zooplankton taxa names correspond to those in Fig. 2.8.

	Taxa	% in zooplankton taxa	Night time abundance (%)	r Abundance vs U_{par} (m s^{-1})		r Abundance vs $\overline{U}$ (m s^{-1})		r Abundance vs ε (W kg^{-1})	
				Night	Day	Night	Day	Night	Day
Strong migrators (only night)	Ostracoda (a)	18.2	100.0	–0.48**	—	–0.36**	—	–0.54**	—
	Mysida (b)	15.5	99.8	–0.25**	—	–0.30**	—	–0.36**	—
	Polychaeta (c)	11.9	98.9	–0.30**	—	–0.19	—	–0.32**	—
	Decapoda (d)	7.0	100.0	–0.35**	—	–0.32**	—	–0.41**	—
	Chaetognatha (e)	5.0	100.0	–0.23**	—	–0.06	—	–0.23**	—
	Monstrilloida (f)	4.0	99.1	–0.28**	—	–0.10	—	–0.30**	—
	Amphipoda (g)	3.4	95.6	–0.13*	—	–0.28**	—	–0.23**	—
	Isopoda (h)	1.4	95.7	–0.20**	—	–0.20*	—	–0.24**	—
	Cumacea (i)	1.0	96.3	–0.19**	—	–0.07	—	–0.20**	—
	Total	67.4	99.3	–0.57**	—	–0.45**	—	–0.68**	—
Moderate migrators (night preferred)	Calanoida (j)	9.1	65.1	–0.16**	–0.15**	0.14	0.14	–0.12*	–0.12*
	Larvacea (k)	3.3	79.8	–0.08	–0.15**	0.14	—	–0.02	–0.12*
	Harpacticoida (l)	2.1	75.0	–0.18**	–0.18**	0.00	—	–0.15**	–0.14*
	Cyclopoida (m)	1.6	59.2	–0.19**	–0.14*	—	—	–0.15**	–0.13*
	Poecilostomatoida (n)	1.5	68.3	–0.20**	–0.17**	0.18	–0.25*	–0.16**	–0.20**
	Hydrozoa (o)	0.8	60.6	–0.03	–0.02	—	—	0.03	—
	Total	18.4	68.4	–0.25**	–0.29**	0.18	–0.01	–0.19**	–0.25**
Non-migrators (Day/night even)	Radiolaria (p)	10.5	52.2	–0.08	0.02	0.21*	0.03	0.00	0.05
	Aulosphaera (q)	3.7	46.8	–0.07	–0.14**	–0.01	0.27*	–0.06	–0.12*
	Total	14.2	50.8	–0.10	–0.06	0.18	0.17	–0.01	–0.03

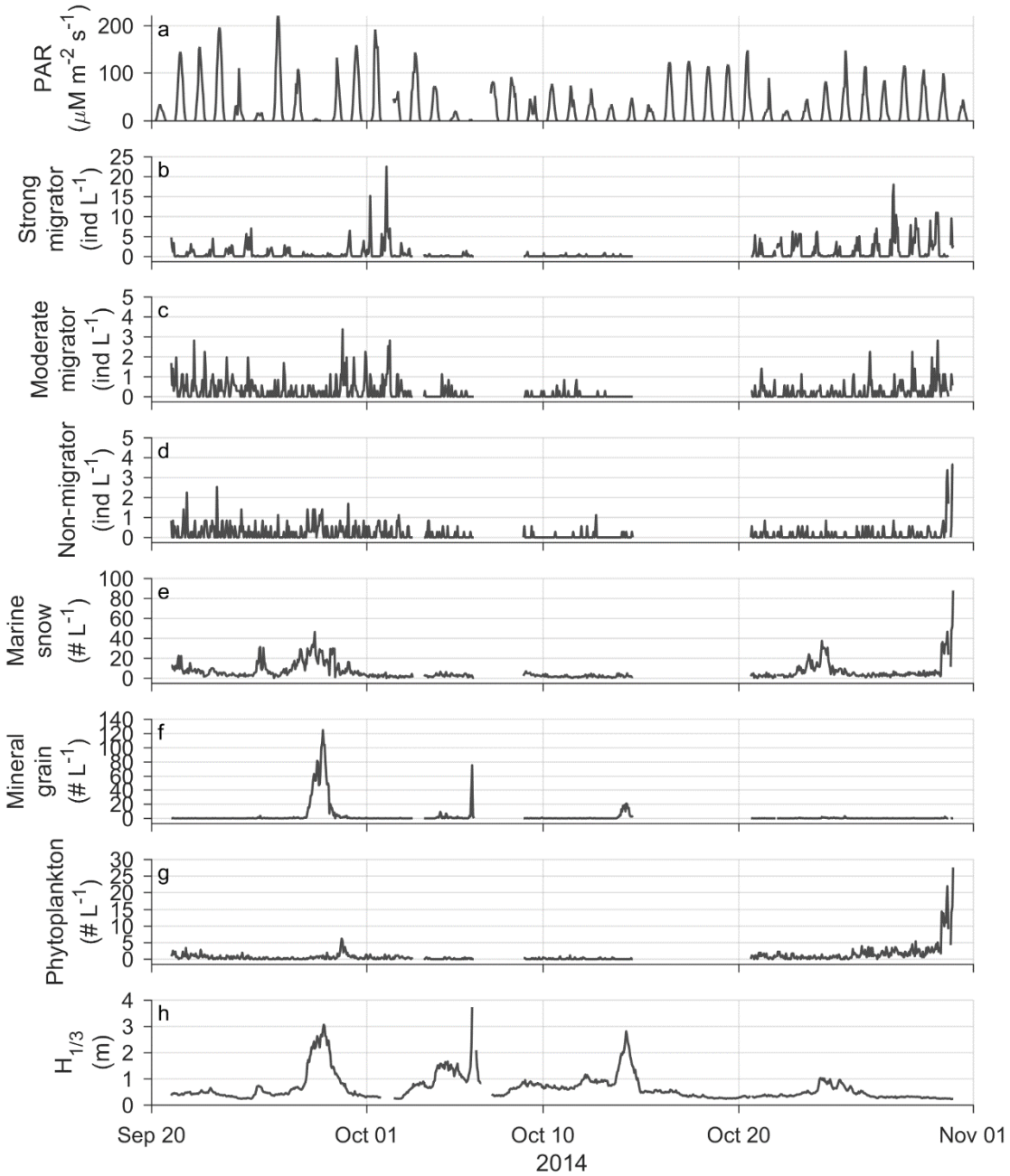

Fig. 2.12. Time series of (a) PAR and abundance of (b) the strong migrator, (c) the moderate migrator, (d) the non-migrator, (e) marine snow, (f) mineral grain, (g) phytoplankton, and (h) significant wave height $H_{1/3}$ over the ROI sorting period. The Y-axes show values calculated in 1-hour bins.

2.3.3 Zooplankton DVM

While zooplankton abundance increased during night time (Table 2.3, Fig. 2.12a,b), acoustic backscatter showed night-time increases regardless of the depth of the samples (Fig. 2.13). Fig. 2.13a and b show an example of time series for PAR and vertical distribution of acoustic backscatter. Night-time acoustic backscatter was 2 dB greater (corresponding to 1.6 times greater in linear scale) than that during day time on average (Fig. 2.13c,d). Acoustic backscatter was averaged over each night and compared with the strong migrator abundance, showing significant correlations regardless of the depth of the samples (r^2 = 0.39 to 0.50, $p < 0.01$) (Fig. 2.13e, Table 2.4).

Similarly to acoustic backscatter, optical backscatter shows night-time increases (Fig. 2.14a,b). Optical backscatter rapidly increased after dusk and decreased before dawn, and night-time values are 10 times greater than day-time values on average (Fig. 2.14c,d). Night-time averaged optical backscatter is significantly correlated with night-time abundance of the strong migrator (r^2 = 0.79, $p < 0.01$) (Fig. 2.13e). Night-time averaged optical backscatter is significantly correlated with acoustic backscatter obtained at the 2nd layer (r^2 = 0.12, $p < 0.01$) that is the closest layer to the bottom and the turbidity sensor. Weak or no correlations were found with those measured at higher Aquadopp layers (Table 2.4). Coefficients of determination among sensors are summarized in Fig. 2.15.

Table 2.4. Coefficients of determination of acoustic backscatter against the strong migrator abundance or optical backscatter, at different sampling layers. The statistics were calculated based on night-time averaged values. Single asterisk denotes p<0.05. Double asterisk denotes p<0.01.

Aquadopp layer number	Sampling depth (MAB)	r^2	
		Strong migrator	Optical backscatter
2	3 to 4	0.39**	0.12**
3	4 to 5	0.43**	0.05
4	5 to 6	0.50**	0.07*
5	6 to 7	0.47**	0.06*
6	7 to 8	0.47**	0.05*
7	8 to 9	0.45**	0.05
8	9 to 10	0.40**	0.04

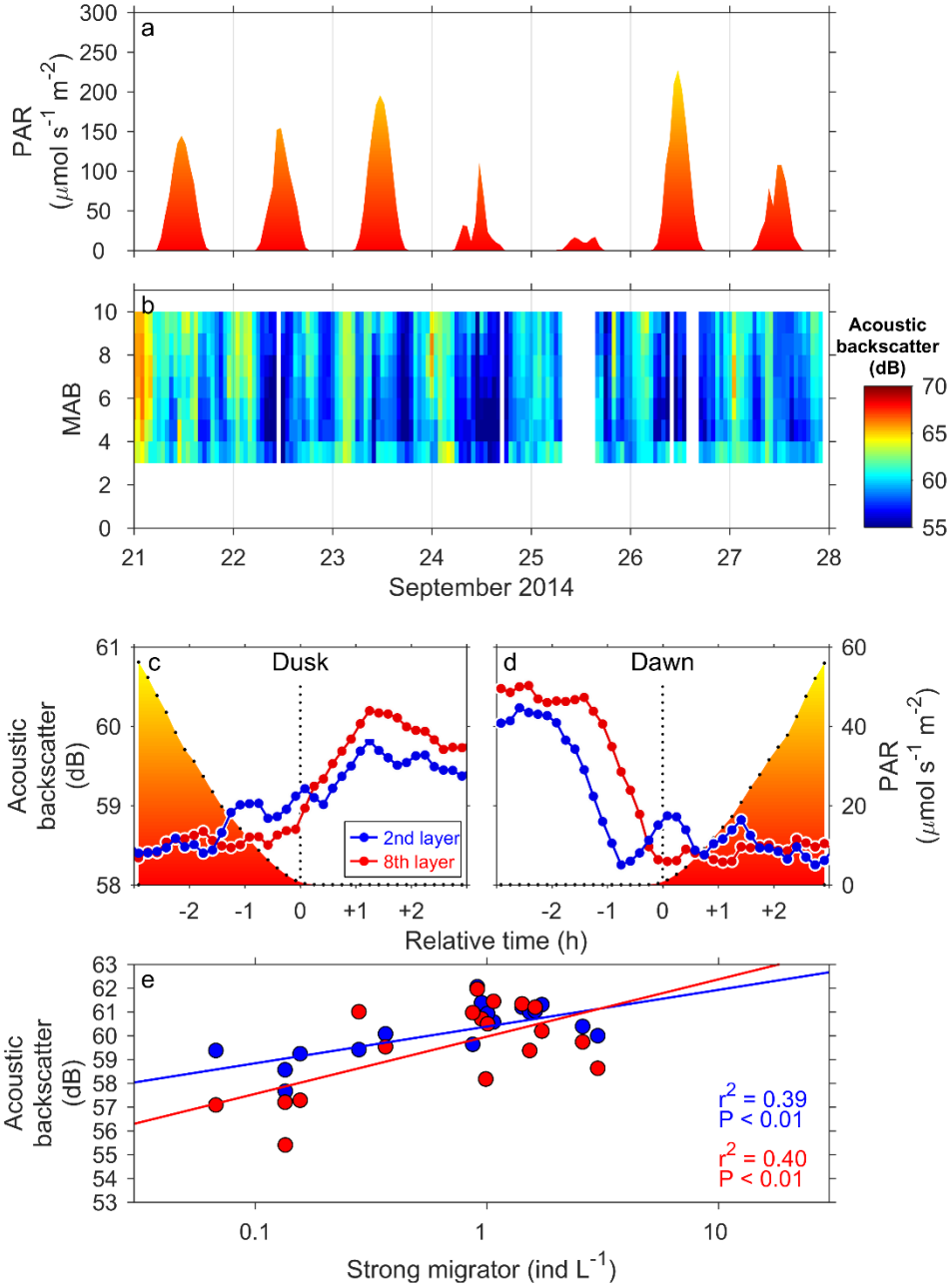

Fig. 2.13. Correlation between acoustic backscatter and the strong migrator. (a,b) An example of time series for PAR and vertical distribution of acoustic backscatter. (c) Acoustic backscatter at the 2nd layer and 8th layer are denoted as blue and red lines respectively. PAR is denoted as filled area. Average was done for the analysis period using 10-min bins set around dusk. (d) Same as (c) but for dawn. (e) Scatter plot between night-time averaged acoustic backscatter and night-time packing density of the strong migrator. Lines indicate regression lines. The statistics were calculated from n = 18 nights.

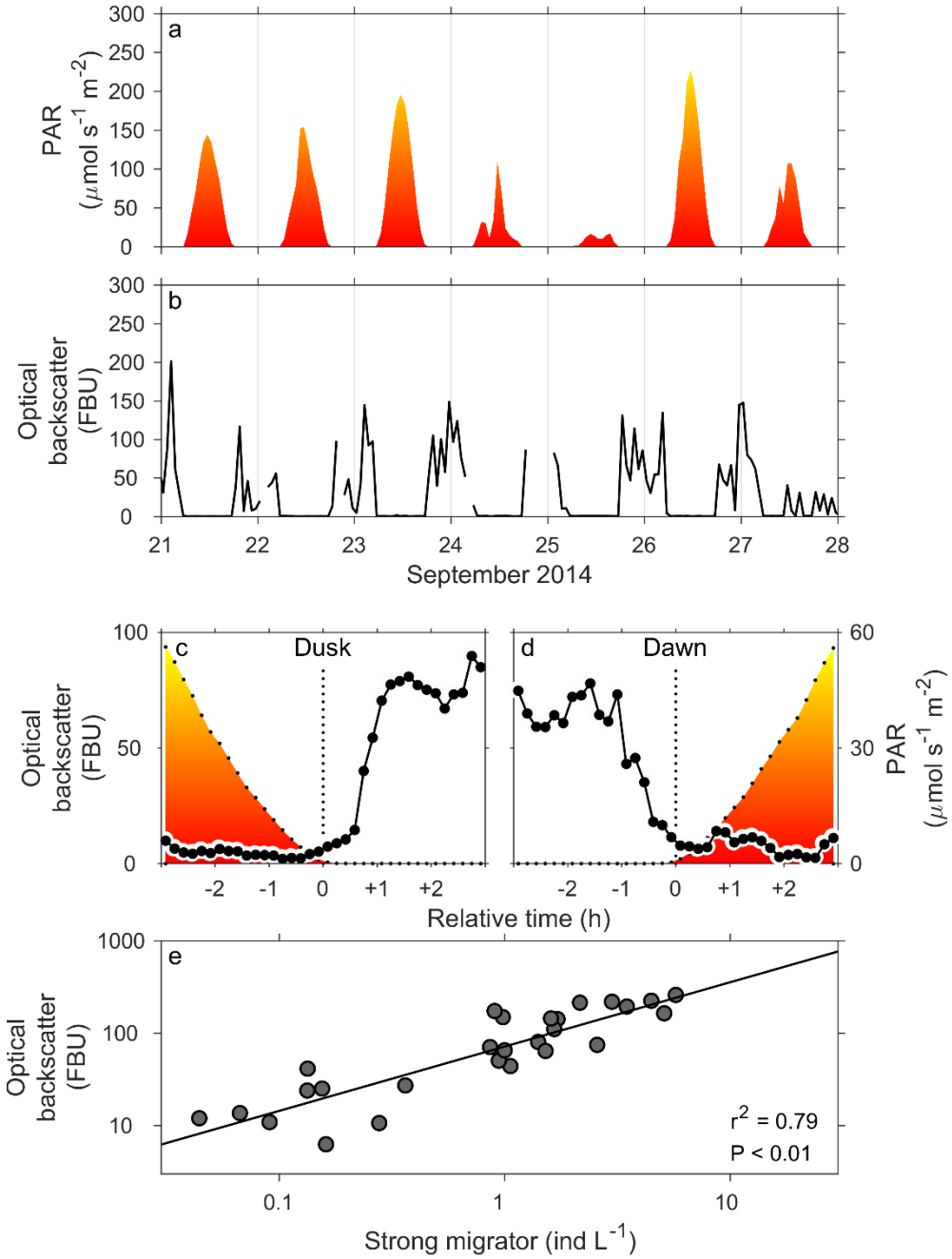

Fig. 2.14. Correlation between optical backscatter and the strong migrator. (a,b) An example of time series for PAR and optical backscatter. (c) Optical backscatter and PAR are denoted as black line and filled area respectively, averaged for the analysis period using 10-min bins set around dusk. (d) Same as (c) but for dawn. (c) Scatter plot between night-time averaged optical backscatter and night-time packing density of the strong migrator. Black line denotes regression line. The statistics were calculated from n = 27 nights.

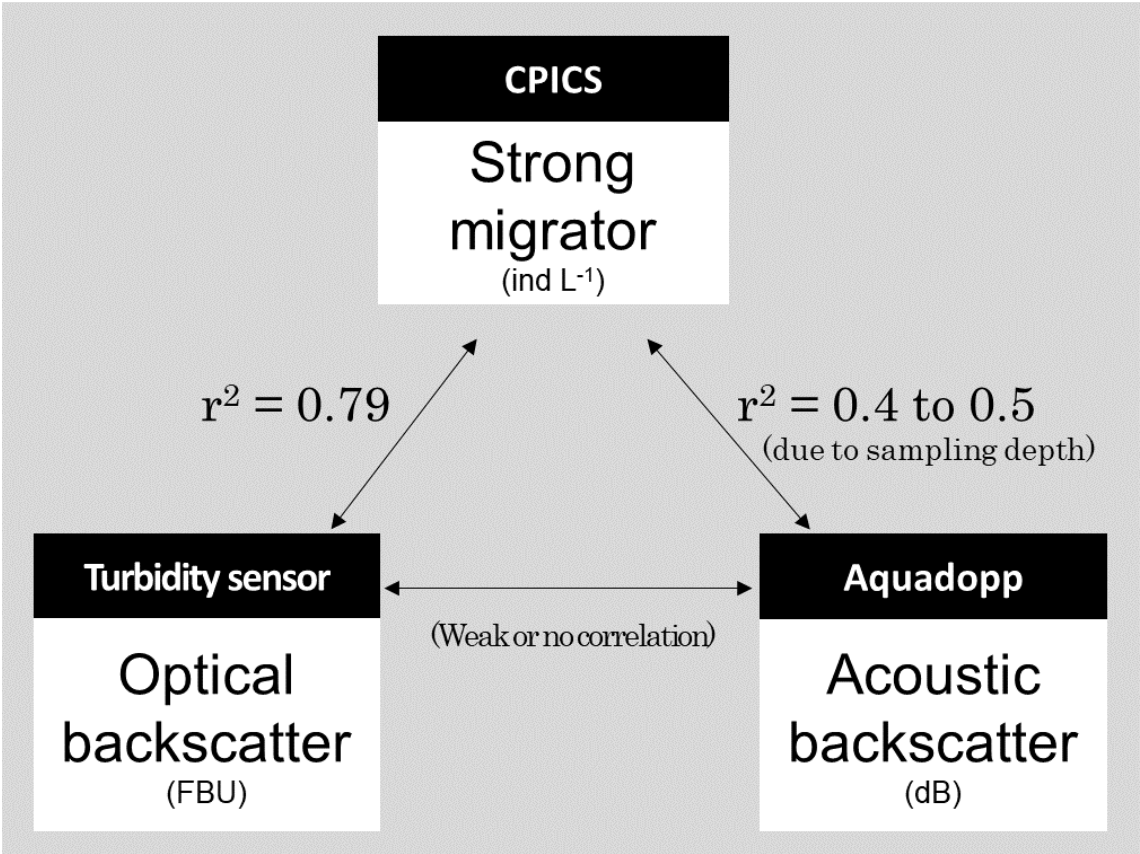

Fig. 2.15. Coefficients of determination among sensors. Statistics are calculated from night-time averaged values, as in Fig. 2.13e, Fig. 2.14e, and Table 2.4.

2.3.4 Currents and zooplankton

Wave orbital velocity U_{obs} (directly observed by the Vector) and U_{par} (estimated from the depth variation) increased frequently, as $H_{1/3}$ increased due to typhoons (Fig. 2.1a) (Fig. 2.7e,f,g,h). U_{obs} and U_{par} are highly correlated ($r^2 = 0.87$, Fig. 2.16a). Since U_{par} is available for longer period than U_{obs} (see Fig. 2.7g,h), U_{par} is used as representative of orbital velocity for further data analyses.

Background velocity $\bar{U}$ is found to increase with U_{par} increased (see early November and middle December in Fig. 2.7g,i). Scatter plot of $\bar{U}$ against U_{par} show that the increase in U_{par} tends to associate with increase in $\bar{U}$ (Fig. 2.16b). To separate $\bar{U}$ from U_{par}, $\bar{U}$ with U_{par}<0.15 m s^{-1} is used for further analyses with biological signals (i.e. zooplankton) (Fig. 2.16b).

Correlation coefficients of abundance of each zooplankton taxa (individuals L^{-1}) were calculated against U_{par} or $\bar{U}$ (Table 2.3). All taxa for the strong migrator show significantly negative correlations with U_{par} ($r = -0.48$ to -0.13, $p<0.05$) (Table 2.3), while the negative correlations are not simple linear relationships (Fig. 2.17). For example, Ostracoda (Fig. 2.8a) show a wide range in their abundance (0 to 10 ind L^{-1}) (Fig. 2.17a). Average abundance is 1.0 ind L^{-1} when U_{par} = 0.1 m s^{-1}, while the average value decreased to 0.1 ind L^{-1} when U_{par} increased to 0.2 m s^{-1} (Fig. 2.17a). No Ostracoda individuals appeared when U_{par} was greater than 0.3 m s^{-1}. Similar decrements along with U_{par} were found in the other zooplankton taxa in the strong migrator (left column in Fig. 2.17). However, degree of decrement seems to be different among zooplankton taxa: for example, the reduction in Mysida abundance is more moderate than that in Ostracoda (Fig. 2.17a,c).

While only a limited period is available for analyses with $\bar{U}$ (see Fig. 2.7a,h), the strong migrator also show negative correlations with $\bar{U}$, and correlations for 5 taxa are statistically significant (Table 2.3). The 5 taxa (Ostracoda, Mysida, Decapoda, Amphipoda, and Isopoda) show decrements along with increased $\bar{U}$ in their averaged abundance (right column in Fig. 2.17). Some taxa show different reactions to U_{par} and $\bar{U}$: for example, Chaetognatha clearly decreased with increasing U_{par} but show almost no correlation with $\bar{U}$ (Fig. 2.17i,j).

For the moderate migrator, all taxa show negative correlations with U_{par} regardless of night or day, and most correlations are statistically significant ($r = -0.20$ to -0.14, $p<0.05$) (Table 2.3). The moderate migrator also show decrements in their abundance with increasing U_{par}, and the patterns are almost the same with night time and day time (Fig. 2.18). The moderate migrator do not show significant correlations with $\bar{U}$ unlike the strong migrator (Table 2.3). Non-migrators show no

significant correlations with either U_{par} nor $\overline{U}$ (Table 2.3).

The average abundance of the strong migrator decreases to one-thirtieth (1 / 30) when U_{par}>0.3 m s^{-1} relatively to those at U_{par}<0.1 m s^{-1} (Fig. 2.19a). For $\overline{U}$, the decrement reached about one-fourth (Fig. 2.19b). The average abundance of the moderate migrator decreases to one-third when U_{par}>0.2 m s^{-1} relatively to those at U_{par}<0.1 m s^{-1}. The ratio of one-third is common in both night time and day time (Fig. 2.19c,d) even if the moderate migrator appeared more frequently at night (Table 2.3).

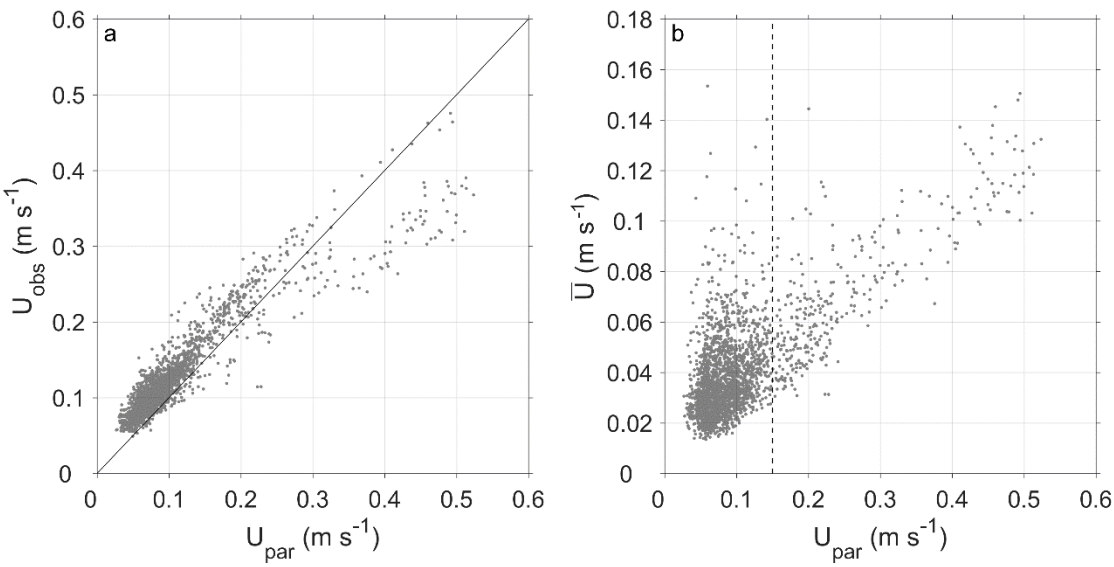

Fig. 2.16. (a) Scatter plot of estimated wave orbital velocity U_{par} against that observed by the Vector U_{obs}. The black line denotes the one-to-one relationship. (b) Scatter plot of the U_{par} versus background velocity $\overline{U}$. The vertical dotted line indicates U_{par} = 0.15 m s^{-1} below which the $\overline{U}$ is available for further analyses with biological signals shown in Figs. 2.17,19,20 and Table 2.5.

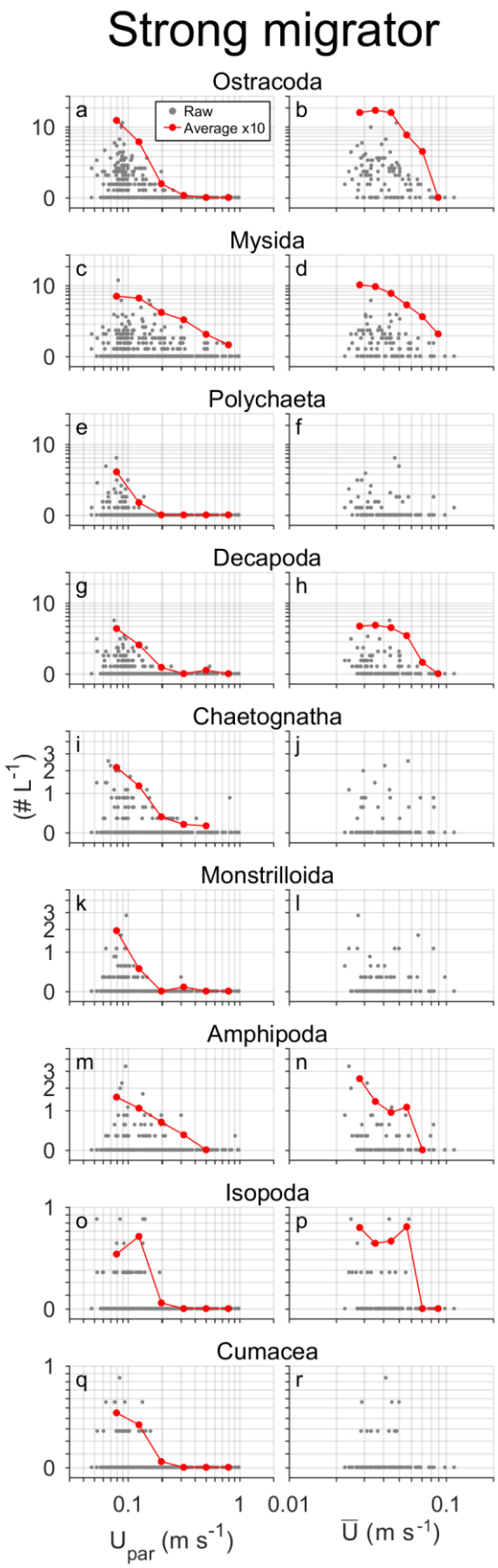

Fig. 2.17. Scatter plots of the strong migrator abundance (ind L^{-1}) versus U_{par} or U_{obs}. Each row is plots of (a,b) Ostracoda, (c,d) Mysida, …, (q,r) Cumacea. Gray dots denote one-hour calculated values. Red-filled circles denote velocity-averaged abundances that are multiplied by 10 for clear visualization. The averages are displayed only for data with $p<0.05$ (Table 2.3).

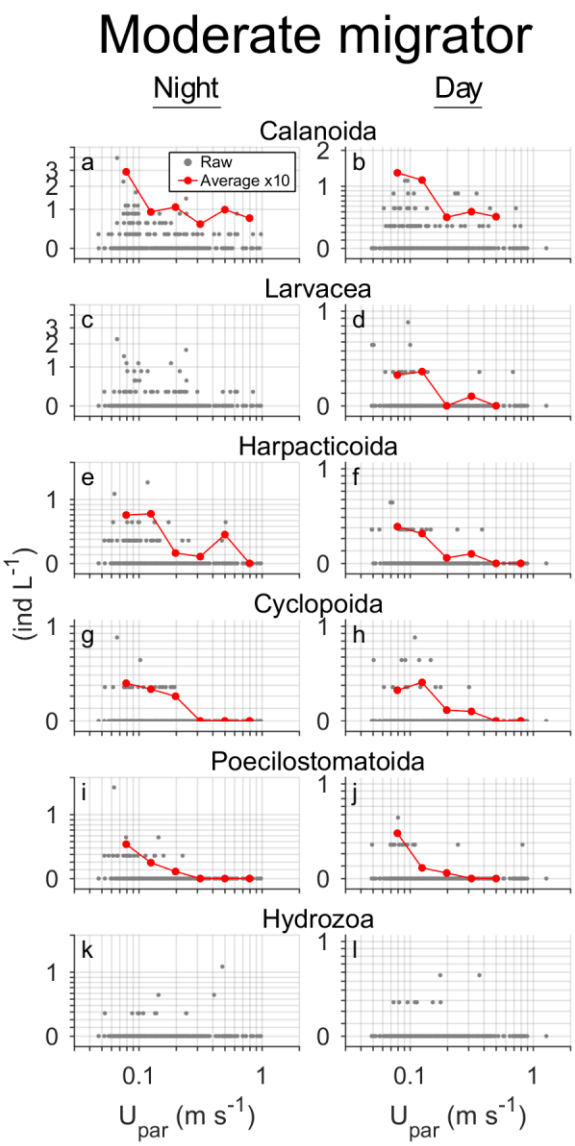

Fig. 2.18. Scatter plots of the moderate migrator abundance (ind L^{-1}) versus U_{par} . Each row is plots of (a,b) Calanoida, (c,d) Larvacea, …, (k,l) Hydrozoa. Left column panels are for data obtained at night, and right column panels are for data at day. Gray dots denote one-hour calculated values. Red-filled circles denote velocity-averaged abundances that are multiplied by 10 for clear visualization. The averages are displayed only for data with $p<0.05$ (Table 2.3). The moderate migrator do not show statistically significant negative correlations against $\overline{U}$ (Table 2.3).

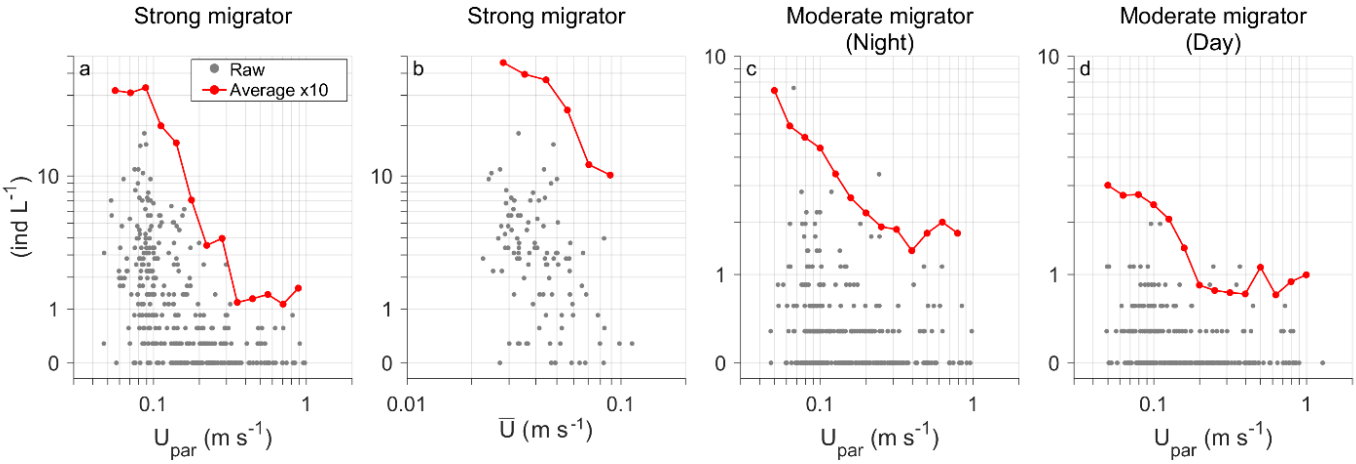

Fig. 2.19. Zooplankton abundance (ind L^{-1}) versus U_{par} or $\bar{U}$. Each scatter plot is for (a) total abundance of the strong migrator versus U_{par}, (b) total abundance of the strong migrator versus $\bar{U}$, (c) total abundance of the moderate migrator and U_{par} at night, (d) total abundance of the moderate migrator and U_{par} at day. (a) and (b) are only from night time since most strong migrator individuals appeared only at night (Table 2.3). All combinations show negative correlations with $p<0.01$ (Table 2.3).

The same analyses with U_{par} and $\bar{U}$ have been done for acoustic backscatter and optical backscatter. Before the analyses, acoustic and optical backscatters were separated into night-time data (dusk + 1h to dawn – 1h) and day-time data (dawn + 1h to dusk – 1h) as these backscatters showed the daily change (Fig. 2.12, Fig. 2.13). Also, the data were separated seasonally into "summer–fall" (period before December 1st) and "winter" (period after December 1st), as optical and acoustic backscatters decreased with decreasing seawater temperature at around December 1st (Fig. 2.7c,d,k). Correlation coefficients of acoustic and optical backscatters against U_{par} and $\bar{U}$ were calculated with changing time (night/day) and season (summer-fall/winter) (Table 2.5).

When the temporal conditions were "night" and "summer–fall", both acoustic and optical backscatters showed negative correlations with both U_{par} and $\bar{U}$ ($r = -0.52$ to -0.19, $p<0.01$) (Table 2.5). Acoustic backscatter showed 5 dB decrease (one-third decrease in linear scale) with increasing U_{par} (Fig. 2.19a) and 3 dB decrease (one-second decrease) with increasing $\bar{U}$ (Fig. 2.19b). Night-time optical backscatter showed one-order decreases with increasing U_{par} or $\bar{U}$ (Fig. 2.19c,d).

Table 2.5. Correlation coefficients of biological parameters (acoustic and optical backscatter) against currents (U_{par} and $\bar{U}$) and turbulence (ε), with changing season (summer–fall or winter) and time (night or day). Single asterisk denotes p<0.05, and double asterisk denotes p<0.01. Under conditions of "summer-fall and night", biological parameters constantly showed significant negative correlations against physical parameters.

		Summer–fall			Winter		
		U_{par} (m s^{-1})	$\bar{U}$ (m s^{-1})	ε (W kg^{-1})	U_{par} (m s^{-1})	$\bar{U}$ (m s^{-1})	ε (W kg^{-1})
Night	Acoustic backscatter	–0.37**	–0.19**	–0.38**	0.28**	0.34**	0.46**
	Optical backscatter	–0.52**	–0.40**	–0.54**	–0.19**	–0.10	–0.17**
Day	Acoustic backscatter	–0.13**	0.01	–0.14	0.21**	0.19**	0.38**
	Optical backscatter	–0.01	–0.21**	–0.06	–0.01	0.13*	0.16

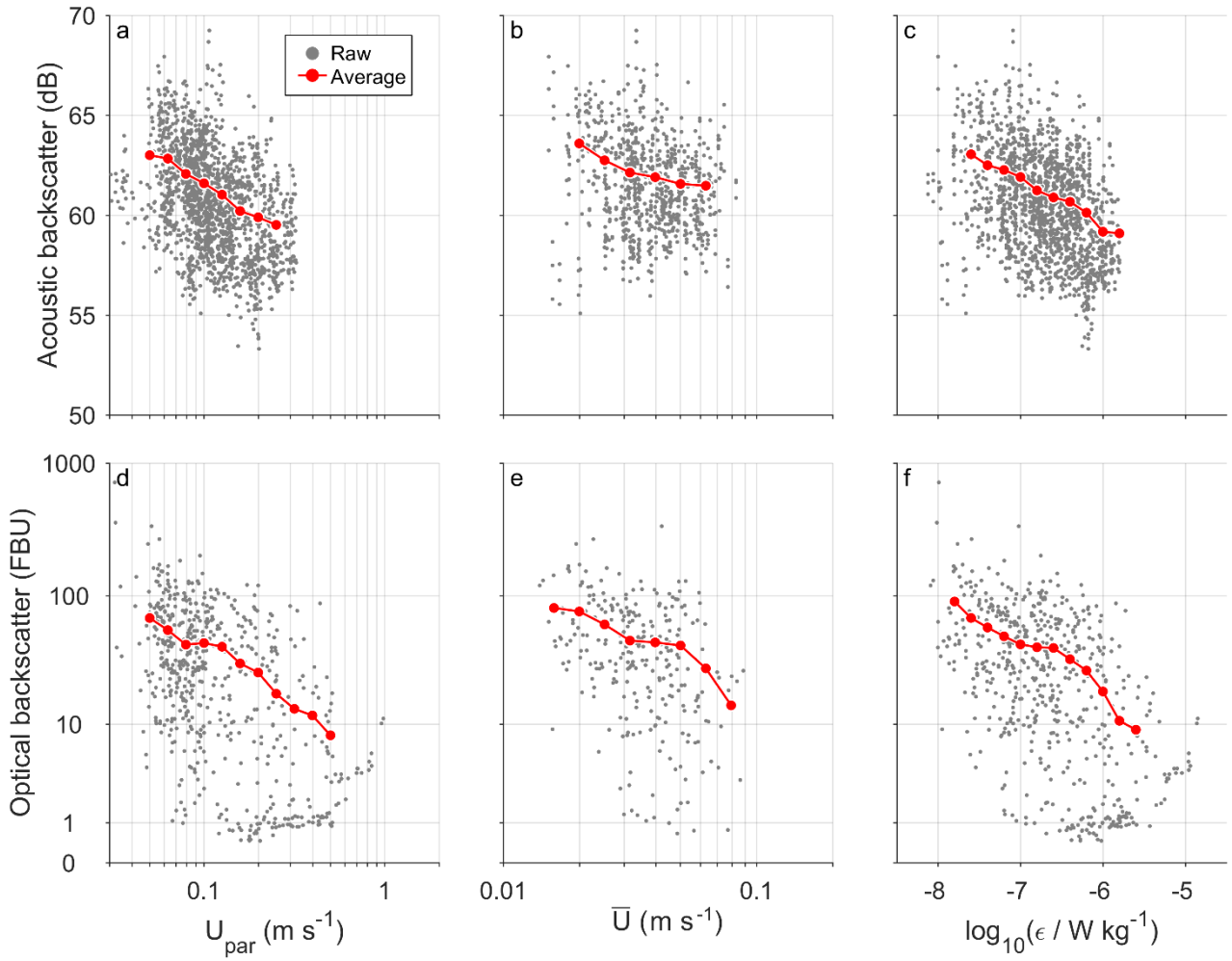

Fig. 2.20. Scatter plots of the biological parameters (acoustic and optical backscatter) against currents (U_{par} and $\overline{U}$) and turbulence (ε). Conditions were set to be "summer-fall and night" where all combinations showed the significant negative correlations (see Table 2.5). Gray dots denote raw values, and red filled circles denote velocity-averaged values.

2.3.5 Turbulence and zooplankton

All taxa of the strong migrator show significant negative correlations against TKE dissipation rate ε (r = –0.54 to –0.20, p<0.05) (Table 2.3). Correlation of the entire strong migrator against ε was r = –0.68 (p<0.01) that was a stronger correlation than those against U_{par} and $\bar{U}$ (Table 2.3). Abundance of the strong migrator decreased sharply as ε increased from 10^{-7} to 10^{-6} W kg^{-1} and became almost zero on average when ε > 10^{-6} W kg^{-1} (Fig. 2.21a).

Abundance of the moderate migrator significantly reduced with increasing ε, where the abundance at ε = 10^{-7} to 10^{-6} W kg^{-1} reduced by one-third compared with that at ε > 10^{-6} W kg^{-1} (Fig. 2.21b,c). The rate of reduction was same at both nighttime and daytime (Fig. 2.21b,c). The average abundance at ε > 10^{-6} W kg^{-1} remains about 0.1 ind L^{-1} that is larger than that of the strong migrator (Fig. 2.21b,c). While almost all taxa of the moderate migrator show significant negative correlations with ε (r = –0.20 to –0.12, p<0.05) (Table 2.3), the correlation of the entire moderate migrator (r = –0.19 at night and r = –0.25 at day) was much weaker than that of the entire strong migrator (r = –0.68). Acoustic and optical backscatter showed significant negative correlations against ε as well (Fig. 2.20c,f, Table 2.5).

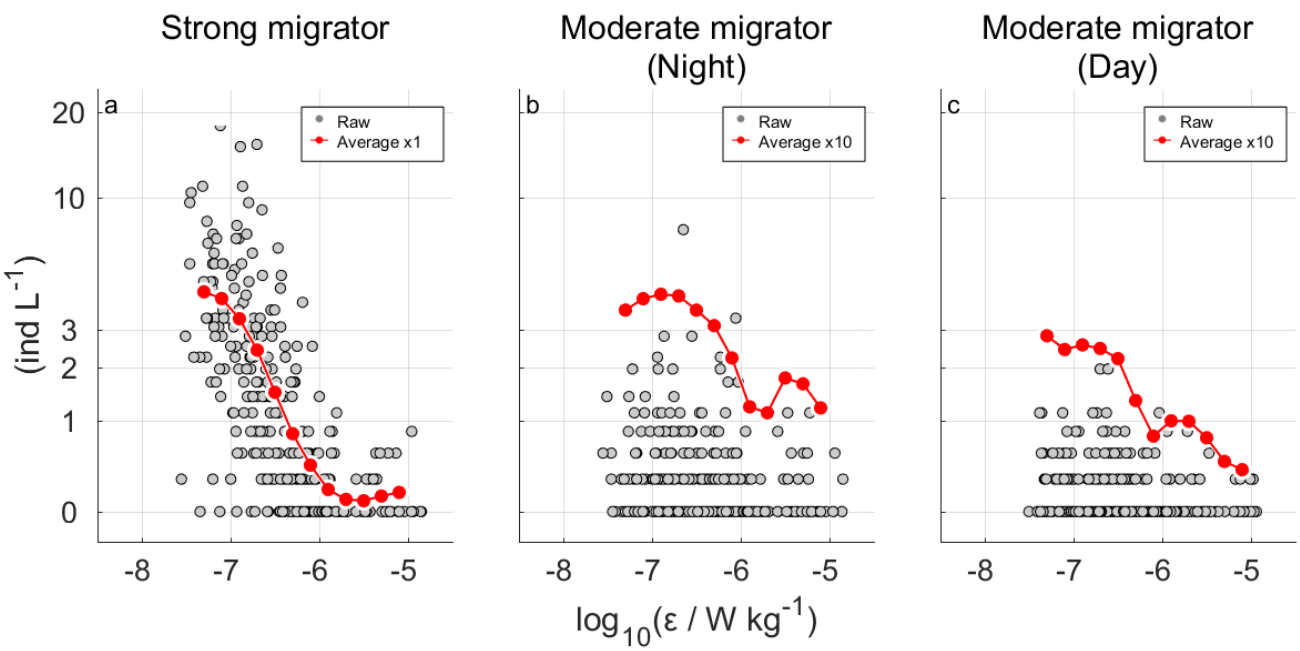

Fig. 2.21. Zooplankton abundance (ind L^{-1}) versus ε. (a) is only from night time since most strong migrator individuals appeared only at night (Table 2.3). All combinations show negative correlations with p<0.01 (Table 2.3).

2.4 Discussion

2.4.1 Physical background

While many zooplankton taxa were found at the observation site, the water column where those are living was always exposed to various physical processes (Fig. 2.22). Several typhoons passed near the observation site during the analysis period (Fig. 2.1a). The typhoons elevated significant wave heights $H_{1/3}$ (Fig. 2.7f). The increase in $H_{1/3}$ was accompanied by the increases in the estimated orbital velocity U_{par} and the observed orbital velocity U_{obs}.

The increase in $H_{1/3}$ was also accompanied by the increase in background velocity $\overline{U}$ (Fig. 2.15b). Over 90 % of high wave heights ($H_{1/3} > 0.5\ \mathrm{m\ s^{-1}}$) were classified as "Stokes wave" (a non-linear surface gravity wave; van der Bremer & Breivik 2017). For a Stokes wave, the orbit of the water movement is not closed, and an initial point of an orbit drifts forward in the next orbit (see the cartoon in Fig. 2.24). This drift is called Stokes drift and significant from the surface to a depth of λ / 2, where λ is wavelength (van der Bremer & Breivik 2017), while the wavelength was estimated as 50 to 200 m from the dispersion equation (Soulsby 2006, Wiberg & Sherwood 2008). The velocity of Stokes drift averaged over the orbits (hereinafter Stokes velocity, U_{SD}) at a depth of z is defined as $U_{SD} = a^2 \omega k \frac{\cosh(2k(h+z))}{2\sinh^2(kh)}$, where a is wave amplitude (~$0.5H_{1/3}$), ω is angular frequency, k is angular wavenumber, h is the bottom depth (van der Bremer & Breivik 2017). The U_{SD} calculated from observed parameters ($H_{1/3}$ and k) was upper bounded by 1 cm s-1 throughout the analysis period which is obviously smaller than observed $\overline{U}$ associated with high $H_{1/3}$ (Fig. 2.7f,i). Also, the induced current was always southeastward that flows from the shore to the ocean (Fig. 2.23); clearly opposite to the predictable direction of surface wave propagation. Hodograph by the ADV shows that the rotation direction of the orbits was consistent with typical orbit for Stokes wave that propagate from the ocean to the shore (Fig. 2.24). However, the velocity averaged over the cycles (corresponding to $\overline{U}$) was opposite to the wave direction (Fig. 2.24). This is probably due to complicated topography around the observation site (Fig. 2.1c). Since there is a semi-enclosed small bay nearby the observation site, a possible source could be counter-flows which balance total water mass.

Internal gravity waves were active when the stratification was strong. Especially in August and September, the fluctuations of temperature signals were high during diurnal K1 and semi-diurnal M2 frequencies. The complex topography around Izu-Oshima Island is the source of internal gravity waves (Masunaga et al.

2017). While M2 fluctuation is typically stronger than K1 fluctuation in mid-latitudes, internal gravity waves with K1 frequency cannot propagate freely, thus the wave is trapped around the Izu-Oshima island as a Kelvin wave (Masunaga et al. 2017). Also the trapped wave resonates since the travel time around the island matches the forcing period (Masunaga et al. 2017). The K1 internal tides enhanced by the resonations would generate the observed intrusions of the cold-water bores (Fig. 2.8b) and subsequent currents (Fig. 2.8d) under strong stratification in summer.

The meso-scale eddies and streamers typically enhance stratification of the water column even in winter (Mahadevan et al. 2012). Because of the approaches of the Kuoshio-originated water masses in the winter (Fig. 2.9; Fig. 2.10b,c), the local stratification was elevated from $N^2 = 10^{-5}\,\mathrm{s}^{-2}$ to $N^2 = 10^{-4}\,\mathrm{s}^{-2}$ (Fig. 2.7m), that induced baroclinic flow (included in $\overline{U}$) even in winter (Fig. 2.7i; Fig. 2.8c,e).

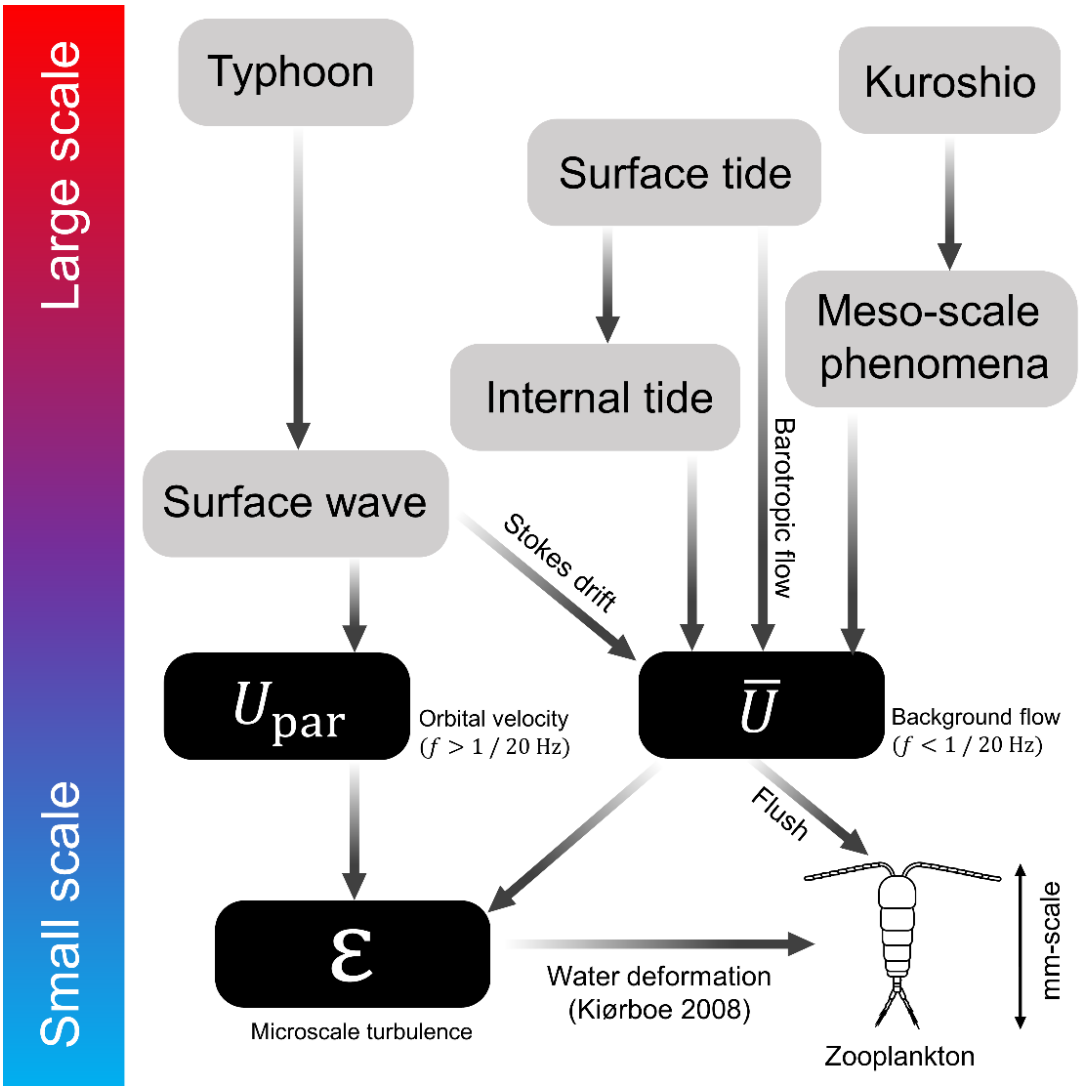

Fig. 2.22. Summary of physical processes and influence on zooplankton. Arrows denote direction of influence. Phenomena at upper (lower) part occur at relatively large (small) scale. Typhoon induce surface waves and consequently enhance wave orbital velocity U_{par} in the water column. Background velocity $\bar{U}$ was associated with significant wave height. Surface tide induce barotropic flows, as well as internal tides that generate baroclinic flows. Meso-scale eddies and streamers that are branched off from Kuroshio also modify local stratification and consequently affect local flow fields at the observation site. Mean flow flush zooplankton away from their original habits. Bottom friction by U_{par} and $\bar{U}$ induced strong turbulence by which zooplankton feel water deformation, rotation, acceleration at a scale of their body size. Zooplankton (e.g. copepods) show avoidance responses to only water deformation (Kiørboe 2008).

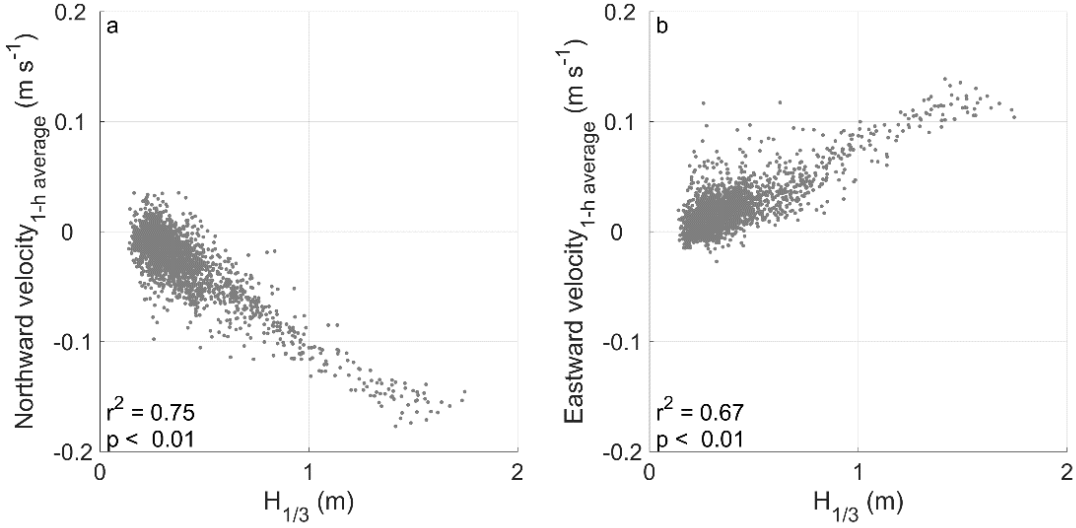

Fig. 2.23. Scatter plot of (a) 1-h averaged northward velocity and (b) eastward velocity against significant wave height.

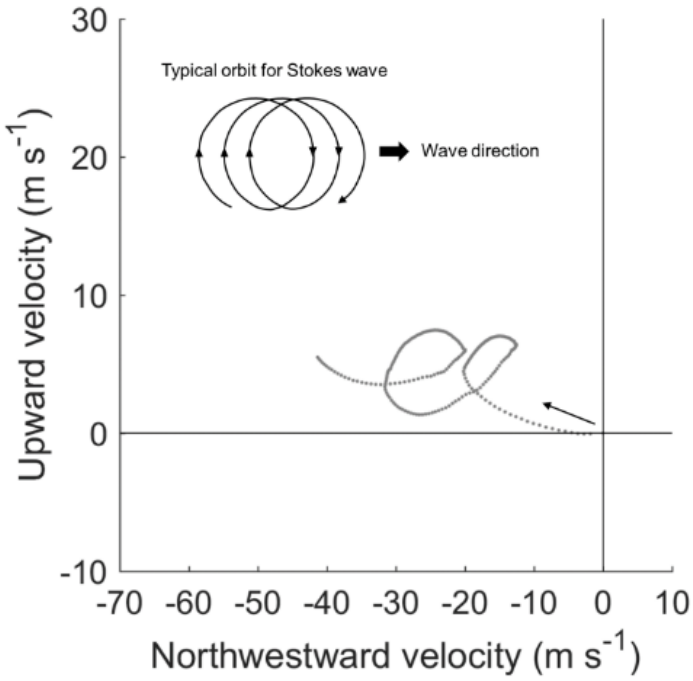

Fig. 2.24. Hodograph for an example data by ADV (sampled at 8 Hz). While the observed orbit is consistent with the typical orbit in terms of rotation direction, current direction averaged over cycles are opposite. The example is 30 seconds (~2 cycles) and acquired at midnight of November 6th when $H_{1/3}$>1 m (Fig. 2.7m).

2.4.2 ROI

While phytoplankton biomass is typically larger than zooplankton biomass (Yurista et al. 2014, Sprules & Stockwell 1995), the observed phytoplankton ROIs were fewer than zooplankton ROIs (Table 2.2). While the most dominant phytoplankton size class in the open water is pico-size (<2 μm), the minimum detection size for ROIs was set to be 100 μm in equivalent sphere diameter. Hence, the observed phytoplankton ROIs were mostly chained/aggregated colonies.

The normalized biomass size spectra (NBS spectra; Yurista et al. 2014, Sprules & Stockwell 1995) were calculated for the phytoplankton and the zooplankton to evaluate the biomass structure in the observation site. The NBS spectra for the trophic levels (i.e. phytoplankton, zooplankton) are typically approximated by dome-shaped regressions (Yurista et al. 2014, Sprules & Stockwell 1995). The NBS spectra from this study were also fitted with the regressions (Fig. 2.25). The regression is expressed as $\log_{10}(\mathrm{Y}) = \mathrm{A} + 0.5 \times \mathrm{C}(\log_{10}(\mathrm{X}) - \mathrm{B})^2$, where Y is normalized biomass per unit volume (in the unit of $\mathrm{g\,L^{-1}\,\Delta g^{-1}}$, where $\Delta\mathrm{g}$ is width of size class), A and B are the vertex coordinates of the dome, C is the curvature of the dome, and X is the size class (in g). Volume of individual (or colony/aggregation) was estimated from the equivalent sphere diameter of the ROI, and the volume was then converted to the mass (in g) assuming that the density of the organism body was same as the seawater density. The coefficients for the regression (i.e. A, B, and C) for zooplankton are comparable with those reported previously (Table 2.6). Since the previous study (Yurista et al. 2014) obtained the coefficients A and B based on phytoplankton single cells unlike this study, the coefficients obtained from this study are several orders of magnitude different from the previous study (Table 2.6).

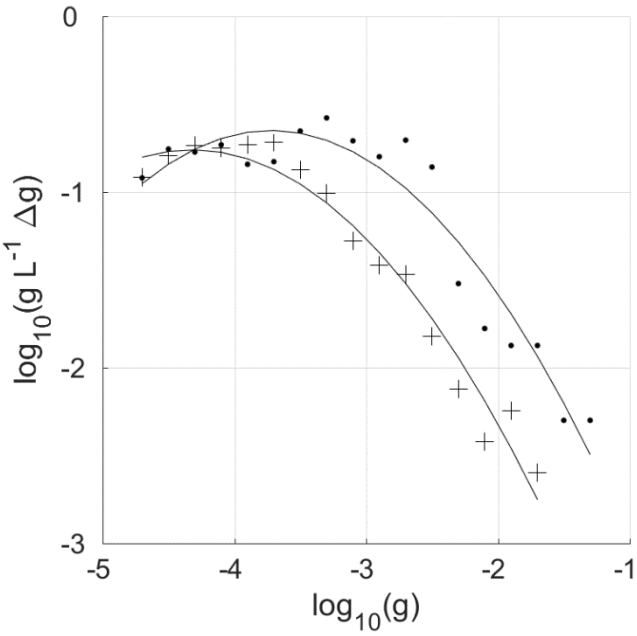

Fig. 2.25. Normalized biomass size spectra (NBS spectra) for zooplankton (•) and phytoplankton (+). Solid lines denote the dome-shaped regressions expressed as $\log_{10}(Y) = A + 0.5 \times C(\log_{10}(X) - B)^2$. The coefficients A, B, and C for each regression are shown in Table 2.6.

Table 2.6. Coefficients in the dome-shaped regressions for the normalized biomass size spectra (NBS spectra).

Location	Zooplankton			Phytoplankton			Reference
	A	B	C	A	B	C	
Izu-Oshima Is.	–0.65	–3.72	–0.63	–0.76	–4.32	–0.58	This study
Lake Superior	–0.94	–4.56	–0.38	6.90	–11.67	–0.41	Yurista et al. 2014
Lake Ontario	1.24	–6.57	–0.34	—	—	—	Sprules and Stockwell 1995
Lake Erie	1.14	–5.46	–0.82	—	—	—	Sprules and Stockwell 1995

2.4.3 Acoustic and optic backscatters

Acoustic backscattering from zooplankton has been utilized to quantify their population abundance remotely (Brierley et al. 2002). While echo sounders are typically used for this purpose (Gregg & Horne 2009), acoustic backscatter by current meters, such as Aquadopp and ADCP, also have used to ensure zooplankton dynamics (Yahel et al. 2005, Holzman et al. 2007). Since the calibration method for the acoustic backscatter by current meters has not been established, the acoustic backscatter ensured in this study represents relative changes. The wave length of the pings from the Aquadopp is roughly 3.8 mm, based on the acoustic frequency of 400 kHz and a typical sound speed of 1500 m s^{-1}. Target strength from an animal (defined as ratio between intensity of echo reflected by the animal against that of incident echo) largely depends on the size of the animal. An animal that is significantly smaller than the wave length has a negligible target strength. The body size of the observed zooplankton taxa was comparable to or smaller than the wave length (see plankton photos in Fig. 2.8). The wave length of 3.8 mm corresponds to the 80 percentile of the body size of the strong migrator; most strong migrator were smaller than this wave length. This probably resulted in the low correlation of the acoustic backscatter against the strong migrator (Fig. 2.12). Also, the wave length corresponds to the 95 percentile of the body size of the moderate migrator, probably resulting in no significant correlation between the acoustic backscatter and the moderate migrator.

While zooplankton bodies can be optical scatterers in the ocean, *in situ* measurements of zooplankton abundance utilizing optic backscatter are very rare. Dickey et al. (1991) moored optical turbidity sensors together with various sensors (e.g. thermistors, current meters, etc.) off the eastern coast of the US where the bottom depth was 100 m. The turbidity sensors were vertically distributed through the water column, and they reported night-time increases in the turbidity data with slight time lags among sensors. At dusk, the increases in upper layers were delayed against those in the lower layers, and the opposite things happened at dawn; the signals were most likely from zooplankton community performing diel vertical migration. While Dickey et al. (1991) did not have zooplankton sampling, the optical backscatter (turbidity) observed in this study also showed diel pattern showing a high correlation against the strong migrator ($r^2 = 0.79$, $p<0.01$). The results suggest that optical backscatter by turbidity sensor can be utilized as a proxy of zooplankton population abundance.

At the same time, a potential issue of the use of turbidity sensor is phototaxis

of zooplankton against light source of the turbidity sensor. The turbidity sensor emitted blue light (460 nm) in order to measure fluorescence., where the wave length typically attracts zooplankton. The influence of zooplankton phototaxis would happen even on CPICS data due to the same potential issue. Further investigations on zooplankton phototaxis against artificial light emissions from optic sensors are performed in Chapter 4.

2.4.4 Influence of current and turbulence on DVM

Diel rhythm was observed in the plankton abundance (ensured by the CPICS), the acoustic backscatter (the Aquadopp), and the optical backscatter (the turbidity sensor). These data showed significant negative correlations against the currents and turbulence (Fig. 2.19, Fig. 2.20, Fig. 2.21). The negative correlations strongly suggest that the zooplankton community which performed DVM (the moderate/strong migrator) avoided fluid disturbances.

Zooplankton in the ocean is typically attracted by light sources, while the NBS spectra ensured by the zooplankton community followed the dome-shaped regression curve (Fig. 2.25). Since the regression curve is a general feature found in any environments (Yurista et al. 2014), the bias due to the phototactic behaviors on the plankton abundance ensured by the CPICS seems to be limited. The acoustic backscatter that must not be affected by the phototactic behaviors also showed the negative correlations (Fig. 2.20a,b,c). In addition, the moderate migrator showed the negative correlations even in daytime when zooplankton individuals do not perform phototactic behaviors (Fig. 2.19d, Fig. 2.21c). Avoidance of zooplankton in response to turbulence has also been observed by net samplings (Incze et al. 2001). Even if some limited bias existed on the data acquired in night time, the results suggest that the physical disturbances suppressed the zooplankton DVM.

Chapter 3

Flow-mediated DVM observed from ADCP

3.1 Introduction

In Chapter 2, it was suggested that zooplankton avoid enhanced turbulence, and the turbulence avoidance results in suppressed Diel Vertical Migration (DVM). While the turbulence avoidance has been suggested by previous studies (Incze et al. 2001, Seuront et al. 2004, Gallager et al. 2004), the suppression of DVM due to turbulence was suggested first time in Chapter 2.

The cabled observatory OCEANS carried two instruments that emitted visible light by zooplankton. Since zooplankton is generally attracted by visible light source (phototaxis), the zooplankton data by the optic sensors would be biased. While acoustic backscatter measured by the Aquadopp was also used to demonstrate the turbulence avoidance, the backscatter near the optic sensor would be biased.

Here, the turbulence avoidance of zooplankton was tested using only acoustic data without using the optic data. The data were acquired by an ADCP that was moored without any light-emitting device near the Izu-Oshima Island. A 2-years acoustic data set by an ADCP was also available near a coastal city (Eilat) in Israel that faces to the Gulf of Aqaba, the Red Sea, provided by the Interuniversity Institute for Marine Sciences, Israel. Using the ADCP data from both Izu-Oshima Island and Eilat, I confirmed reproducibility and generality of the turbulence avoidance of zooplankton and the subsequent DVM suppression.

3.2 Materials and methods

3.2.1 Location

Filed campaigns were carried out near Izu-Oshima Island, Japan and off Eilat, Israel. See “2.2.1 Location” for details of Izu-Oshima Island. Eilat is a city located at

southern tip of Israel that faces to the Gulf of Aqaba, Red Sea (Fig. 3.1). The gulf is surrounded by deserts, and annual rain fall in Eilat is 25 mm that is about 1% of general rain fall in Izu-Oshima Island. Salinity is >40 PSU throughout the year (Manasrah et al. 2006), and annual temperature range is 21 to 26 °C in the upper 100 m off Eilat (Genin et al. 1995). The water column is stratified with $N^2 = 10^{-4}$ s^{-2} in summer (Monismith & Genin 2004), but surface mixed layer in winter reaches the deepest bottom of 1000 m in the gulf (called deep convective mixing), resulting in high temperature of >20 °C even in the depth of 1000 m (Genin et al 1995, Manasrah et al. 2006). The currents in the surface layers are associated with internal gravity tides throughout the year except winter (Monismith & Genin 2004, Carlson et al. 2014).

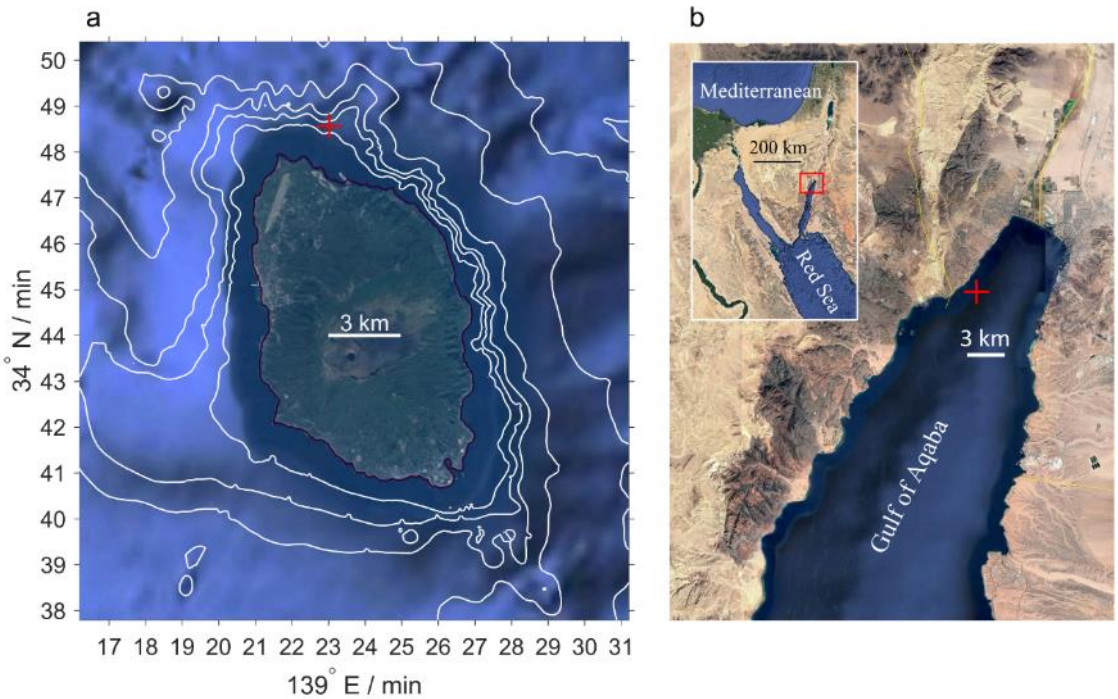

Fig. 3.1. a) Map of Izu-Oshima Island. Red cross denotes the location of the ADCP mooring. White lines denote isobaths of 100, 200, 300, 500, 1000, 1500 m. b) Same as a), but for Eilat, Israel. Subset figure shows a spatial relationship between the Gulf of Aqaba and the Red Sea.

3.2.2 ADCP

Both ADCPs were moored near the bottom or at a middle depth, looking upward. A RDI Sentinel V 500 kHz was moored off Okada Port at Izu-Oshima Island (Fig. 3.1a, Table 3.1). A RDI Work Horse 600 kHz was used for the mooring off Eilat (Fig. 3.1b). The data set from Izu-Oshima Island is hereinafter called “Oshima Data”, and that from Eilat is called “Eilat Data”. Most specifications and configurations were similar (Table 3.1), but the observation period for the Oshima Data was about 3 months while that for the Eilat Data was about 2 years. For the Eilat Data, the ADCP was replaced with a cycle of several days to several weeks due to the limitation of battery and memory. The specifications and configurations for each ADCP were maintained.

Table 3.1. Comparison of the specifications and configurations for the ADCP moorings.

Data set name	"Oshima Data"	"Eilat Data"
Start date	Apr 21 2016	Aug 04 2014
End date	Jul 19 2016	Jul 05 2016
Lattitude	34° 48' 30''	29° 30' 00''
Longitude	139° 23' 00''	34° 56' 00''
Acoustic frequency (kHz)	500	600
Ensemble interval (min)	6	10
Pings per ensemble	40	250
Water depth (m)	100	43
Instrument depth (m)	90	42.5
Bin size (m)	1	2
Number of bins	55	21
Blanking distance (m)	1	0.5

3.2.3 Data analysis

Velocity data

Current velocity data from the ADCPs were processed by a regular detection method, namely, if the ratio of valid data (%good) is lower than 80% within an ensemble, the data were rejected. For the Oshima Data, the bottom 5 layers (corresponds to 10%) were noisy and not used. For the Eilat Data, the bottom 2 layers (corresponds to 10%) were not used, and the top 10 layers (corresponds to 50%) were not used to avoid contamination from the surface process (e.g. micro bubbles). The data acquired during nighttime was used to examine the interactions between flow pattern and acoustic backscatter. The nighttime was defined as period from sunset + 0.5 h to sunrise – 0.5 h. The velocity data were decomposed into along-shore velocity and cross-shore velocity according to the bottom topography (Fig. 3.1).

TKE dissipation rate

The structure function method (Wiles et al. 2006) was applied for Oshima Data whose measurements were away from the boundaries. A second order structure function $D(z,r)$ at depth z is calculated as follows;

$$D(z,r) = \overline{(v'(z) - v'(z+r))^2}, \tag{3.1}$$

where v' is turbulent velocity component, and r is distance from z. v' is calculated as $v' = v - \bar{v}$, where v is along-beam component of the water velocity measured from each ping, and $\bar{v}$ is averaged v over each ensemble. The maximum value for r is set to 12 m as in Wiles et al. (2006). Assuming the Taylor cascade theory, D is expressed as following form;

$$D(z,r) = C_v^2 \varepsilon^{2/3} r^{2/3}, \tag{3.2}$$

where C_v is a constant (~1.45) (Wiles et al. 2006). The slope of a linear fit of $D(z,r)$ versus $r^{2/3}$ yields value for ε.

For Eilat Data, ε was estimated from friction velocity u_* assuming the law of the wall as follows;

$$\varepsilon = \frac{{u_*}^3}{kz}, \tag{3.3}$$

where k is the von Karman constant (= 0.41), and z is the distance from the bottom. u_* can be calculated by solving the following relationship between mean current $U(z)$ and u_* as follows (Drost et al. 2018);

$$U(z) = \frac{u_*}{k} ln\left(\frac{z}{z_0}\right), \tag{3.4}$$

where z_0 is bottom roughness length scale. The slope and intercept of a linear fit of $U(z)$ versus $ln(z)$ yields values for u_* and z_0, respectively. Only profiles that conservatively satisfied the assumption of a logarithmic profile (with r^2 from the linear fits >0.5) were included in the analysis, a criterion which was satisfied for approximately 41.6% of the profiles.

Acoustic backscatter

Acoustic amplitude recorded by the ADCPs was converted to acoustic backscatter from the same process mentioned in Chapter 2 (See 2.2.3 Data processing and analysis, *Acoustic backscatter*). Although the acoustic backscatter intensity was not calibrated, the data were useful to examine relative changes in backscatter (i.e. zooplankton abundance) in space and time. The acoustic backscatter by the ADCP has been used as a proxy of zooplankton abundance off Eilat (Yahel et al. 2005, Holzman et al. 2007) as well as other areas (Flagg & Smith 1989, Zhu et al. 2000).

The acoustic backscatter data includes signals from any type of scatterers including fish whose bladder is a source of strong signal. To eliminate signals from fish that is a noise for this study, a filtering process (fish filter) was newly developed, and the filter was applied for the both data sets. The ADCPs have 4 acoustic beams, and the signal from each beam is recorded separately. (A representative value at a certain depth and time is ensured by averaging the data over the beams.) Here, if an individual or a school of fish passed over the cluster of the beams, a large variation among the values by the beams would occur (Fig. 3.2); the signal from fish may be detected from this variation. In this study, the criterion is defined as follows; 1) calculate differences among the 4 beams at a certain depth and time, 2) the data is rejected if any of differences exceed a certain threshold value (Fig. 3.3). The threshold is set to 10 dB in this study. Since the distance among individuals within a school is proportional to individual body size (Huntley & Zhou 2004), the filter effectively eliminates the signal from large fishes.

Since the acoustic backscatter of the Eilat Data was very noisy probably due

to suspended sediments, an additional filter was required to separate zooplankton signals for the Eilat Data. Although acoustic wavelength is about 2.5 mm when acoustic frequency is 600 kHz (assuming a sound speed of 1500 m s^{-1}), particles much smaller than the wavelength (e.g. <0.2 mm) would greatly affect acoustic backscatter (Simmons et al. 2010). The variation among the signals by the beams was used for eliminating the noise. To quantify the variation, I calculated coefficient of variation (CV) at a certain time and depth from the values by the beams. The CV is defined as follows:

$$\mathrm{CV} = \frac{Standard\ deviation}{Mean}, \tag{3.5}$$

where the standard deviation and the mean were calculated from the values acquired by the 4 beams. Hence, the CV can be calculated for each spatial and temporal bin. Since the calculated CV values were very noisy due to the small number of samples (n = 4), an averaged CV (expressed as $\overline{\mathrm{CV}}$) is calculated over the night time and the water column. The criterion is the following; the acoustic backscatter values recorded during a night were rejected if the $\overline{\mathrm{CV}}$ at the night lowered a threshold value. The threshold value was set to 0.20 for this study. Using this filter (hereinafter CV filter), 94 nights passed out of 655 nights. The 94 nights were sampled from all seasons and both years and not biased temporally.

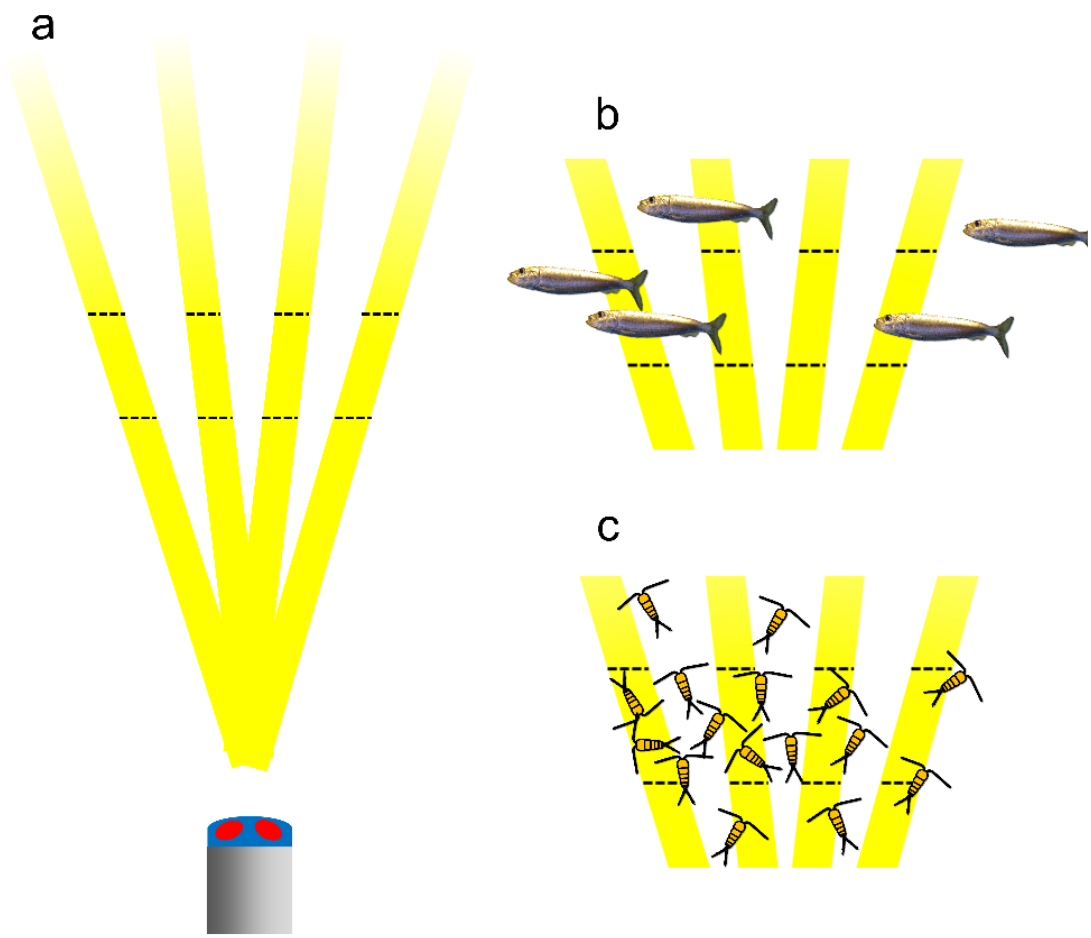

Fig. 3.2. a) Schematic diagram for the acoustic beams of the ADCP. A representative acoustic backscatter value at certain depth and time is acquired by averaging the recorded values over the beams. b) Schematic when a fish school passed over the cluster of the beams. c) Same as b) but for a zooplankton aggregation. Even if average acoustic backscatter values are the same in the cases b) and c), the variation among the values from the beams is different due to the individual body size and the spatial distribution. A fish school would cause a larger variation than that from a zooplankton aggregation.

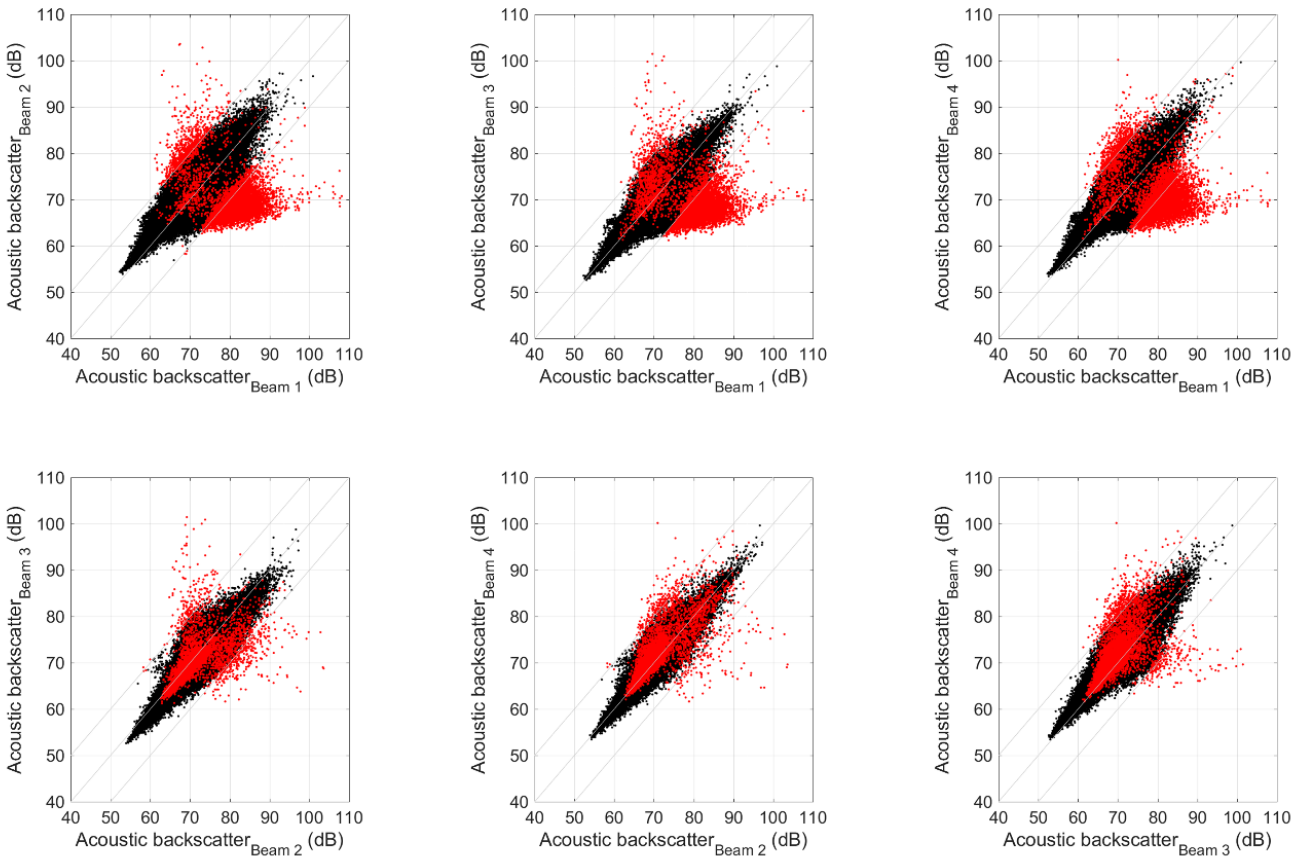

Fig. 3.3. Scatter plots for all combination from the 4 beams. Black dots denote the acoustic backscatter values that passed the fish filter. Red dots denote the values rejected by the fish filter. Solid line denotes the one-to-one relationship. Dotted lines denote that the line of the one-to-one relationship is shifted by ± 10 dB.

3.3 Results

3.3.1 Physical and biological background

For the Oshima Data, acoustic backscatter was typically lower than 60 dB but increased after July 1 2016 (Fig. 3.4b). Absolute velocity typically ranged from 0.1 to 0.3 m s^{-1} but temporally exceeded 0.5 m s^{-1} associated with surface tide (Fig. 3.4c). TKE dissipation rate ε typically ranged from $3x10^{-9}$ W kg^{-1} to $3x10^{-8}$ W kg^{-1} and rarely exceeded 10^{-7} W kg^{-1} (Fig. 3.4d).

For the Eilat Data, acoustic backscatter shows an annual cycle; the backscatter increased rapidly in Spring and decrease gradually toward the next Spring (Fig. 3.5b). The high levels of acoustic backscatter were generally found from May to September (Fig. 3.5b). Surface elevation also shows an annual cycle associated with monsoon winds acting on the Red Sea (Fig. 3.5a) (Monismith & Genin 2004). Absolute velocity is typically lower than 0.2 m s^{-1} but frequently exceeded 0.4 m s^{-1} (Fig. 3.5c). ε generally ranged from 10^{-9} W kg^{-1} to 10^{-6} W kg^{-1} (Fig. 3.5d). Estimated ε exhibited the log-normal distribution for both Oshima and Eilat Data (Fig. 3.6).

For the both data sets, acoustic backscatter shows a diel cycle (Fig. 3.7). In the Oshima Data, the backscatter rapidly increased after sunset and decreased gradually toward sunrise (Fig. 3.7a,b). The backscatter from the Eilat Data shows a similar pattern, but the range of difference between daytime and nighttime is much smaller than the Oshima Data (Fig. 3.7c,d). Also, there is a secondary peak 30 min before sunset that is common for the both data sets (Fig. 3.7a,c).

3.3.2 Acoustic backscatter and current velocity

For the Oshima Data, acoustic backscatter significantly decreased with increasing current velocity (Fig. 3.8a) if the data is only limited to the period after July 1 2016 where the backscatter is relatively strong (Fig. 3.4b). On the other hand, if the data is only limited in the period before July 1, the decrease was not found (Fig. 3.8b).

After the CV filter for the Eilat Data, acoustic backscatter significantly decreased with increasing current velocity (Fig. 3.9a) even if the data is from the entire observation period (Fig. 3.5). If the CV filter was not applied, the decrease disappeared (Fig. 3.9b).

Even if the ranges of absolute velocity and acoustic backscatter were different between the two data sets (<1.0 m s^{-1} and 50 to 80 dB for the Oshima Data; <0.3 m s^{-1} and 55 to 90 dB for the Eilat Data), the trends in acoustic backscatter against the absolute velocity were similar (Fig. 3.8a, Fig. 3.9a). Acoustic backscatter

also significantly decreased with increasing turbulent level for the both data sets (Fig. 3.10).

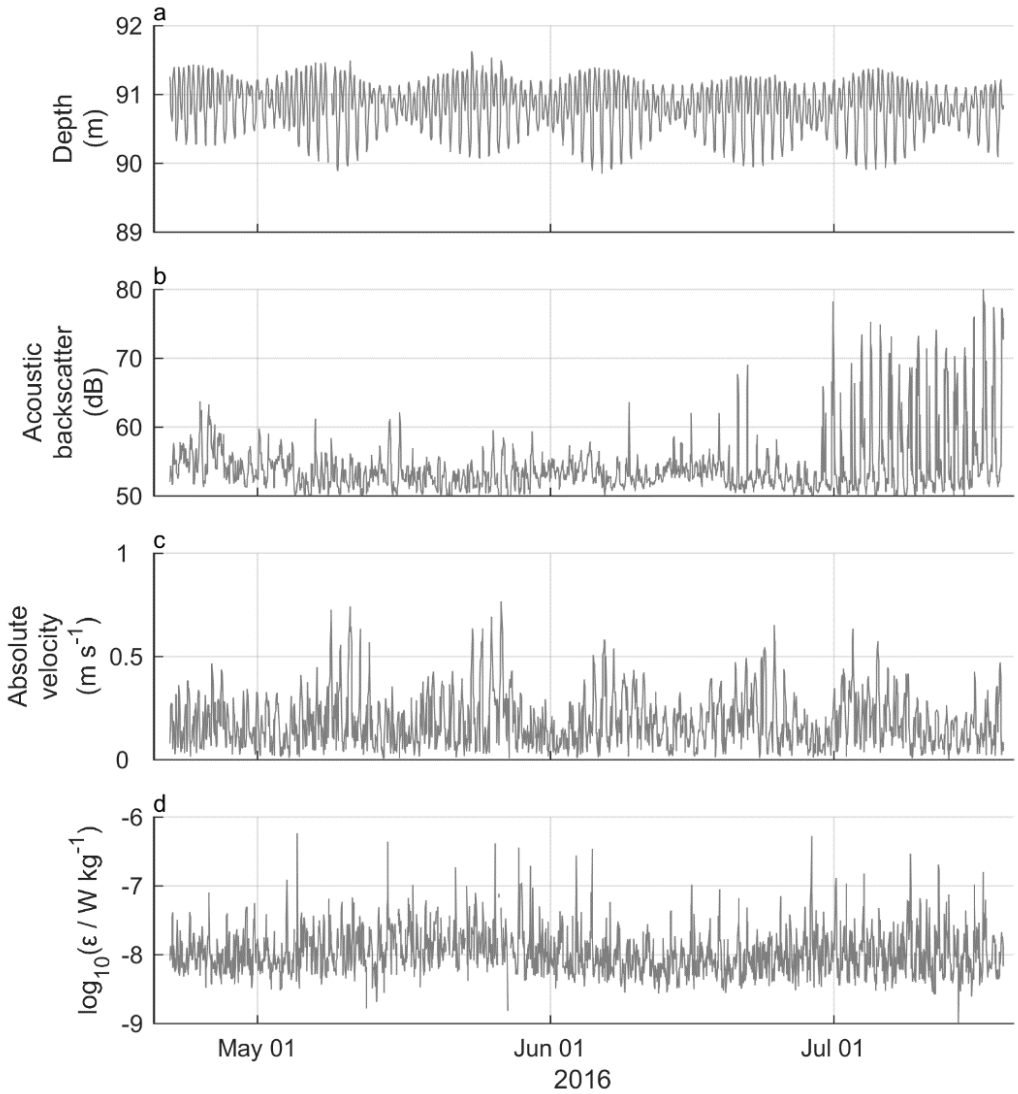

Fig. 3.4. Time-series for Oshima Data. Data except the depth is from the layer of 30 MAB.

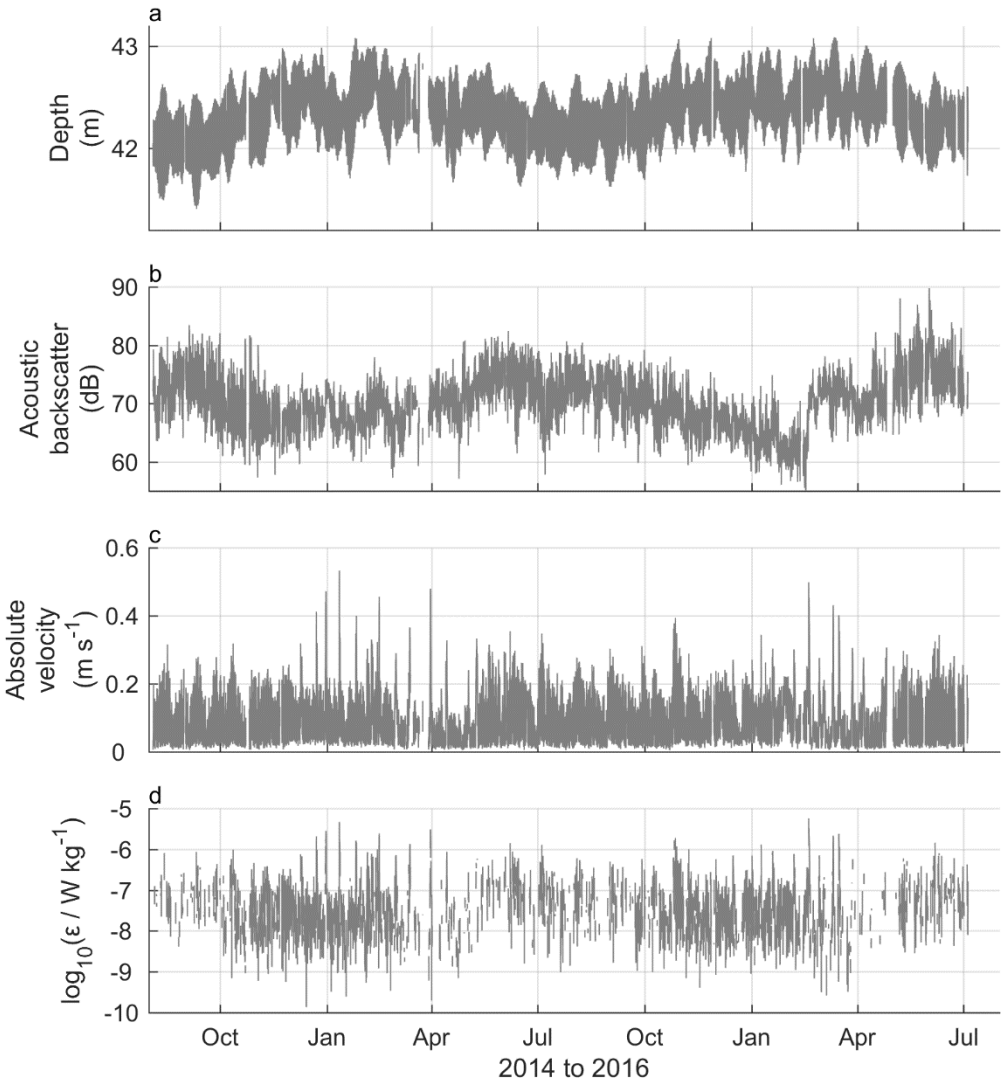

Fig. 3.5. Time-series for Eilat Data. Data is from the layer of 10 meters above the sensor except the depth.

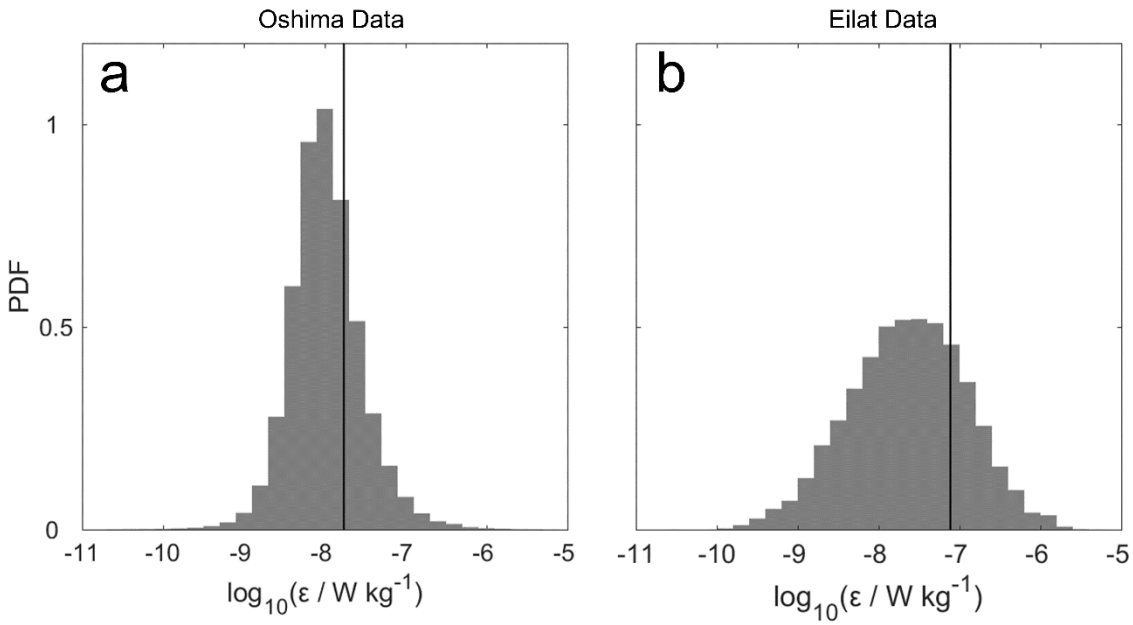

Fig. 3.6. PDF of TKE dissipation rate ε for a) Oshima Data and b) Eilat Data. Vertical solid lines denote average values, 1.7×10^{-8} W kg^{-1} for Oshima Data and 7.7×10^{-8} W kg^{-1} for Eilat Data.

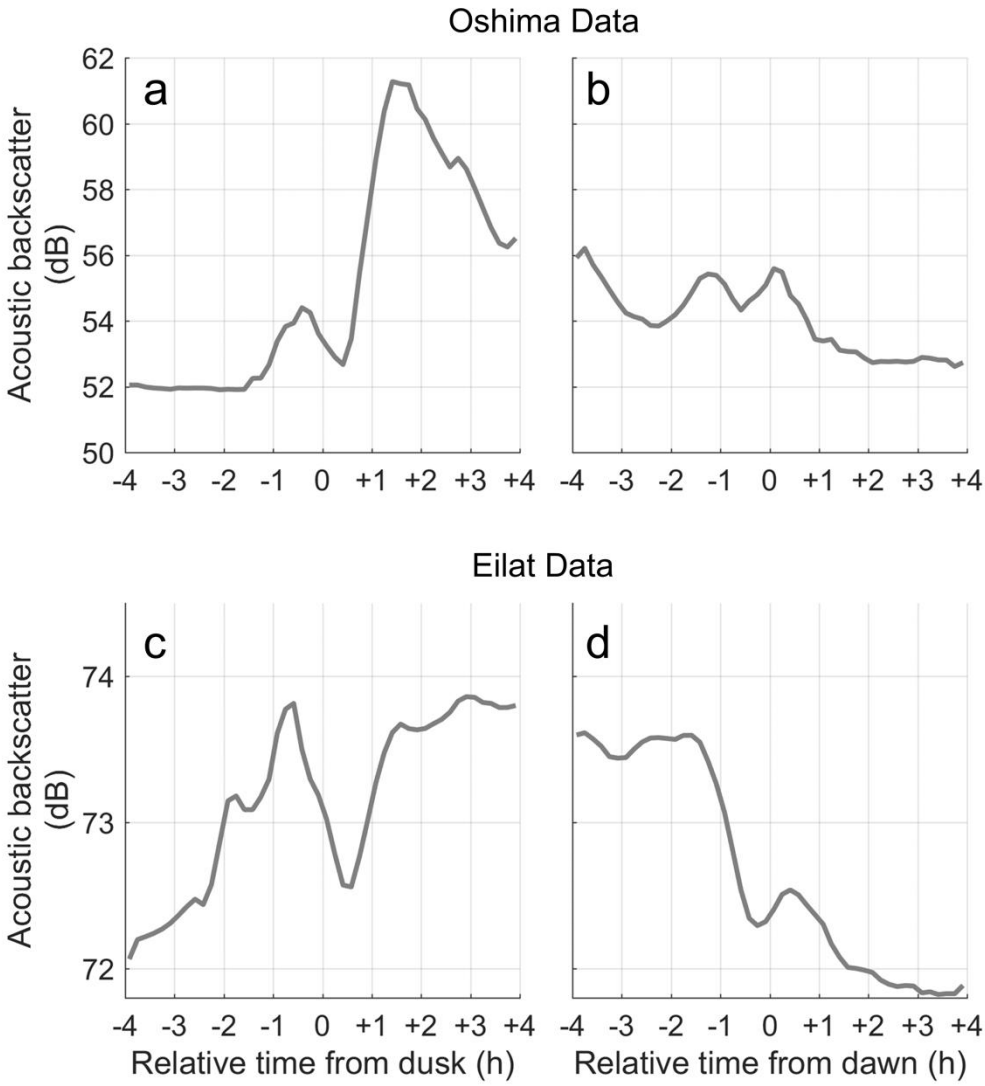

Fig. 3.7. Acoustic backscatter averaged around dusk (a) and dawn (b) with 10-min bins for the Oshima Data. c,d) Same as a,b) but for the Eilat Data.

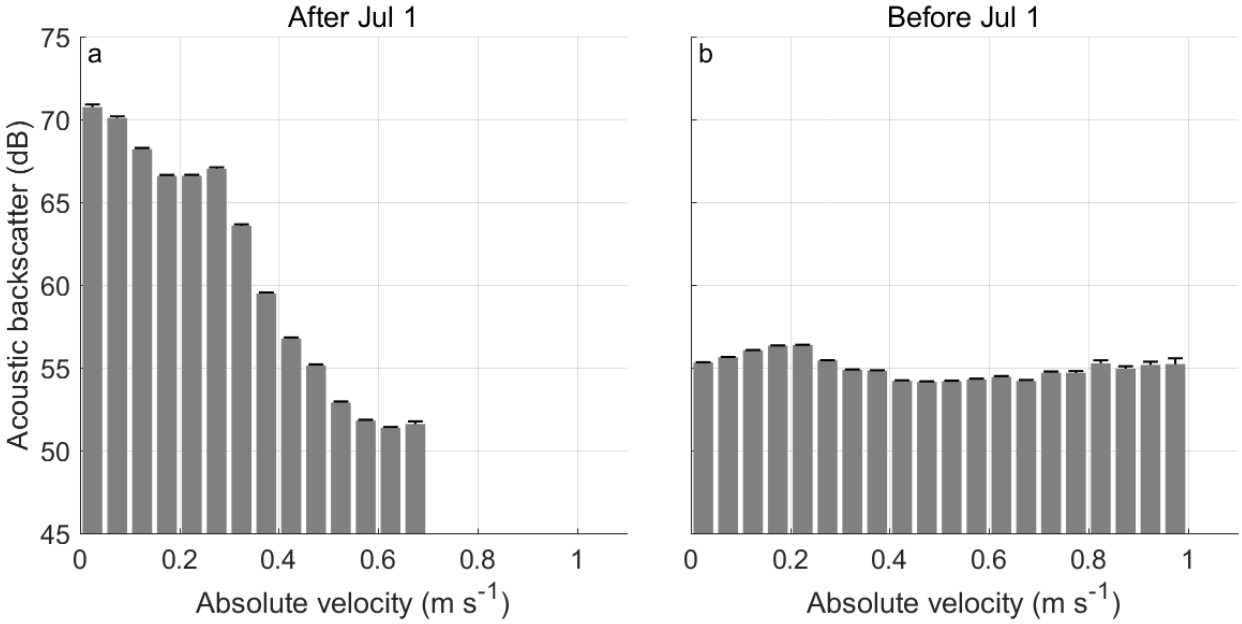

Fig. 3.8. Bar plots of nighttime acoustic backscatter averaged over different velocity levels for a) the former period (after July 1) and b) the later period (before July 1). Error bars denote standard errors.

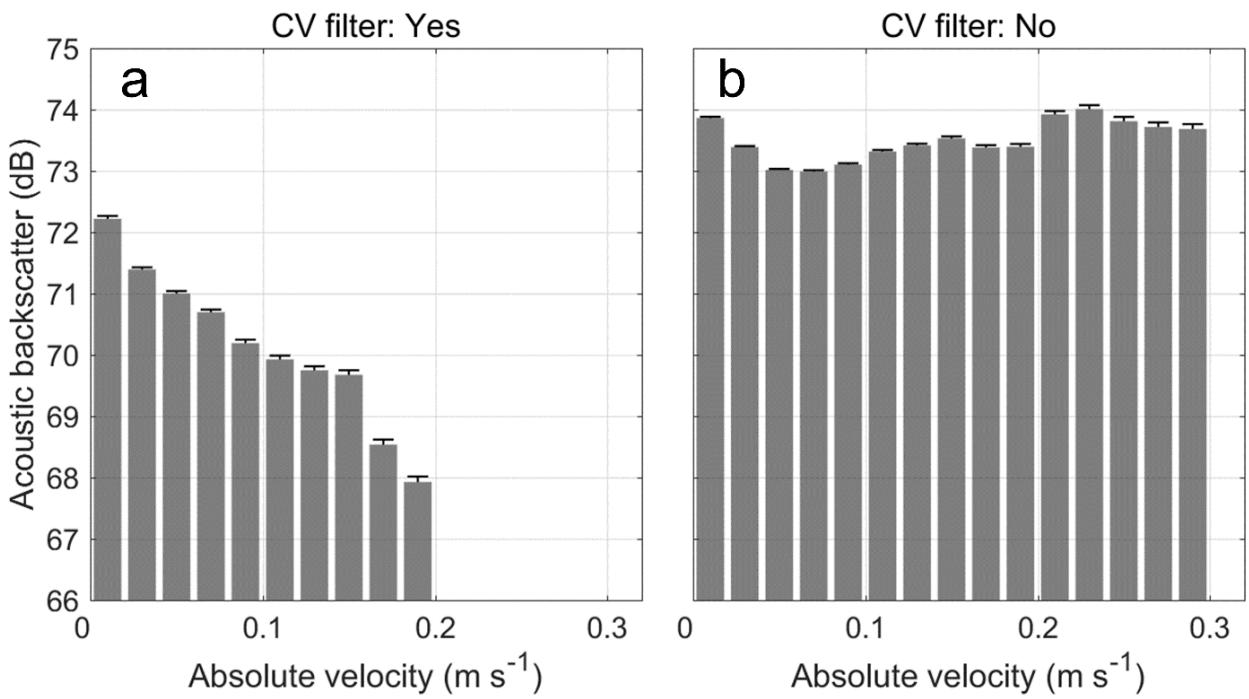

Fig. 3.9. Bar plots of nighttime acoustic backscatter averaged over different velocity levels a) with using the CV filter and b) without using the filter. Error bars denote standard errors.

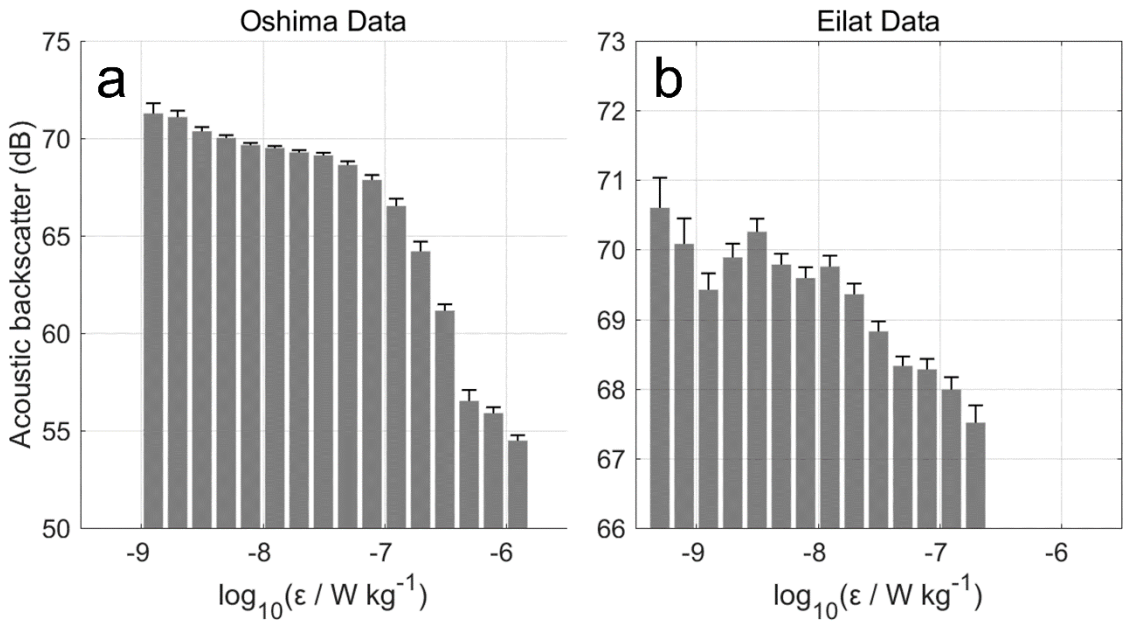

Fig. 3.10. Bar plots of nighttime acoustic backscatter averaged over different turbulent levels for a) Oshima Data and b) Eilat Data. Error bars denote standard errors.

3.4 Discussion

While the physical processes at the both observation sites were different (Fig. 3.4, Fig. 3.5), acoustic backscatter significantly decreased against current velocity (Fig. 3.8a, Fig. 3.9a) and turbulent level (Fig. 3.10). At the Oshima observation site, strong current velocities (>0.5 m s^{-1}) were synchronized with large variations in surface tides (Fig. 3.4a,c), probably affected by internal gravity waves that are generated by surface tides and the complex topography around the island (Fig. 3.1a) (Masunaga et al. 2017). At the Eilat observation site, current velocity was generally below 0.3 m s^{-1} that is consistent with previous field surveys (Reidenbach et al. 2006, Monismith & Genin 2004). While the stratification at the observation site is generally the same as or much weaker than typical stratifications in the open ocean (Thorpe 2007), the current is greatly affected by internal gravity waves which are generated at the Strait of Tiran where density-driven exchanges between the gulf and the Red Sea occur (Fig. 3.1b) (Monismith & Genin 2004). TKE dissipation rates ε estimated from the structure function method and the friction velocity u_* exhibited the log-normal distributions for the both data sets (Fig. 3.6). Averaged ε of 1.7×10^{-8} W kg^{-1} for the Oshima Data is almost the same level as the averaged ε in the open ocean (Thorpe 2005), while the averaged ε of 7.7×10^{-8} W kg^{-1} in the Eilat Data is one-order smaller than previously reported average value of 10^{-6} W kg^{-1} at 1 mab (Reidenbach et al. 2006).

Zooplankton community for the Oshima Data is expected to be similar to that observed by the cabled observatory located at the southern part of the island (see Fig. 2.8 in Chapter 2). The community for the Eilat Data was not observed in detail for this study but, in general, composed of the pelagic community which is dominated by calanoid copepods and the neritic community which is a mixture of reef-originated zooplankton and demersal zooplankton (Yahel et al. 2005, Sommer et al. 2002, Echelman & Fishelson 1990). Acoustic backscatter in the Eilat Data showed a seasonal trend that high levels of acoustic backscatter were generally found between May and September (Fig. 3.5b). The seasonal peaks in May and June (Fig. 3.5b) appeared to follow phytoplankton spring blooms generally found in March to middle April (Genin et al. 1995, Lindell & Post 1995).

Although two observation sites were spatially and environmentally separated, acoustic backscatter which is proportional to local zooplankton abundance (Flagg & Smith 1989) decreased with increasing current velocity and turbulent level (Fig. 3.8a, Fig. 3.9a, Fig. 3.10). This trend is clearly consistent with the results from Chapter 2 (see Fig. 2.18, Fig. 2.19, Fig. 2.20) which showed

significant decrease in zooplankton abundance with increasing current velocity and turbulent level. Also, the previous field/experimental studies have demonstrated the turbulence avoidance by various types of zooplankton. Seuront et al. (2004) used freshwater-cultured *Daphnia pulicaria* (~2 mm) and oceanic calanoid copepod *Temora longicornis* (~1 mm) that was collected from the Eastern English Channel for their tank experiments, and the both species showed active escape reactions with increasing turbulence intensity. Gallager et al. (2004) observed by a 3-dimensional video plankton recorder in Georges Bank that most zooplankton taxa including *Calanus* spp., *Oithona* sp., and *Pseudocalanus* sp. were significantly aggregated only when their swimming speed significantly exceeded rms turbulent velocity. Incze et al. (2001) found that copepodite stages of *Temora* spp., *Oithona* spp., *Pseudocalanus* spp., and *Calanus finmarchicus* avoided high turbulent levels in the surface mixed layer associated with increased wind stress, based on net samplings and microstructure measurements in Georges Bank. In the North Sea, Visser et al. (2001) found that *Oithona similis* avoided strong turbulent levels in the surface mixed layer, using net samplings and microstructure measurements. Although no avoidance was found in some zooplankton due to species or life stages (Incze et al. 2001, Visser et al. 2001), various types of zooplankton from the different geographic locations exhibited turbulence avoidance (Seuront et al. 2004, Gallager et al. 2004, Incze et al. 2001, Visser et al. 2001) which is consistent with this study (Fig. 3.8a, Fig. 3.9a, Fig. 3.10).

The zooplankton abundance observed in Chapter 2 would be biased due to positive phototaxis that is common among oceanic zooplankton (Tranter et al. 1981, Meester & Dumont 1989, Storz & Paul 1998, Jékely et al. 2008, Ma & Johnson 2017), and, hence, it has been critical whether the decrease in abundance was caused by active avoidance or passive dispersion by turbulence and currents. If zooplankton migrate toward the artificial light of the instrument, the estimated abundance would be larger than the natural condition, and zooplankton would be flushed away by currents or dispersed by turbulence, consequently exhibiting the decreases in abundance as in Fig. 2.18, Fig. 2.19, and Fig. 2.20. However, the mooring systems used in this chapter did not carry any light-emitting device, and the zooplankton abundance was implied by acoustic backscatter, not optical data. Hence, I conclude that the zooplankton avoidance is a real phenomenon which is common both in the seas around Izu-Oshima Island and off Eilat.

3.5 Conclusion

The two upward-looking ADCP moorings deployed nearby the Izu-Oshima Island and off Eilat, Israel successfully observed current velocity and acoustic backscatter from the water columns (the Oshima Data and Eilat Data). The objective of this study was to confirm the consistency of the turbulence abundance by zooplankton observed in Chapter 2, using acoustic instruments without any light-emitting devices at different geographic locations. TKE dissipation rates were estimated from the structure function method for the Oshima Data and from the law of the wall for the Eilat Data. Since the value of acoustic backscatter reflects signals from all potential scatterers, not only zooplankton (e.g. fish, bubble, sediments), filters that utilized the acoustic backscatter differences among 4 beams were applied to extract signals which were most likely from zooplankton. After the filtering processes, the acoustic backscatter showed nighttime increases which most likely reflected diel vertical migration of pelagic zooplankton or nighttime emergence of demersal zooplankton in the both data sets. While the two observation sites were spatially and environmentally separated, acoustic backscatter significantly decreased with increasing current velocity and turbulent level for the both data sets. The results from the ADCP moorings strongly supported the results from Chapter 2 that suggested the turbulence avoidance by individual zooplankton.

Chapter 4

Zooplankton phototaxis to optic sensor

4.1 Introduction

Zooplankton in the ocean generally show positive phototaxis toward visible light source. In general, a fluorescence sensor uses blue light, therefore, zooplankton may be attracted to the turbidity sensor. On the other hand, a turbidity sensor normally uses infrared light that is invisible to zooplankton. However, turbidity sensor receives optical backscatter from suspended particles in the water column. If aggregation of zooplankton is present, the turbidity signals may be contaminated by the zooplankton aggregate.

Optic sensors are used to measure water turbidity and fluorescence (a proxy of chlorophyll). For this purpose, the sensors generally carry light-emitting and receiving parts, and optic backscatter from particles (suspended solid, phytoplankton cell, etc.) is used for estimating suspended solid or chlorophyll concentration. Major manufactures use blue light (450 to 495 nm) for fluorescence measurement; for example, RINKO-profiler (JFE Advantech, 460 nm), Water Quality Monitor (Sea-Bird Scientific, 470 nm). Those sensors also carry a turbidity sensor nearby the fluorescence sensor, and the sampling volume is typically shared by the both turbidity and fluorescence sensors.

Phototaxis of zooplankton have been studied in fields (Tranter et al. 1981, Meester & Dumont 1989, Storz & Paul 1998, Jékely et al. 2008, Ma & Johnson 2017). Most studies demonstrated positive phototaxis toward visible light source (Tranter et al. 1981, Meester & Dumont 1989, Storz & Paul 1998, Jékely et al. 2008, Ma & Johnson 2017), while some animals show negative phototaxis (Ma & Johnson 2017). The reason for the positive phototaxis is not well understood yet, but phototaxis seems to enhance mating rates.

Several limnologic studies have reported nighttime increases in turbidity data measured by optical sensors at inland rivers (Rice et al. 2016, Loperfido et al. 2010). The nighttime turbidity increased by 10 times from daytime value on average (Loperfido et al. 2010), concluding the water turbidity was elevated by biological activities in the rivers (Rice et al. 2016, Loperfido et al. 2010). However, diel pattern of turbidity is rarely reported in the ocean (e.g. Dickey et al. 1991).

In addition, the effect of background current velocity on phototactic behavior is elusive. While swimming velocity of zooplankton is in general much faster than turbulent velocity in the upper layers (Yamazaki & Squires 1996), the effect of the background hydrodynamics on the phototactic behavior has not been tested.

The purposes of this study are investigations on 1) the effects of phototactic behavior in turbidity data and 2) the effects of the background hydrodynamics on phototactic behaviors. A series of laboratory experiment was conducted using a zooplankton natural community collected from the ocean as well as cultured zooplankton.

4.2 Materials and methods

4.2.1 Sensor

A RINKO-profiler manufactured by JFE Advantech was used for this study. The RINKO-profiler carries a turbidity/fluorescence sensor (a combined unit), as well as a conductivity/temperature sensor, a dissolved oxygen sensor, and a pressure sensor (Fig. 4.1). The turbidity/fluorescence sensor emit a blue-light beam (460 nm) for the fluorescence measurement and an infrared-red beam (880 nm) for the turbidity measurement, sharing a sampling volume of 4 mL (Fig. 4.1b). The blue-light beam is visible for the most zooplankton in the ocean. The sampling frequency was set to 10 Hz for the following experiments.

4.2.2 Experimental setup

Two types of laboratory experiments were carried out. The first experiment (hereinafter Experiment A) is designed to investigate the effect of zooplankton phototactic behavior on turbidity data with altering the abundance, using a zooplankton natural community (mostly copepods). Experiment B is designed to investigate the effect from ambient current velocity on zooplankton's phototactic behavior and the turbidity data, using cultured *Artemia Salina*.

Experiment A. Zooplankton were collected from a coastal region off São Paulo State, Brazil. A plankton net (100 μm mesh) was towed throughout the water

column during daytime where the bottom depth was 5 m. Individuals were classified at the level of species, and the community was mostly composed of copepods (Table 4.1). The community was used for the experiment within 24 h after the sampling.

RINKO profiler was fixed in an experimental tank with the zooplankton natural community (Fig. 4.2). Filtered seawater that was collected nearby the sampling location was put in the tank (7.8L). The tank was made from acrylic glass to eliminate shades in the tank under room light condition. The temperature and the salinity were 23.1 °C and 34.7 PSU, respectively. The room light intensity was 460 lux in an experimental room. When turbidity signals were collected, the room light was turned on/off alternatively every 3 min, making two dark periods during the entire duration of 15 min. Three measurements were carried out with different packing densities of 430, 870, and 1300 individuals L^{-1} (called Experiment A1, A2, and A3, respectively) (Table 4.2). Videos were taken by a smart phone camera during the measurements. A control experience was carried out under dark condition with only the filtered seawater, without zooplankton.

Experiment B. A. Salina individuals were hatched and kept in chambers, under room light condition. The nauplius larva were used for the experiment within 24 hours after hatching. The individuals were fed until the experiment to eliminate the effect of hunger on phototactic behaviors (Meester & Dumont 1989).

RINKO-profiler was fixed in a beaker filled with artificial seawater (1 L) (Fig. 4.2). The temperature was 28.5 °C, and the salinity was 18.9 PSU that was lower salinity than their natural environments (Vanhaecke et al 1987). The abundance of *A. Salina* was set to be 1850 ind L^{-1}. A tube was installed to generate turbulent flow in the beaker by aeration (Fig. 4.2). The end of the tube was located at a bottom corner to generate a circulation without contaminating data by air bubbles. The experiment was carried out under dark condition, and the aeration was started occasionally to imitate strong levels of turbulence in the ocean.

Videos were taken by a smart phone camera during the measurements, with a pixel resolution of 0.05 mm pix^{-1} and a frame rate of 30 fps. Individuals as well as non-living passive particles (i.e. egg shells after hatching, fecal pellets) were detected using an image processing software, ImageJ. Time-series of current velocity was ensured based on the cross-correlation method (Catton et al. 2011). The spatial displacement of particles between successive two images can be found by calculating cross-correlation of 2-D brightness data. The calculation region was 100 x 100 pixels (corresponds to 5 x 5 mm), where the center of calculation region was 1 cm below the turbidity/fluorescence sensor same location as the sampling volume. The maximum

lag for the vertical and horizontal displacements is set to 50 pixels. Hence, the minimum and maximum detectable velocities are 0.15 cm s^{-1} and 10.6 cm s^{-1}, respectively. Noise velocity from trajectories of swimming individuals were removed, and hence velocity calculation was based on the passive particles. Only two components of the current velocity (u and w) can be calculated from the method. For calculating 3-D absolute velocity, the horizontal velocity u is used as another horizontal component v, assuming u and v are statistically in the same magnitude.

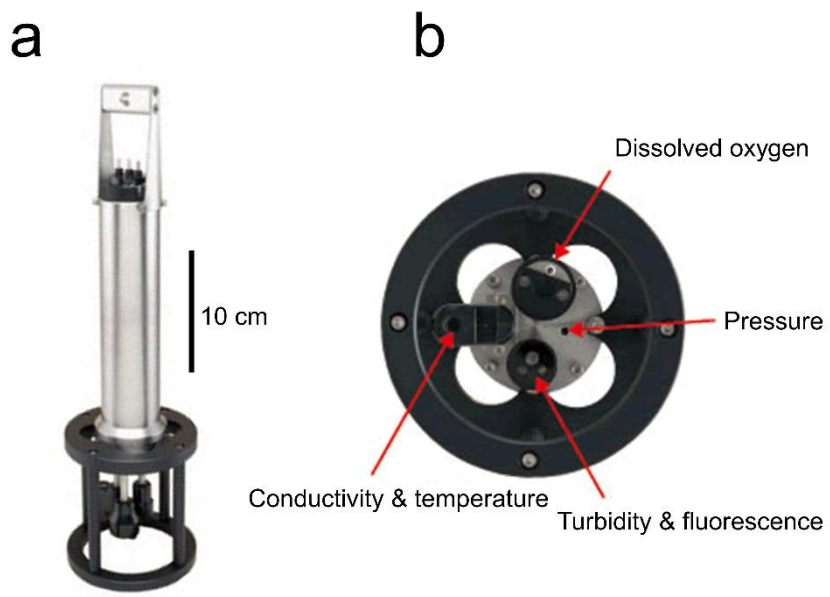

Fig. 4.1. RINKO-profiler. a) The height of the instrument is about 40 cm. The sensors are positioned at the lowest part of the instrument. b) The bottom view of RINKO-profiler. The photos are from the manufacture's website (http://www.jfe-advantech.co.jp/).

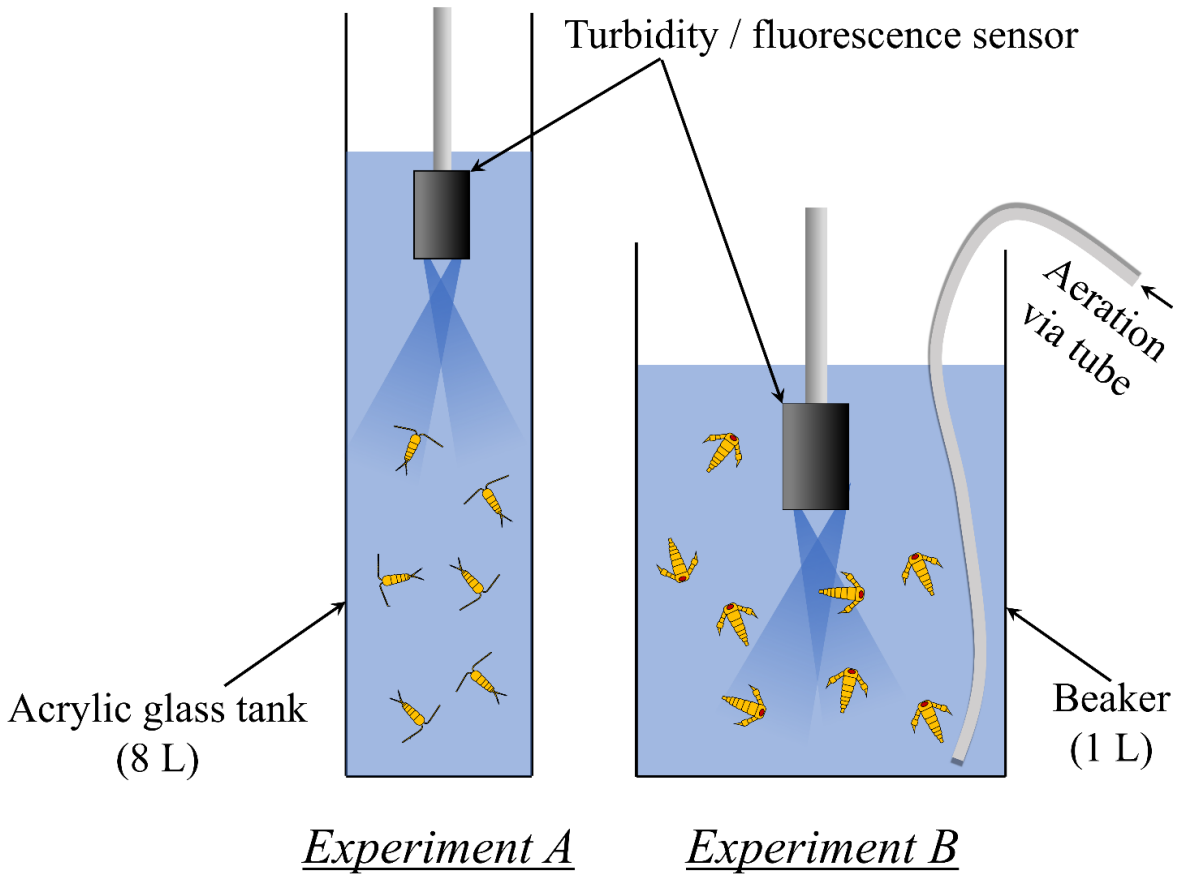

Fig. 4.2. Schematics for Experiment A and B. The schematics are not drawn in scale.

Table 4.1. Composition of zooplankton natural community collected from a coastal region off São Paulo State, Brazil that was used for Experiment A.

Species	Ratio (%)
Acartia lilljeborgi	76
Pseudodiaptomus acutus	14
Oithona oculata	5
Oithona hebes	2
Temora turbinata	1
Paracalanus quasimodo	1
Euterpina acutifrons	1

Table 4.2. Comparison of experimental settings for Experiments A and B.

Experiment name	Experiment A	Experiment B
Zooplankton	Ntural community	*A. Salina*
Packing density (individuals L^{-1})	Altered (430 → 870 → 1300)	1850
Stirrer	No	Yes

4.3 Results

Turbidity data increased significantly under dark condition even when the abundance was set to a low value (430 ind L^{-1}) (Fig. 4.3a). Turbidity was below 1 FBU under the light condition (0 to 3 min in Fig. 4.3a). After the light condition was switched to the dark condition (3 to 6 min in Fig. 4.3a), local peaks appeared on the turbidity data that lifted the average value. The dark condition was again switched to the light condition, and then, the turbidity decreased to the same value as before (6 to 9 min in Fig. 4.3a). The same increase in the turbidity data was found in the second dark condition (9 to 12 min in Fig. 4.3a), as well as in the measurements with higher packing densities of 870 ind L^{-1} (Fig. 4.3b) and 1300 ind L^{-1} (Fig. 4.3c). Active accumulations of zooplankton near the sampling volume were found under the dark conditions (Fig. 4.3d,e).

To compare the effect of different packing densities, average and standard deviation of the turbidity values were calculated over the last 1 min of the dark conditions for each measurement (5 to 6 and 11 to 12 min in Fig. 4.3a,b,c). While the background value from the control experiment (just from the filtered seawater) was 0.17 FBU, the turbidity with the low abundance (430 ind L^{-1}) was 1.02 FBU, about 6 time increase from the background (Fig. 4.4). While the turbidity increased to 2.23 FBU for the middle abundance (870 ind L^{-1}), the measurement with the highest abundance (1300 ind L^{-1}) did not show further increase in the turbidity where the average was 2.26 FBU (Fig. 4.4).

During Experiment B, the individuals of *A. Salina* accumulated near the sampling volume of the turbidity/fluorescence sensor as in Experiment A. The turbidity data was about 30 FBU after the packing density around the sampling volume was saturated (see 10 s in Fig. 4.5a). Total are of the detected particles in the still images (including living and non-living) was correlated with the turbidity at a statistically significant level ($r^2 = 0.96$, $p<0.01$; Fig. 4.5a,c). When the currents were generated by the stirrers, the current velocity reached 3 cm s^{-1} (20 to 40 s and 80 to 100 s in Fig. 4.5b), flushing the individuals around the sampling volume away. The turbidity and the total area of the detected particles suddenly decreased to the background level associated with the increased current velocity (Fig. 4.5a,b). The turbidity data is negatively correlated with the current velocity ($r^2 = 0.40$, $p<0.01$; Fig. 4.5d).

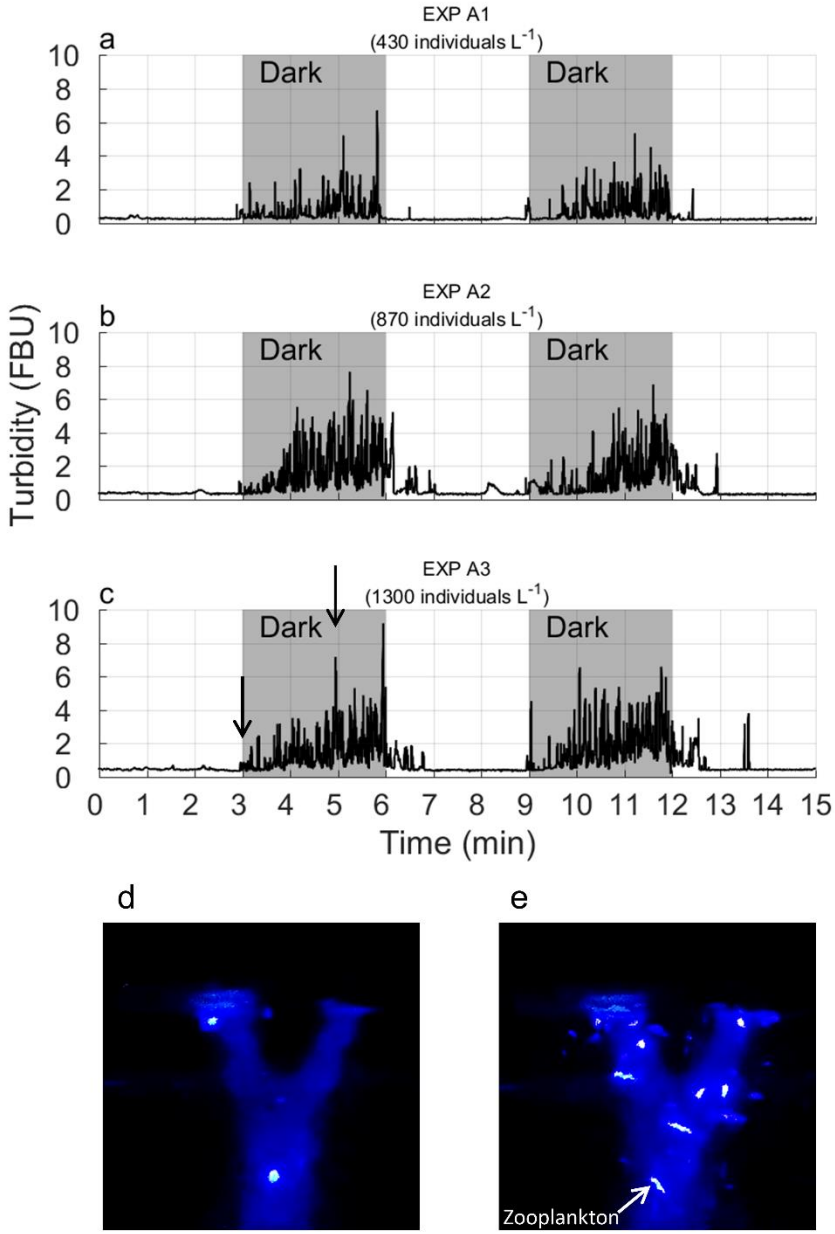

Fig. 4.3. a) Time-series of the turbidity data with a packing density of 430 ind L^{-1}. The room light was turned on except the light gray periods that show dark conditions (3 to 6 and 9 to 12 min). b) Same as a) but for a different packing density of 870 ind L^{-1}. c) For a packing density of 1300 ind L^{-1}. d) A still image taken just after the room light was turned off, shown by the left arrow in c). e) A still image taken at the middle of the dark condition, shown by the right arrow in c). Turbidity increased due to zooplankton that actively accumulated near the turbidity/fluorescence sensor.

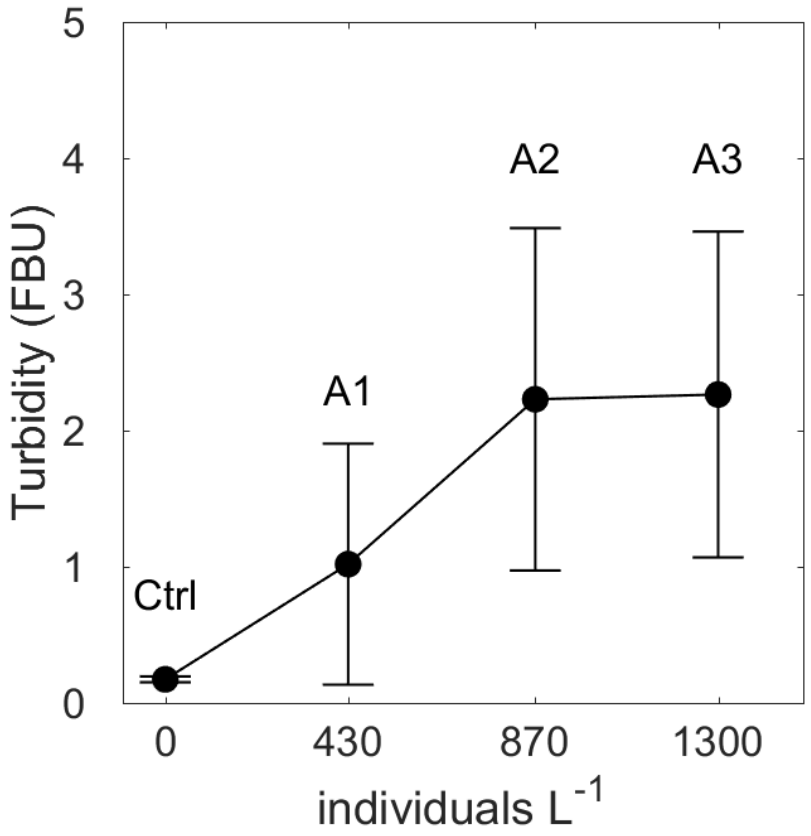

Fig. 4.4. The comparison of the effect of different zooplankton abundances on turbidity data. Black filled circles denote average value over the last 1 min of the dark conditions (5 to 6 and 11 to 12 min in Fig. 4.3). Error bars indicate 1 standard deviations.

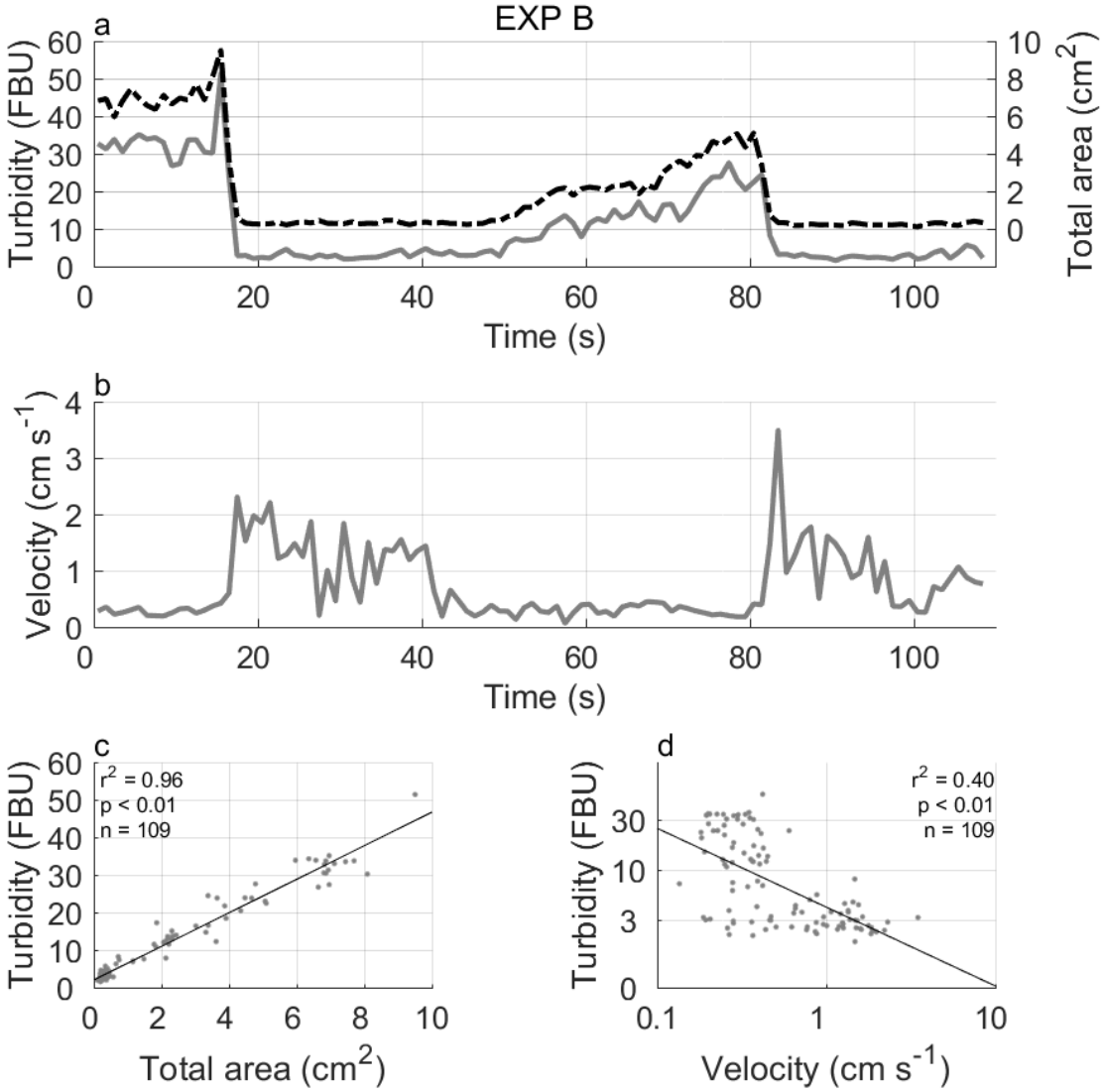

Fig. 4.5. a) Gray solid line denotes the turbidity. Black dotted line denotes the total area of the detected particles. b) Time series for the absolute current velocity calculated by the image processes. c) Scatter plot of the total area of the detected particles against the turbidity data, showing strong positive correlation ($r^2 = 0.96$, $p<0.01$). d) Scatter plot of the absolute current velocity against the turbidity data, showing negative correlation ($r^2 = 0.40$, $p<0.01$).

4.4 Discussion

The results from the experiments suggest that 1) zooplankton individuals are attracted by light emission (blue color, 460 nm) from the turbidity/fluorescence sensor, 2) zooplankton accumulation around the sensing part results in turbidity increase by up to 2 FBU higher than the background turbidity (confirmed from natural zooplankton community), and 3) zooplankton individuals are flushed away and cannot swim against strong currents even if they are attracted by the light.

The natural zooplankton community collected from a coastal region off São Paulo for Experiment A was mainly composed of copepods and classified at a level of species (Table 4.1). The most abundant two calanoid species *Acartia lilljeborgi* and *Pseudodiaptomus acutus* were common species in the coastal region off Brazil (Melo et al. 2010, Lopes 1994). Other species with relatively small abundances have also been sampled off Brazil (Melo et al. 2010, Lopes 1994). The water temperature and salinity during the experiments (23.1 °C and 34.7 PSU) are typical off Brazil in summer (Campos et al. 2000). Cultured *Artemia Salina* used for Experiment B originally inhabit highly saline lakes (>100 ‰) (Vanhaecke et al. 1987), and the water used for the experiment is much less saline (18.9 PSU) in comparison with their natural environment (Vanhaecke et al. 1987). I confirmed that the individuals foraged their food (Spirulina) and swam actively in the tank, by visual inspections. The packing density for Experiments A and B that ranged from 430 to 1850 individual L^{-1} (Table 4.2) is unusually high in comparison with natural packing density, while the same magnitude of density is rarely found in the natural environment (Heidelberg et al. 2004).

While the intensity of the light emission from the turbidity/fluorescence sensor is not strong in comparison with the sun light, the light emission stands out under dark conditions (e.g. nighttime, deep layers). Blue light (435 to 480 nm) is generally used for measurement on *in situ* fluorescence. Recent instruments carry both turbidity and fluorescence sensors on the same platform, and a shared sampling volume is frequently adopted. JFE Advantech's Infinity-CLW is designed for long-term *in situ* measurements on turbidity and fluorescence and has a shared sampling volume for the measurement which is a same type as RINKO-profiler used in this study. Sea-Bird Scientific's Water Quality Monitor is also designed for long-term mooring. The sampling volumes for turbidity and fluorescence measurements are not shared but spatially very close (<10 cm). Since blue light is visible by various zooplankton and induces their behavioral response (Buskey & Swift 1985),

phototactic behavior of individual zooplankton would affect turbidity data recorded by those instruments which have been designed and used for long-term measurements (Fig. 4.3). In addition, even when the instruments are used as a profiler, zooplankton individuals would reach the sensor's light source if the profiling speed is slower than individual's swimming speeds that could reach 10 cm s^{-1} (Buskey & Swift 1985).

I found that only a part of the entire zooplankton community was attracted by the light source. According to the previous studies, individual's life stage and nutrient condition determine if the individual shows positive phototactic behavior (Meester & Dumont 1989). However, turbidity significantly increased throughout the experiments due to accumulation of individuals around the sensor (Fig. 4.3, Fig. 4.5). The background turbidity was observed as 0.17 FBU for the control experiment of Experiment A (Fig. 4.4). The turbidity increased by about 1 FBU for Experiment A1 (430 individuals L^{-1}) and 2 FBU for A2 (870 individuals L^{-1}) (Fig. 4.4). However, the elevation remains 2 FBU for A3 (1300 individuals L^{-1}). This can be explained by the sampling volume of the turbidity/fluorescence sensor. Zooplankton individuals hovering in the sampling volume of 4 mL are only sensed by the sensor, so there is a limitation how many individuals can be hovering in the sampling volume. Zooplankton, in general, can sense the distance between neighbors from fluid signals (Kiørboe 2008) and keep a significant distance in their swarm (Haury & Yamazaki 1995, Mackie & Mills 1983). Even if they are attracted by the light source, they may keep a preferred distance from neighbors. Hence, maximum zooplankton abundance in the sampling volume would be limited by the biological reason.

The maximum elevation of 2 FBU which was observed from the natural zooplankton community does not explain the nighttime increase in turbidity (>50 FBU) observed in Chapter 2 (Fig. 2.13c,d). In Experiment B which used cultured *A. Salina* with abundance of 1850 individual L^{-1}, the turbidity elevation of 30 FBU was observed due to the accumulation around the sensor (see around 10 s in Fig. 4.5a), better explaining the nighttime increase observed in Chapter 2 (Fig. 2.13c,d). This suggest that the community structure (which species compose the community) may affect how effectively zooplankton community changes turbidity value. The 2 FBU difference due to natural zooplankton community is much smaller than turbidity fluctuations in coastal regions (Jafar-Sidik et al. 2017, Constantin et al. 2016) or inland rivers (Rice et al. 2016, Loperfido et al. 2010) but would be larger than that in the open ocean (Takata et al. 2008).

During Experiment B, individuals of *A. Salina* which were accumulated

around the sensor were flushed away by the generated current (Fig. 4.5a,b,d). This experiment simulated the observed negative correlations between velocity and turbidity in Chapter 2 (Fig. 2.19d,e and Fig. 4.5). Hence, the *in situ* decrease in zooplankton abundance with increasing current velocity could be explained by the combination of the phototaxis of the zooplankton and the currents that flush them away. On the other hand, the decrease in acoustic backscatter with increasing current velocity observed by the ADCP moorings in Chapter 3 cannot be explained by the zooplankton phototactic behavior, since the data was acquired only from acoustic devices. Thus, even if the data from the observatory is affected (biased) by the zooplankton phototaxis at a certain level, the main conclusion from Chapters 2 and 3 does not change.

4.5 Conclusion

Two experimental campaigns were carried out to confirm/evaluate 1) phototactic behavior of zooplankton individuals against artificial light of turbidity/fluorescence sensor, 2) influence of their abundance on turbidity, and 3) influence of environmental current on their phototactic behavior. Experiment A used natural zooplankton community mainly composed of copepod species collected off Brazil, with changing their packing density. Zooplankton individuals start accumulating around the sensor after the room light turned off, and the turbidity signals increased as individuals stayed in the sampling volume. While the control experiment without zooplankton shows average turbidity of 0.17 FBU, turbidity elevated to 1.02 FBU for packing density of 430 individuals L^{-1}, 2.23 FBU for 870 individuals L^{-1}, and 2.26 FBU for 1300 individuals L^{-1}; a linear increase was found between packing density and turbidity when the packing density was limited below 870 individuals L^{-1}. Experiment B used cultured *Artemia Salina* as a model animal, with packing density of 1850 individuals L^{-1}. They also exhibited accumulations around the sensor under dark condition that led significant increase in turbidity up to 30 FBU. When the environmental current was generated by rotating stirrers, the accumulated individuals were flushed away, and turbidity signal decreased. This experiment simulated the observed negative correlation between current velocity and turbidity in Chapter 2. While turbidity elevation of 2 FBU in Experiment A does not explain nighttime increase in turbidity in Chapter 2 (>50 FBU), the elevation of 30 FBU by *A. Salina* better explains the nighttime increase. This suggests that community structure is important in how effectively zooplankton community affect turbidity signal.

Chapter 5

Sardine-generated turbulence

5.1 Introduction

Mixing due to swimming marine organisms (hereinafter biomixing) is a poorly understood phenomenon. Although major energy sources that drive the global ocean general circulation, such as tides and winds, have been relatively well quantified, contributions from biomixing have been elusive (Ferrari & Wunsch 2009). Nevertheless, some studies (Dewar et al. 2006) have reported that biomixing could possibly be an important component for the global energy budget of ocean general circulation. Dewar et al. (2006) have estimated that 1% of the total chemical power stored in marine organisms, 62.7 TW, could be converted into mechanical energy of the ocean. This is comparable to the power input from winds and tides (Ferrari & Wunsch 2009). In addition, Huntley & Zhou (2004) estimated that schools and swarms of organisms swimming at their moderate speeds can produce strong turbulence equivalent to a rate of kinetic energy dissipation of 10^{-5} W kg^{-1}, regardless of body size (from zooplankton to cetaceans). This value is comparable to the energy dissipation rates measured in well-mixed surface layers (Thorpe 2007). The estimates shown above imply the importance of biomixing in ocean mixing, and consequently, in driving the ocean general circulation.

Besides the theoretical estimates of Dewar et al. (2006) and Huntley & Zhou (2004), observational evidence of biomixing has been reported. Kunze et al. (2006) measured high turbulent kinetic energy dissipation rates of 10^{-5} to 10^{-4} W kg^{-1} in layers with high acoustic backscatter intensity, mainly due to krill, observed by an echo sounder in Saanich Inlet, BC, Canada. Gregg & Horne (2009) also measured elevated turbulent kinetic energy dissipation rates of 10^{-6} to 10^{-5} W kg^{-1} compared to the background value of 10^{-9} W kg^{-1} with high acoustic backscatter intensity in

Monterey Bay, CA, USA, and surmised that the constituents of the high acoustic intensity were anchovy schools, based on the acoustic signals. These measured turbulent kinetic energy dissipation rates are comparable to the theoretical value of 10^{-5} W kg^{-1} estimated by Huntley & Zhou (2004).

However, there are a number of reports which contradict the studies that suggest the importance of biomixing. From additional field observations of biomixing in Saanich Inlet, Rousseau et al. (2010) reported turbulent kinetic energy dissipation rates of 10^{-8} W kg^{-1} with high acoustic backscatter intensity, a dissipation rate higher by a factor of 2 than that in acoustically quiet waters, but 3 orders of magnitude lower than the theoretical 10^{-5} W kg^{-1} estimated by Huntley & Zhou (2004). Sato et al. (2014) reported no correlation between turbulent kinetic energy dissipation rates and volume backscattering strength in Saanich Inlet. On the other hand, Ross & Lueck (2005) developed an inverse method to estimate turbulence intensity (10^{-8} to 10^{-3} W kg^{-1}) from volume backscattering strength in a stratified and highly turbulent water column. Even if marine organisms can induce strong turbulence, it does not always mean strong turbulent 'mixing'. Visser (2007) pointed out that small swimmers, such as krill (~1 cm), cannot produce eddies and subsequent density inversions larger than their body size, implying that biomixing by small swimmers is less efficient than physically induced turbulence. Based on krill body size (1 cm), Visser estimated that, at most, 1% of the total kinetic energy produced by krill swimming is used in mixing, while it is up to 20% for physically induced turbulence (Osborn 1980). Using *in situ* observation data, Gregg & Horne (2009) reported that mixing inside fish schools was 100 times less efficient for vertical mixing of density-stratified water than that due to physically induced turbulence, consistent with Visser (2007). In contrast, based on field campaigns with turbulence measurements, net samplings, still image recordings and acoustic surveys, Lorke & Probst (2010) found that, regardless of whether turbulence was measured inside or outside of fish schools, roughly 20% of the turbulent kinetic energy was used for vertical mixing of density. Katija & Dabiri (2009) pointed out that fluid viscosity and body shapes, rather than generated eddy size, are important in determining the efficiency of swimming-induced mixing, as the viscous fluids can be drifted along the swimming organisms, and that more efficient swimmers are more efficient in drifting fluid around their bodies: the length of drifted water along the streamline, not the body length, is the important scale. The studies discussed above, with conflicting conclusions regarding the efficiency of biomixing, clearly demonstrate the need for further studies.

One of the most problematic issues in the previous studies is that one cannot be sure whether the measured turbulence was caused by the swimming organisms, and that it is not possible to know the detailed swimming behaviors of the organisms when they encountered the instruments just by using echo sounders, which were frequently utilized in the studies. Characteristics such as swimming behavior, swimming speed and synchrony of group motion can be influenced by the presence of instruments (e.g. avoidance of an approaching turbulence microstructure profiler). Although these characteristics appear to be critical for determining the intensity of the induced turbulence (Huntley & Zhou 2004), the previous observations did not consider swimming behavior but used acoustic backscatter merely to estimate population density. However, in a tank experiment, Catton et al. (2011) reported that individual (not aggregated) krill were able to transfer a water parcel by a distance of 1 body length, while aggregated krill actively transferred water parcels down to successive group members and disturbed the water column at a scale of aggregations. They suggested that different biological characteristics (i.e. individual or aggregation, distance between group members) result in different fluid motions around the swimming organism. Thus, obtaining turbulence measurements simultaneously with visual observations of organism aggregations and their swimming behavior is necessary to investigate the intensity of turbulence generated by an organism and to elucidate whether the generated turbulent eddy is large enough to produce mixing in the ocean.

In this study, we conducted an experiment in a large aquarium tank containing several thousand Japanese sardines *Sardinops melanostictus* to measure turbulence inside the sardine school and to observe the school characteristics simultaneously. *S. melanostictus* and the other species in the genus *Sardinops*, which have similar body dimensions and behavioral characteristics, are a cosmopolitan taxon and have a large biomass in the ocean (Whitehead 1985), and hence, the result from this experiment is expected to be applicable for the world ocean. The objectives of this study were to measure biologically induced turbulence and to investigate the relationship between turbulent properties and school characteristics.

5.2 Materials and methods

5.2.1 Microstructure profiler

A microstructure profiler, the Turbulence Ocean Microstructure Acquisition Profiler-9 (Fig. 5.1A; hereinafter TM9; JFE Advantech), was used to measure turbulence

inside the sardine school. The 1.3 m long free-ascending TM9 sampled data from the bottom of the experiment tank until it reached the surface without any interruptions (Figs. 5.1B & 5.2). Nominal ascending speed was roughly 0.5 m s^{-1}. In a past study, the TM9 was deployed in a small bay as shallow as 20 m depth (Saita et al. 2009). The TM9 had 2 turbulent shear probes (hereinafter shear-1 and shear-2; digitized at 512 Hz), an FP07 fast temperature probe (512 Hz), a light-emitting diode fluorescence/turbidity probe (256 Hz), a CTD (64 Hz) and XYZ 3-directional accelerometers (256 Hz) on the head. Previous studies (Kunze et al. 2006, Gregg & Horne 2009, Rousseau et al. 2010) used free-fall microstructure profilers, which may not be suited to measure turbulence near the water surface due to unstable motion of the profiler's body. In order to maximize the sampling water column, we employed a free-ascending profiler.

For deployment, a weighted releaser was attached to the tail of the TM9. After the TM9 had sunk to the bottom, we waited 3 min before releasing the attached weight in order to avoid contamination from disturbances generated by the instrument setup. Eight deployments were performed during the course of the experiment (Table 5.1).

5.2.2 Experimental tank and sardines

We used a large indoor tank (Fig. 5.1B) at an aquarium (Yokohama Hakkeijima Sea Paradise, www.seaparadise.co.jp/english/). Since the tank is managed as part of a commercial aquarium, we had a limited time window and were allowed to deploy the instrument only 8 times. The 7 m deep tank held 1500 m^3 of seawater and contained roughly 5000 Japanese sardines *Sardinops melanostictus*, caught in the sea around Japan. Body length of the sardines, L, was measured as total length after the experiment, and averaged 0.173 m (n = 35; Table 5.2), typical of adult Japanese sardines (Whitehead 1985). The tank also contained predators of sardines, such as sand tiger sharks, rays and mackerels. Due to their presence, the sardines regularly formed an aggregation, or school, during the measurements. Since predator abundance was relatively low compared to that of the sardines (e.g. a few sand tiger sharks and rays, and several tens of mackerels) and no predators were identified near the measuring sensors, turbulence generation due to the predators was ignored.

Water temperature and salinity in the tank were 20.0 ± 0.016°C (mean ± SD) and 30.6 ± 0.001 respectively. Mean and SD were calculated from all deployments of the TM9. The water column was almost homogeneous, with very weak stratification dominated by temperature. The spatial- and temporal-averaged stratification

corresponded to a buoyancy frequency of $N = 1.6 \times 10^{-3}\ \mathrm{s}^{-1}$, comparable to that in the surface mixed layer of the ocean (Thorpe 2007). Aeration devices that created bubble columns and circulation to stir the water were turned off 1 h before commencing the experiment to minimize turbulence generated from the circulation system.

In order to visually inspect the performance of the TM9, 3 video cameras were placed around the tank (Figs. 5.1B & 5.2): Camera #1 in front of the panorama window, Camera #2 in front of an acrylic glass window located 6 m above the bottom, and Camera #3 in an underwater tube. Cameras #1 and 2 were mounted on tripods and Camera #3 was hand-held. Footage was recorded simultaneously by all 3 video cameras.

Based on the film footage, we distinguished 3 different types of swimming behavior of the sardine school: avoidance, feeding, and cruising behaviors. Given that the turbulence sensors (i.e. the shear probes) require a background flow to measure turbulence, and thus the TM9 needed to ascend in the tank, it was not possible to suppress the sardines' avoidance behavior in response to the TM9, which was measuring turbulence inside the school. All of the turbulence measurements inside the school were made when the sardines showed avoidance behavior. However, when aquarium personnel fed food pellets (2 mm in diameter) to the sardines before the launch of Deployment 3, and the sardines were feeding on the pellets, they exhibited a different swimming pattern (feeding behavior) from avoidance behavior shown in the other deployments. Avoidance behavior was short-burst swimming; on the other hand, feeding behavior was comparatively fast and long-lasting swimming. The school displayed cruising behavior when neither avoidance nor feeding behavior was exhibited. Thus, no turbulence measurement from cruising behavior was obtained.

For each behavior, we were able to measure swimming speeds relative to L from the footage. Relative speeds were used to estimate absolute swimming speeds, assuming $L = 0.173$ m. Swimming behavior is described in '5.3.1 School behavior' and discussed in '5.4.1 Swimming behavior'.

For packing density of the sardines in the school, we tried to estimate this using video footage obtained from the 3 video cameras. However, packing density was hard to quantify from the footage since the arrangement of the video cameras was not suited to establish the 3-dimensional position of each sardine. Therefore, we estimated packing density by making use of the measured body length of the sardines and assuming that the distribution of the sardines in the school displayed

hexagonal close-packing of equal spheres, as discussed in '5.4.3 Dissipation rates'.

5.2.3 Turbulent kinetic energy dissipation rate

Assuming isotropy of turbulence, the rate of turbulent kinetic energy dissipation, ε is estimated as

$$\varepsilon = \frac{15}{2} \cdot \nu \cdot \overline{\left(\frac{\partial u}{\partial z}\right)^2} = \frac{15}{2} \cdot \nu \cdot \int_{k_1}^{k_2} \phi(k)\, \mathrm{d}k, \tag{5.1}$$

where ν is the kinematic viscosity, the overbar indicates the temporal average, $\partial u / \partial z$ is the velocity vertical shear, k is the wavenumber, ϕ is the shear spectrum as a function of k, and k_1 and k_2 are the integration range. In this study, $k_1 = 1$ cycles per meter (cpm) and $k_2 = k_\eta / 2$, where k_η is the Kolmogorov wavenumber, $k_\eta = (\varepsilon \cdot \nu^{-3})^{1/4}$. When k_2 was larger than the Nyquist wavenumber (~500 cpm in this study), ϕ was extrapolated to k_2 by using the Nasmyth empirical spectrum (Oakey 1982), which is an empirical spectrum for a well-developed turbulence field. Wavenumber ranges, excluding high-frequency noises from the system electronics, were extrapolated by the Nasmyth spectrum for the integration in Eq. (5.1). The logarithmic spectral power loss along increasing wavenumbers, which depends on the size of the sensing tips of the turbulent shear probes (~1 cm), was corrected using a single pole filter (Oakey 1982). The rate of kinetic energy dissipation was estimated from a 2 s section of data which was half-overlapped with the next sections. From the video footage, we were able to visually distinguish whether or not the estimated ε values were acquired inside the sardine school by measuring the distance between the school and the turbulent shear probes.

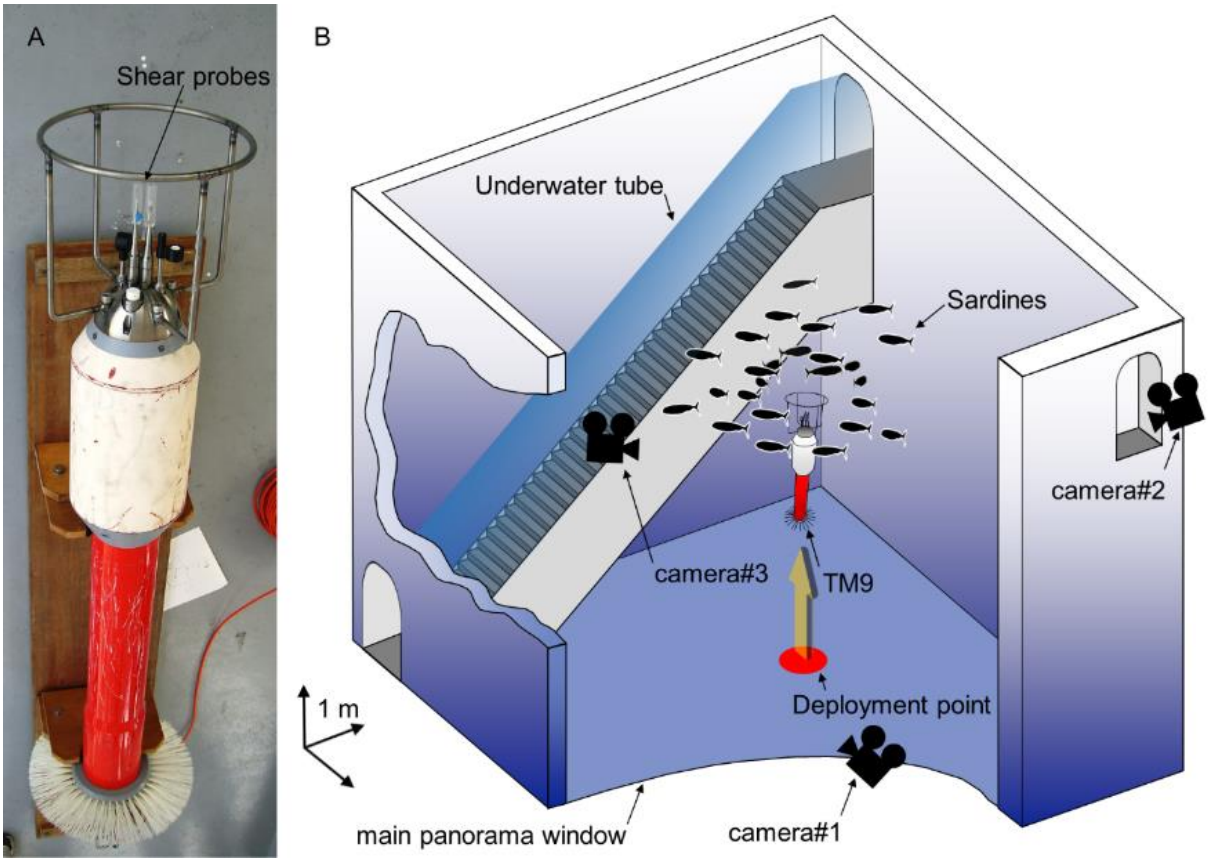

Fig. 5.1. (A) Microstructure profiler, Turbulence Ocean Microstructure Acquisition Profiler-9 (TM9). (B) Experimental setup. Approximate scale shown at lower left.

Table 5.1. Deployments of the TM9 microstructure profiler. Presence: whether or not deployment was successful in measuring inside the sardine school. Period: amount of time taken for the TM9 to measure inside the sardine school (highlighted in light gray in Fig. 5.3). Depth: vertical distance measured by the TM9 inside the sardine school. Thickness: sardine school thickness along vertical coordinate. ($\bar{\varepsilon}$): energy dissipation rate averaged over the period. Background $\bar{\varepsilon}$: energy dissipation rate averaged over the calculation sections outside the sardine school.

		sardine school						
deployment name	launch time	presence	period (s)	depth (m)	thickness (m)	behavior	$\bar{\varepsilon}$ (W kg^{-1})	Background $\bar{\varepsilon}$ (W kg^{-1} x 10^{-6})
Deploy 1	19:33	Yes	3–9	0.5–3.6	3.1	Avoidance	3.2 x 10^{-4}	6.2
Deploy 2	19:54	Yes	0–2	3.0–3.9	0.9	Avoidance	8.6 x 10^{-5}	5.9
Deploy 3	19:59	Yes	6–8	0.5–1.6	1.1	Feeding	2.2 x 10^{-4}	3.1
Deploy 4	20:02	Yes	4–7	0.5–2.1	1.6	Avoidance	8.7 x 10^{-5}	5.1
Deploy 5	*19:45	No	—	—	—	—	—	9.7
Deploy 6	20:07	No	—	—	—	—	—	8.1
Deploy 7	20:10	No	—	—	—	—	—	4.9
Deploy 8	20:21	No	—	—	—	—	—	4.1

Table 5.2. Body dimensions and wet weight of sardines kept in the tank during measurements.

measured items	mean (m)	S. D. (m)
Length	0.173	0.015
Width	0.018	0.002
Height	0.029	0.002
Wet weight	0.033 (kg)	0.008 (kg)

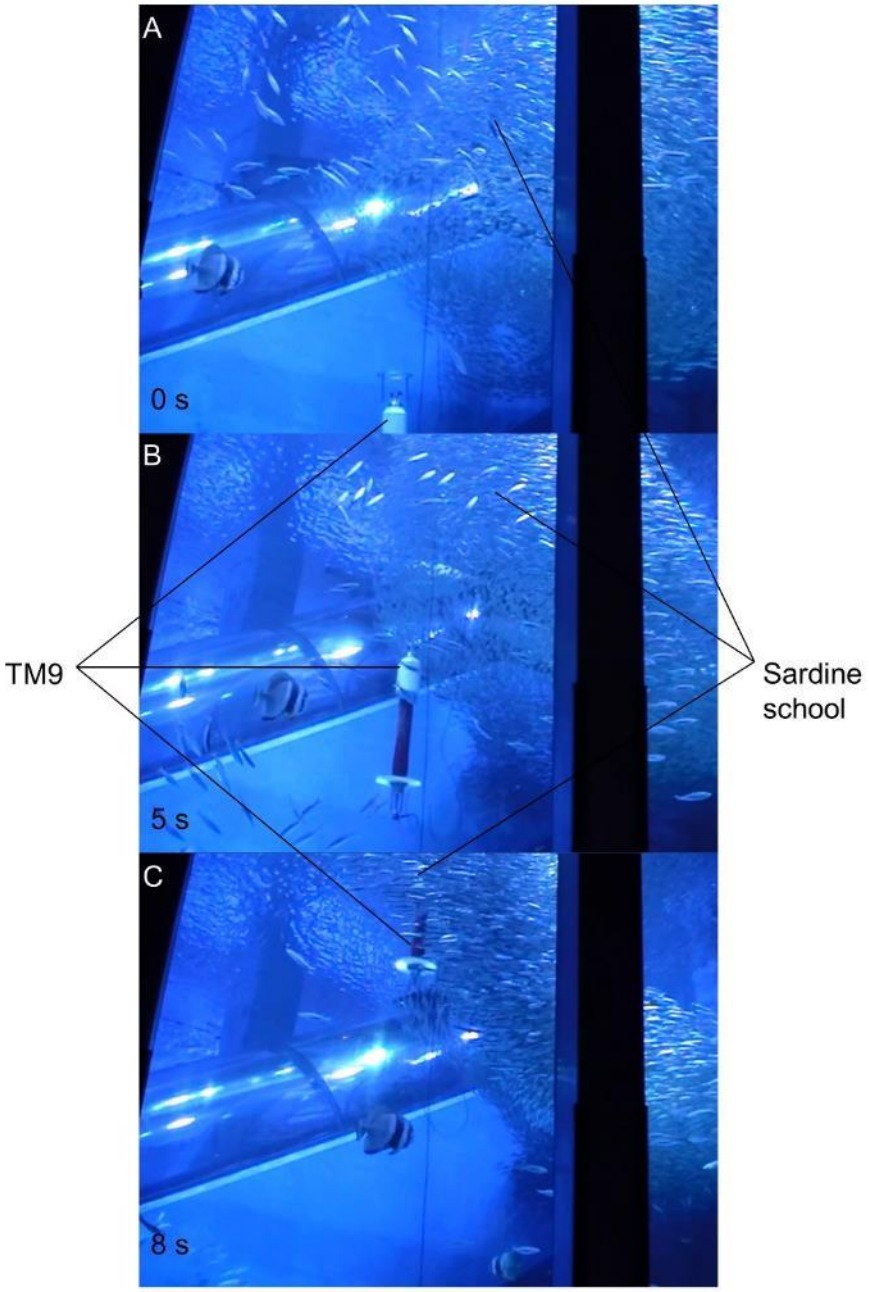

Fig. 5.2. Still images from video footage taken during Deployment 1 by Camera #1. (A) Sardines forming a school above the TM9 microstructure profiler prior to release. (B) TM9 ascending toward sardine school. (C) TM9 measuring turbulence inside the sardine school. Approximate times elapsed from release of TM9 shown in bottom left of each image.

5.3 Results

5.3.1 School behavior

Deployments 1 to 4 passed inside the sardine school. Except for Deployment 3, the sardine school avoided the oncoming TM9 by dispersing in different directions. For each deployment, the distance between the school and the TM9 was about 1 m. The swimming speed of this avoidance behavior was $v_{\text{avoidance}} = 1.08 \pm 0.11\ \text{m s}^{-1}$ (mean ± SD, n = 7), estimated from Deployment 2 footage. Predator avoidance (i.e. ray) was observed as well. Swimming speed during avoidance behavior (away from the predator) was $1.32 \pm 0.18\ \text{m s}^{-1}$, estimated from footage taken before Deployment 1, and the estimated distance between the rear of the school and the predator was about 1 m. On the other hand, when sardines were fed 20 s before the launch of Deployment 3, the school swam relatively quickly ($v_{\text{feeding}} = 0.72 \pm 0.09\ \text{m s}^{-1}$; n = 7) in the same direction. When the TM9 was ascending into the school, sardines avoided the instrument, keeping a distance of ~1 m from it without changing their swimming speed; this response was not as prominent as in avoidance behavior, and was categorized as feeding behavior. During feeding behavior, sardines appeared to be more focused on the food than on the approaching TM9. Except when expressing avoidance or feeding behavior, the sardine school swam at a relatively slow speed, categorized as cruising behavior, at a rate of $v_{\text{cruising}} = 0.26 \pm 0.04\ \text{m s}^{-1}$ (n = 10), estimated from footage taken before Deployment 1. For any behavior, the sardines kept synchrony with regard to their swimming speed, duration, and timing when they changed from one behavior to another. Deployments 5 to 8 passed outside of the sardine school.

Predators did not affect school behavior during any deployments, and the spatial distance between the predators and the TM9 was significantly large for each deployment. No physical contact between the sardines and the turbulent shear probes was observed. Thus all turbulence signals inside the school recorded by the TM9 were due to sardine swimming.

5.3.2 Turbulence inside and outside sardine school

Based on TM9 data obtained outside the sardine school (Deployments 5 to 8), the range of background energy dissipation rates was $\varepsilon = 10^{-6}$ to $10^{-5}\ \text{W kg}^{-1}$ (Fig. 5.3E–H). The average was $\varepsilon = 6.7 \times 10^{-6}\ \text{W kg}^{-1}$. Maximum ε was roughly 10^{-5} W kg^{-1} and minimum ε was 1.1×10^{-6} W kg^{-1}. This background turbulence level is similar to that found in the surface mixed layer of the ocean (Thorpe 2007).

Inside the sardine school, ε values exceeded 10^{-4} W kg^{-1} (Fig. 5.3A–D, Table

5.1). The average was 2.3 × 10^{-4} W kg^{-1}, roughly 50 times greater than the background value. There was no significant difference in the magnitude of ε between the avoidance and feeding behaviors (Table 5.1).

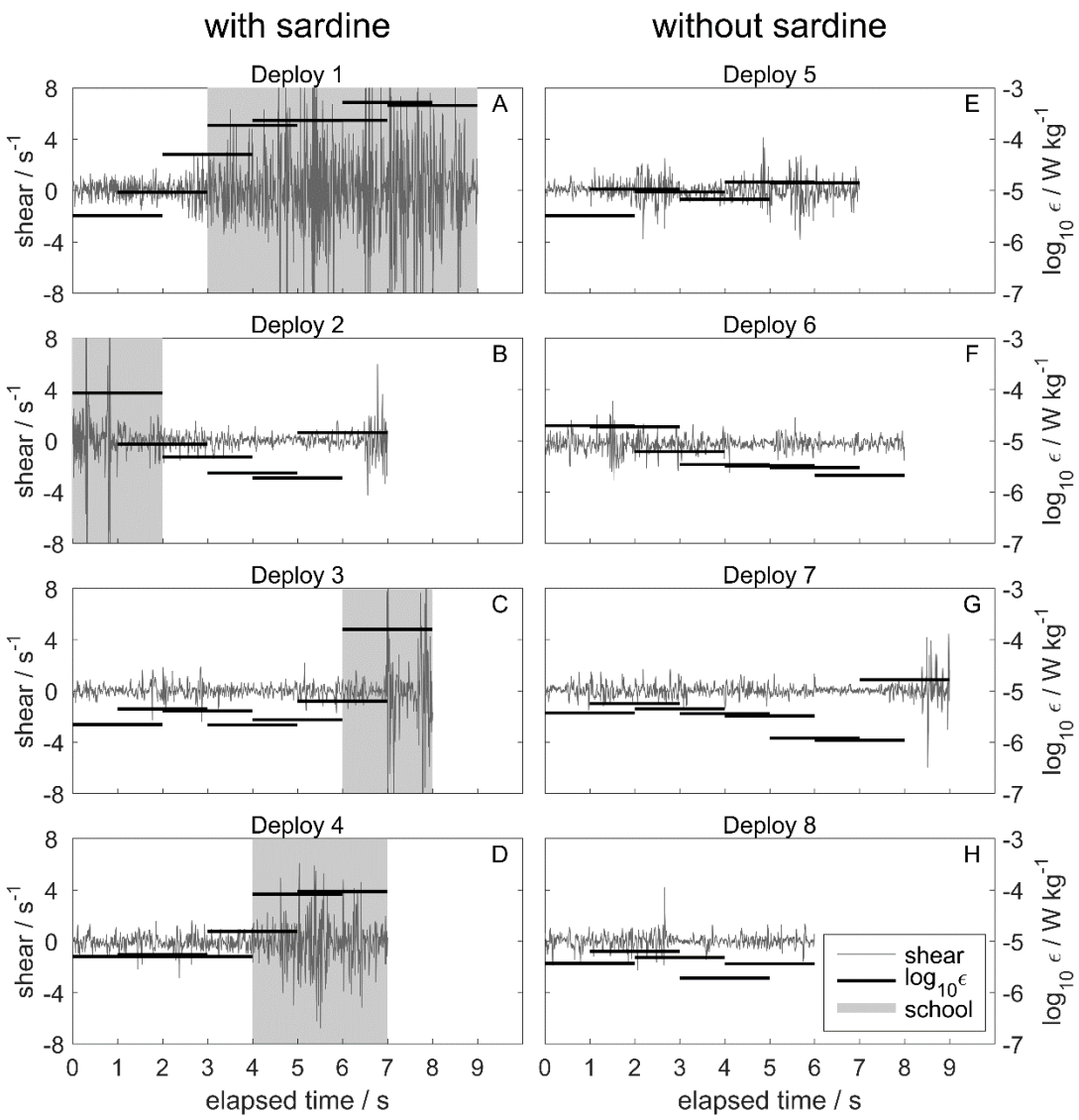

Fig. 5.3. Time series of turbulent velocity shear (thin gray lines) and kinetic energy dissipation rates ε (thick black bars) for 8 deployments (deploy) of the TM9 micro structure profiler. Widths of black bars (2 s) indicate sections used to estimate ε. Data from (A–D) inside and (E–H) outside the sardine (*Sardinops melanostictus*) school. Light gray sections in (A–D) show when the TM9 acquired data from inside the school.

5.3.3 Spectrum analysis

In order to consider the properties of turbulence induced by the sardine school, we examined the wavenumber spectra of turbulent velocity shear. Because mean L was 0.173 m, the wavenumber $k = L^{-1} = 5.8\,\mathrm{cpm}$ is considered to be representative for that size.

Shear spectra measured outside the sardine school followed the Nasmyth spectrum, as in physically induced turbulence in the ocean (Fig. 5.4). The Nasmyth spectrum was within or close to the upper and lower 95% confidence intervals of the measured shear spectra.

Shear spectra obtained from the data inside the school during avoidance behavior did not follow the Nasmyth spectrum well (Fig. 5.5). For example, in the case of Deployment 1, the spectrum had a slope of k^1 in 1–20 cpm, while the Nasmyth spectrum has a slope of $k^{1/3}$ in the inertial sub-range (Fig. 5.5A). Spectral power at 20–40 cpm was higher than that of the Nasmyth spectrum, while spectral power in the wave number ranges lower than $L^{-1} = 5.8\,\mathrm{cpm}$ was significantly lower than the Nasmyth spectrum (Fig. 5.5A). Spectra computed from Deployment 2 and Deployment 4 data, inside the sardine school, had power declines in the inertial sub-range similar to Deployment 1 (Fig. 5.5B,C). For these spectra, the spectral power at 1 cpm was about one-third that of the Nasmyth spectrum regardless of the magnitude of ε, which is clearly shown by the variance-preserving forms of the velocity spectra corresponding to each shear spectrum (Fig. 5.5D–F).

On the other hand, shear spectra measured inside the sardine school while the sardines were fed show relatively good agreement with the Nasmyth spectrum in the wavenumber ranges lower than L^{-1} (Fig. 5.6). The shear spectra computed using shear-1 and shear-2 had power levels comparable to that of the Nasmyth spectrum in the wavenumber ranges lower than L^{-1} (Fig. 5.6A,B). However, the spectral shapes are somewhat distorted from the Nasmyth spectrum, with convex down and up at the transition between inertial sub-range and viscous sub-range, probably reflecting the high spatial and temporal variabilities in turbulence generated by the sardine school.

All non-dimensionalized spectra and their averaged spectra are shown separately for the turbulence induced by avoidance behavior (Fig. 5.7A,C) and that induced by feeding behavior (Fig. 5.7B,D). Turbulence induced by avoidance behavior had a power decline in the inertial sub-range on average, while that induced by feeding behavior showed no power decline.

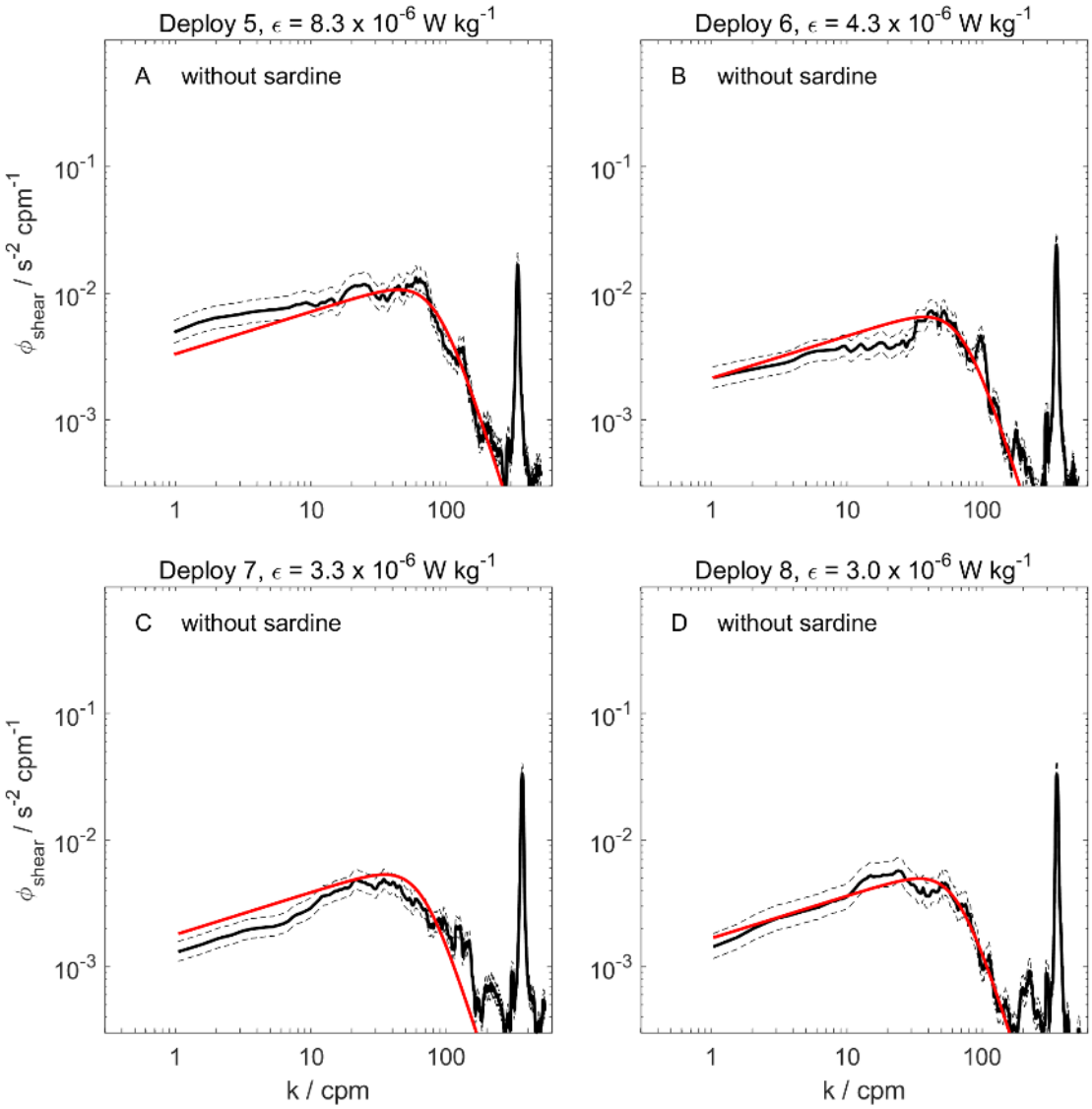

Fig. 5.4. Spectra (ϕ) of turbulent velocity shear outside the sardine school for (A–D) Deployments 5 to 8, respectively, as functions of wavenumber k (cycles per meter, cpm). Measured spectra denoted by thick black lines, upper and lower 95% CIs by thin dashed lines, and Nasmyth spectrum by thick red lines. Each Nasmyth spectrum corresponds to the turbulent kinetic energy dissipation rates (ε, W kg^{-1}) above the panels. Peaks at around $k = 300$ cpm caused by instrument's electrical noise.

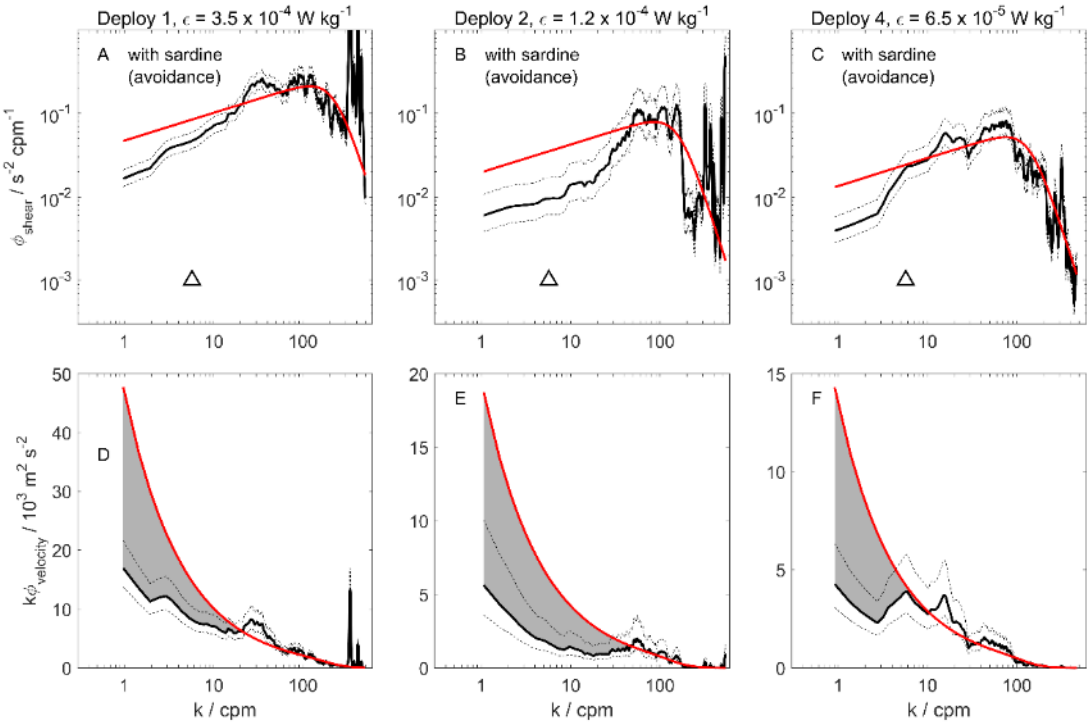

Fig. 5.5. (A–C) Spectra (φ) of turbulent velocity shear inside the sardine school displaying avoidance behavior for Deployments (A) 1, (B) 2, and (C) 4. Line descriptions same as in Fig. 5.4. Inverse of the average body length $L^{-1} = 5.8$ cpm ($L = 0.173$ m) shown as a triangle. (D–F) Variance-preserving forms of velocity spectra corresponding to (A–C). Areas where velocity spectra are lower than Nasmyth spectrum highlighted in light gray. See Fig. 5.4 for further details.

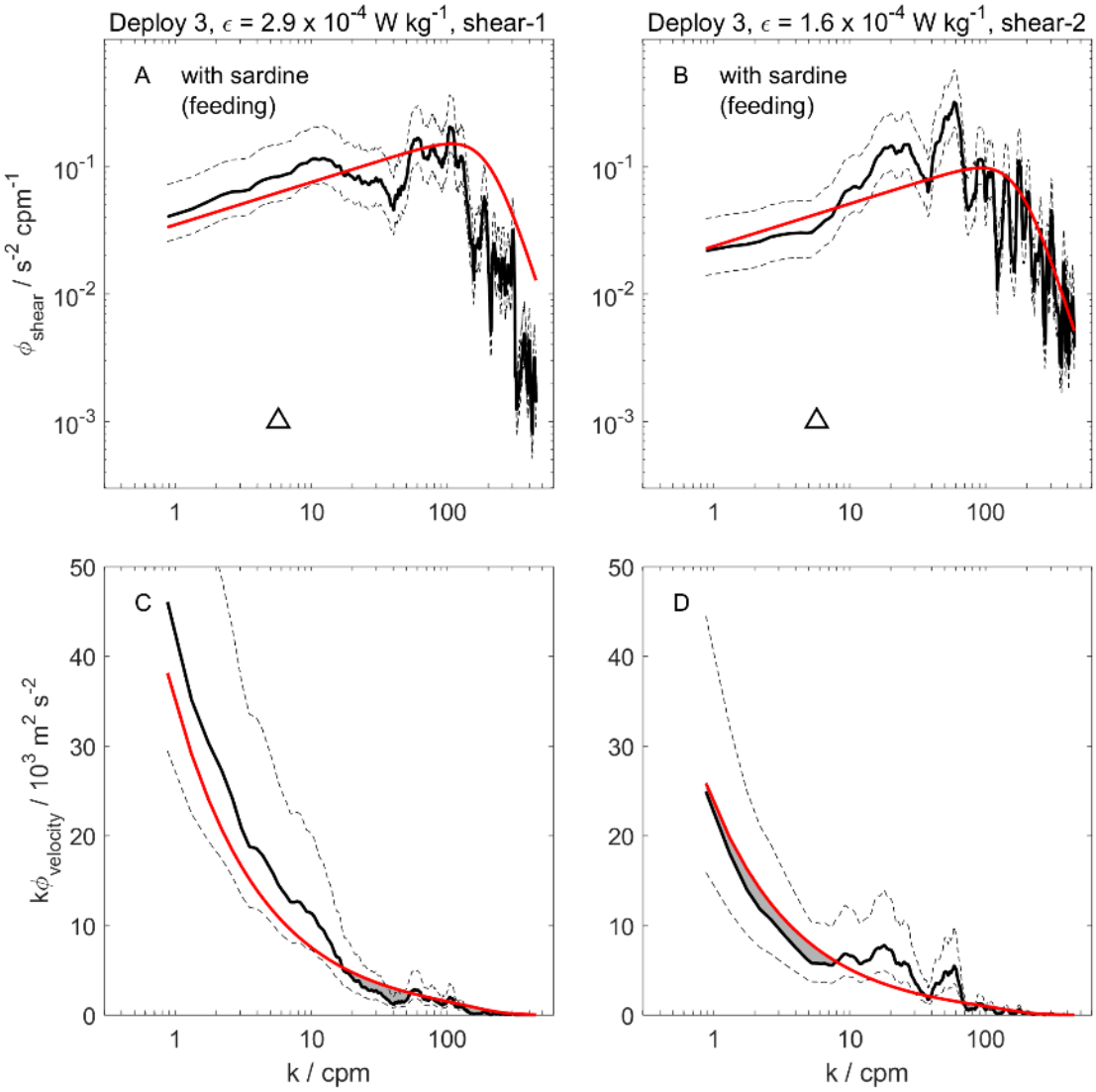

Fig. 5.6. Same as Fig. 5.5, but with spectra acquired inside the sardine school during feeding behavior in Deployment 3. (A,C) Shear-1 and (B,D) shear-2 probes. See Figs. 5.4 & 5.5 for further details.

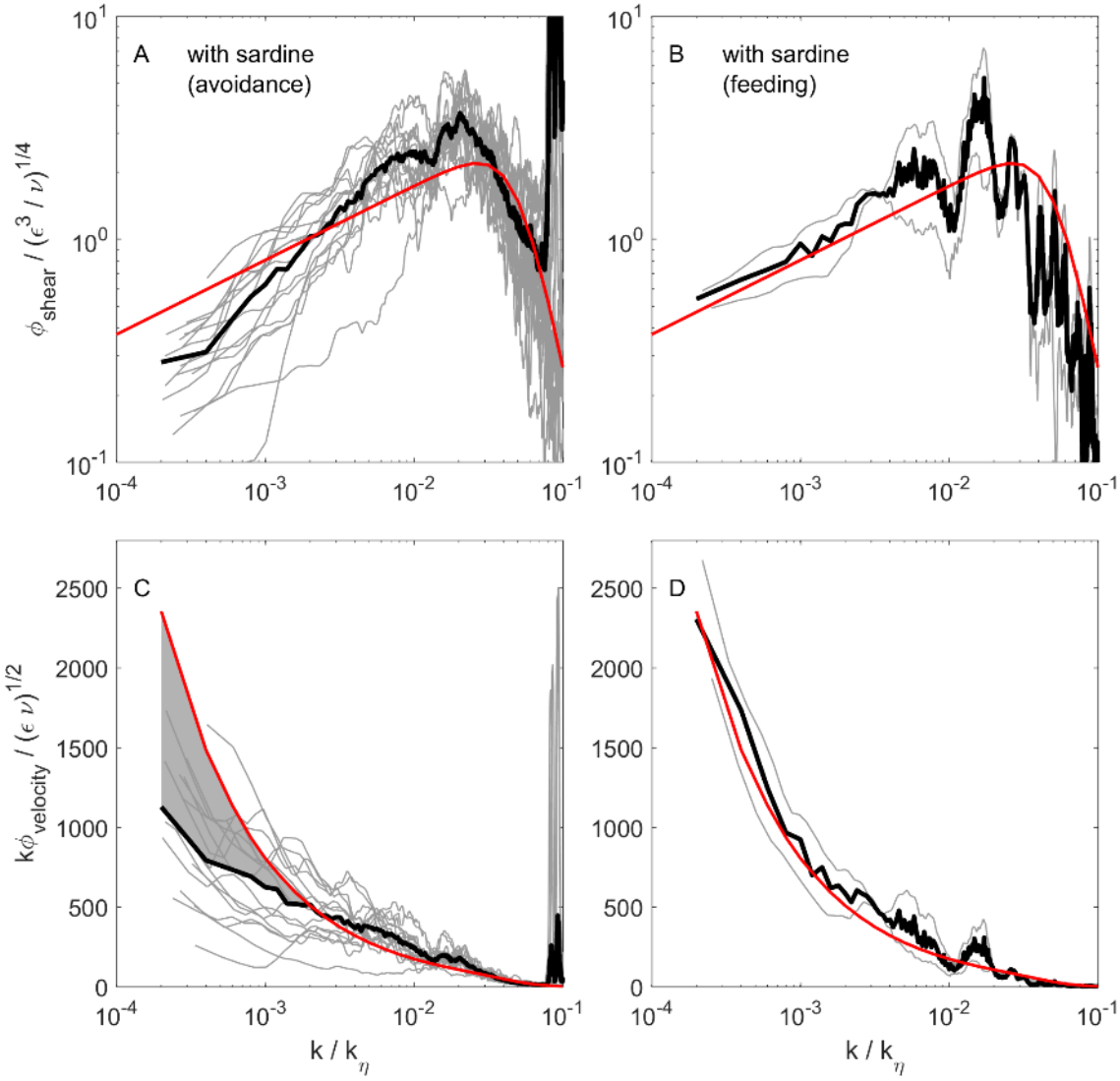

Fig. 5.7. (A,B) Non-dimensionalized turbulent shear spectra (ϕ) using $(\varepsilon^3 / \nu)^{1/4}$ as a function of non-dimensionalized wavenumber by Kolomogorov wavenumber (k_η). ε: turbulent kinetic energy dissipation rate, ν: kinematic viscosity. Raw spectra denoted by thin gray lines, averaged spectrum by thick black lines, and Nasmyth spectrum by red lines. (C,D) Variance-preserving forms of velocity spectra which are non-dimensionalized using $(\varepsilon\,\nu)^{1/2}$ as a function of non-dimensionalized wavenumber by Kolomogorov wavenumber. Area where averaged velocity spectrum is lower than the Nasmyth spectrum highlighted in light gray. (A,C) Data for sardine avoidance behavior include 16 spectra, and (B,D) data for feeding behavior include 2 spectra.

5.4 Discussion

5.4.1 Swimming behavior

Turbulence was measured inside the sardine school displaying either avoidance or feeding behavior, but turbulence during cruising behavior was not measurable. Few studies have reported *in situ* swimming speed of sardines: 0.21 to 0.77 m s^{-1} from Hara (1987) and 0.67 to 1.59 m s^{-1} from Misund et al. (2003). Swimming speeds observed in the present study during 3 types of behavior were $v_{\text{avoidance}} = 1.08 \pm 0.11\,\text{m s}^{-1}$, $v_{\text{feeding}} = 0.72 \pm 0.09\,\text{m s}^{-1}$, and $v_{\text{cruising}} = 0.26 \pm 0.04\,\text{m s}^{-1}$. All are within the range of the *in situ* observed swimming speeds shown in Hara (1987) and Misund et al. (2003). In the present study, the avoidance behavior shown against the TM9 and predator(s) was similar with regard to swimming speed and distance between the school and the instrument or predator. While there has been no quantitative study on sardines avoidance behavior against predators in the ocean, we speculate that the level of turbulence induced by sardines in the ocean is the same as that in this study.

During feeding, Japanese sardines exhibit 3 types of behavior in the ocean: filter-feeding, particulate-feeding, and intermediate mode (Garrido & van der Lingen 2014). Filter-feeding is characterized by fish holding their mouths open while swimming without visual detection and selection, and particulate-feeding is characterized by visual detection and selection of individual prey (Garrido & van der Lingen 2014). Sardine particulate-feed when prey size is larger than 1.23 mm (van der Lingen 1994). Since 2 mm diameter food pellets were fed to the sardines prior to the launching of Deployment 3, we suspect that they employed particulate-feeding behavior, given that it was not clear from the film footage which feeding behavior was employed. Garrido & van der Lingen (2014) note that Japanese sardines appear to frequently filter-feed in the ocean, swimming slower than during particulate-feeding but faster than cruising speeds (Garrido et al. 2007).

During cruising, it was not possible to directly measure turbulence induced by this behavior. Since slower swimming speed may result in lower turbulent kinetic energy production (Huntley & Zhou 2004; see '5.4.3 Dissipation rates'), the level of turbulence induced by cruising behavior is expected to be lower than the measured turbulence intensity, 2.3×10^{-4} W kg^{-1} on average. On the other hand, no difference in ε between avoidance and feeding behaviors was observed (Table 5.1).

5.4.2 Background turbulence

Although the background turbulence of 10^{-6} W kg^{-1} measured in the tank is possible

in the ocean, it occurs under limited situations, such as inside the surface mixed layer forced by winds (Oakey & Elliott 1982) and surface cooling (Shay & Gregg 1986) or in shallow regions under strong tidal forcing (Kokubu et al. 2013) or island wakes in strong ocean current regions (Hasegawa et al. 2004). In the interior of the open ocean, away from the boundaries, values of ε vary from 10^{-10} to 10^{-7} W kg^{-1} and are generally in the order of 10^{-9} to 10^{-8} W kg^{-1} (Thorpe 2005). Since turbulent kinetic energy, which is newly input by a forcing source (e.g. internal wave breaking, shear instability) into the water column, is integrated on (added to) background turbulent kinetic energy (Nikora 1999), ε of 10^{-4} W kg^{-1} acquired inside the sardine school may not be the net intensity of turbulence induced solely by the sardine school. However, since ε inside the sardine school was 2 orders of magnitude higher than the background, bias due to background turbulence was negligible (~1%) in this study.

5.4.3 Dissipation rates

The observed ε caused by the sardine school was 2.3×10^{-4} W kg^{-1} on average, which is among the largest values of past field studies (Hasegawa et al. 2004). Kunze et al. (2006) reported $\varepsilon = 10^{-5}$ to 10^{-4} W kg^{-1} in krill aggregations in Saanich Inlet, Canada. On the other hand, Rousseau et al. (2010) noted $\varepsilon = 1.4 \times 10^{-8}$ W kg^{-1} with high acoustic backscatter intensity that was likely krill aggregations, in Saanich Inlet. Gregg & Horne (2009) related $\varepsilon = 10^{-6}$ to 10^{-5} W kg^{-1}, with high acoustic backscatter intensity that was likely anchovy schools in Monterey Bay, USA. Lorke & Probst (2010) reported $\varepsilon = 3 \times 10^{-9}$ to 1×10^{-8} W kg^{-1} based on fast response temperature sensor data in freshwater fish schools in Lake Constance, Germany. All the above studies used microstructure profilers similar to this study for measuring turbulence. Because the sardine school in this study displayed avoidance behavior against the microstructure profiler, it is possible that the results from the other studies might be due to avoidance behavior as well.

According to Huntley & Zhou (2004), swimming organisms produce turbulence corresponding to $\varepsilon = 10^{-5}$ W kg^{-1} regardless of body size (from zooplankton to whales) using the equation:

$$\varepsilon_p = \frac{e_d}{\eta} \cdot \frac{1}{\rho} \cdot \frac{n}{V}, \tag{5.2}$$

where ε_p (W kg^{-1}) is the total rate of energy production by a group of animals, e_d is

the rate of energy expenditure to overcome drag by an individual animal, η is propulsive efficiency, ρ is density of seawater, and n / V is the number of animals per unit volume of seawater. The ε_p is equivalent to ε for swimming organisms, and e_d and η are functions of swimming speeds. While Huntley & Zhou (2004) obtained $\varepsilon_p = 10^{-5}\ \mathrm{W\ kg^{-1}}$ based on only cruising speeds, we recalculated e_d and η using the observed swimming speeds during avoidance behavior, $v_{\mathrm{avoidance}} = 1.08 \pm 0.11\ \mathrm{m\ s^{-1}}$ (mean ± SD), and feeding behavior, $v_{\mathrm{feeding}} = 0.72 \pm 0.09\ \mathrm{m\ s^{-1}}$.

e_d is shown as:

$$e_d = Dv, \tag{5.3}$$

where D is the drag force and v is swimming speed. D is given as:

$$D = \frac{1}{2}\rho v^2 S_W C_D, \tag{5.4}$$

where ρ is the density of seawater calculated from the international equation of state of seawater (UNESCO 1981), S_W is the total wetted surface area, and C_D is the drag coefficient. S_W is approximated as $S_W = 2WL$, where W is the average body width and L is the average body length. C_D is approximated as $C_D = 0.072\ \mathrm{Re}^{-0.2}$ (Hoerner 1965). η is defined as a ratio of e_d divided by the total rate of energy utilized by a single animal and approximated as (Weihs 1977, Wardle et al. 1996):

$$\eta = 0.39\ v^{0.24}. \tag{5.5}$$

The measured swimming speeds were $v_{\mathrm{avoidance}} = 1.08 \pm 0.11\ \mathrm{m\ s^{-1}}$ (mean ± standard deviation) for the avoidance behavior and $v_{\mathrm{feeding}} = 0.72 \pm 0.09\ \mathrm{m\ s^{-1}}$ for the feeding behavior. Assuming that the possible ranges of the swimming speeds are within one standard deviation, we obtain $e_d = (1.9 \text{ to } 3.3) \times 10^{-2}\ \mathrm{W}$ and $\eta = 0.39 \text{ to } 0.41$ for the avoidance behavior, and $e_d = (5.6 \text{ to } 11.3) \times 10^{-3}\ \mathrm{W}$ and $\eta = 0.35 \text{ to } 0.37$ for the feeding behavior.

Since we could not measure n / V from the video footage, we estimated it based on the following assumptions: (1) the distribution of individual sardines in the school displayed hexagonal close-packing (hcp) of equal spheres, and (2) the radius of the spheres was equal to the average body length $L = 0.173\ m$. The second assumption assumes that each sardine kept a distance of at least 1 body length from

its neighbors. Hcp is a concept that is common in crystallography and has been used for estimating animal distributions in the water (e.g. Mackie & Mills 1983). The volume of a cell V_C is expressed as:

$$V_C = 8\sqrt{2}r^3, \tag{5.6}$$

where r is the radius of the spheres. The number of spheres in a cell is two, $n_{spheres} = 2$. The density of spheres $n / V_{spheres}$ is shown as:

$$n / V_{spheres} = \frac{n_{spheres}}{V_C}. \tag{5.7}$$

We take $r \sim L = 0.173$ m; thus, we obtain $n / V_{spheres} = 34.1$ spheres m^{-3}. Assuming that each sphere corresponds to an individual sardine, we obtain $n / V = 34.1$ individuals m^{-3}, which seemed reasonable after comparing it with the footage. Seawater density $1 / \rho$ in Eq. (5.2) is canceled since e_d is a linear function of ρ. Assuming possible ranges of the swimming speeds within 1 SD, the total rates of energy production are $\varepsilon_{\mathrm{p\ avoidance}} = (1.6 \text{ to } 2.7) \times 10^{-3}\ \mathrm{W\,kg^{-1}}$ for avoidance behavior and $\varepsilon_{\mathrm{p\ feeding}} = (5.3 \text{ to } 10.2) \times 10^{-4}\ \mathrm{W\,kg^{-1}}$ feeding behavior. Thus, the estimated values from Huntley & Zhou (2004) are an order of magnitude higher than the measured $\varepsilon = (0.8 \text{ to } 5.2) \times 10^{-4}\ \mathrm{W\,kg^{-1}}$ in our experiment. Lorke & Probst (2010) also reported that the estimated values of Huntley & Zhou (2004) were higher than their measured turbulent kinetic energy dissipation rates.

5.4.4 Spectrum shapes

The spectra for avoidance and feeding behaviors showed deviations from the Nasmyth spectrum through all wavenumber ranges (Figs. 5.5 & 5.6). This suggests that sardines successively generated turbulent eddies and continuously modified the turbulence field, unlike physically induced eddies. Since energy containing scales in the ocean (e.g. thickness of surface mixed layer, internal wave height) are typically larger than the size of a microstructure profiler, the profilers can only measure eddy cascades and viscous dissipation processes in the ocean. On the other hand, the largest possible energy-containing eddies were formed at the scale similar to the sardine school size or the individual size ($L = 0.173$ m) in this experiment. Although the spectra of the background turbulence followed the Nasmyth spectrum (Fig. 5.4), the spectra from the avoidance behavior showed power declines at wavenumber

ranges lower than $L^{-1} = 5.8$ cpm (Fig. 5.5). This suggests that the energy-containing scale was the same as or smaller than $L = 0.173$ m (Fig. 5.8A), since the kinetic energy of 3-D turbulent eddies cascades into smaller eddies (higher wavenumbers) (Nikora 1999). The power declines formed roughly k^{+1} slopes in the inertial sub-range, consistent with Gregg & Horne (2009), and was similar to that found in the turbulence field inside the bottom boundary layer where turbulent eddies are successively generated as a result of flow instability (Nikora 1999).

The spectra from the feeding behavior did not show power declines at wavenumber ranges lower than $L^{-1} = 5.8$ cpm (Fig. 5.6). Although only a single turbulence microstructure profile was made during feeding behavior, spectral shapes obtained simultaneously by 2 turbulent shear probes indicate that there was no power decline even in the inertial subrange. This suggests that the energy-containing scale was the same as or larger than the school thickness of ~1 m (Fig. 5.8B, Table 5.1). On the other hand, there was a discrepancy between the spectra (Fig. 5.6A,B), which clearly shows that the flow field was not isotropic. This anisotropic turbulence may be caused by the anisotropic swimming pattern produced by the feeding school.

Catton et al. (2011) conducted a small tank experiment to study fluid motion around swimming krill using laser sheet illumination. They reported that krill aggregations actively transferred water parcels down to successive group members, consequently disturbing the water column at a scale of aggregations. Although fluid motions around krill and sardines are different, we speculate that the sardines' synchronous long-lasting group motions generate turbulent eddies larger than their individual body size (Fig. 5.8B).

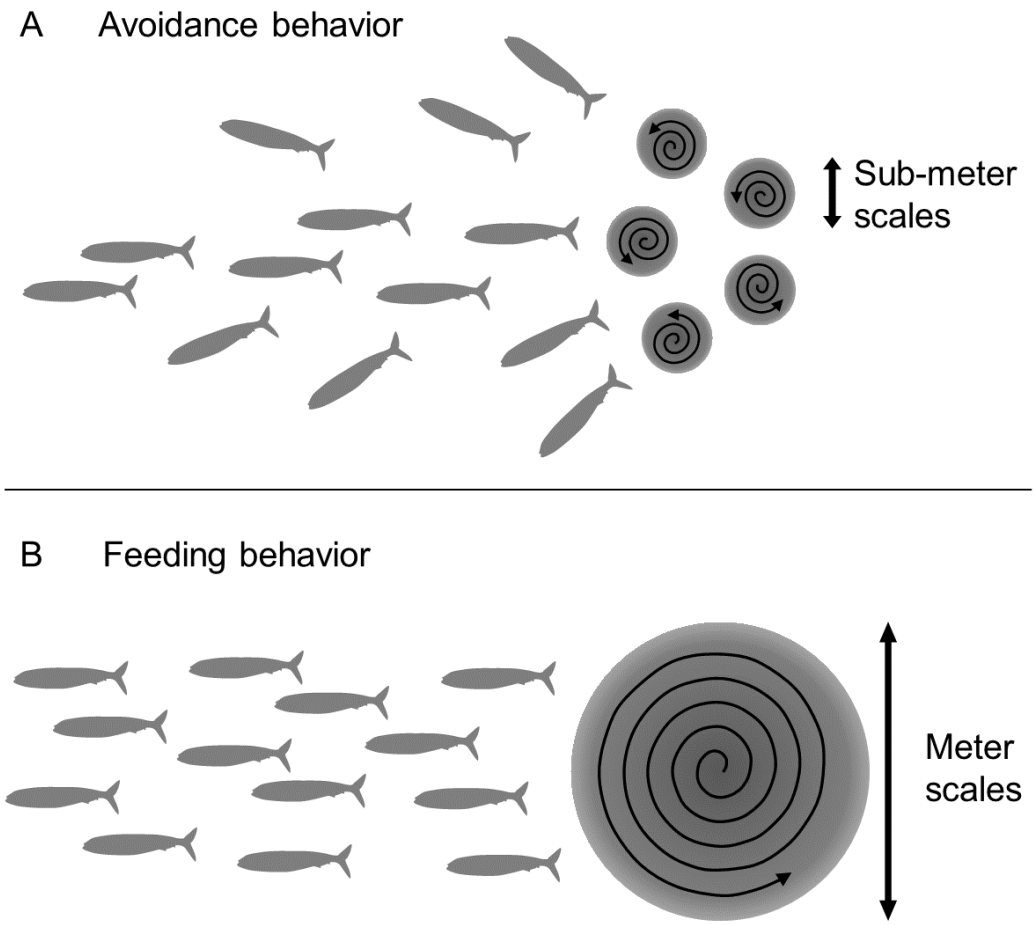

Fig. 5.8. Relationship between fish school behavior and size of school-generated turbulent eddy. (A) Turbulent eddies generated by a school displaying a quick and non-continuous motion, such as avoidance behavior, have the same size as individual body size. (B) Turbulent eddies generated by a school displaying a fast and long-lasting motion, such as particulate-feeding, have the same size as the school.

5.4.5 Mixing efficiency and eddy diffusivity

Based on results from the nearly homogeneous tank experiment, which suggest that sardines are able to generate eddies as large as their school size and as small as their body size, and assuming that these results are applicable in the stratified ocean, we estimate plausible values of the efficiency factor Γ and vertical eddy diffusivity of density K_ρ in the ocean, where Γ is a ratio between buoyancy destruction rate and turbulent kinetic energy dissipation rate, and is generally upper bounded by $\Gamma = 0.2$ (Osborn 1980). Visser (2007) pointed out that when Γ is low, turbulence scarcely contributes to mixing even if turbulent kinetic energy dissipation rates are high. He estimated that Γ does not exceed 0.01, when turbulence is generated by an individual small swimmer (~1 cm). However, his assumption does not take into account the effects of group motions, which can be effective as indicated by Catton et al. (2011) and this study. Following the model by Osborn (1980), K_ρ is expressed as:

$$K_\rho = \Gamma \frac{\varepsilon}{N^2}, \tag{5.8}$$

where N is the buoyancy frequency. Smyth et al. (2001) showed that Γ may be approximated as:

$$\Gamma \sim 0.33 \left(\frac{L_T}{L_O}\right)^{0.63}, \tag{5.9}$$

where L_T is the Thorpe scale, representing an overturning scale, and L_O is the Ozmidov scale, $L_O = (\varepsilon / N^3)^{1/2}$, which is the largest turbulent eddy size in a stratified water column. Measured ε caused by the sardine school varied between 8.2×10^{-5} and 5.2×10^{-4} W kg^{-1}. Generally, $N = 1 \times 10^{-2}$ to 3×10^{-2} s^{-1} in the stratified ocean (Thorpe 2007). Based on our results, the overturning scale by sardines is as small as their individual body size, and as large as their school thickness (Fig. 5.8). First, we assume that the overturning scale is similar to the thickness of the school, $L_T \sim 1$ m (Fig. 5.8B). Using all ranges of ε and N, we obtain $\Gamma = 0.05$ to 0.23 and $K_\rho = 2.1 \times 10^{-2}$ to 2.4×10^{-1} m^2 s^{-1}. The estimated Γ can reach $\Gamma = 0.2$, as in Osborn (1980). On the other hand, when the overturning scale is assumed to be individual body size $L_T \sim L = 0.173$ m (Fig. 5.8A), we obtain $\Gamma = 0.02$ to 0.08 and $K_\rho = 7.0 \times 10^{-3}$ to 7.9×10^{-2} m^2 s^{-1}. The estimated Γ is in a range consistent with Visser (2007). Regardless of the assumptions of L_T, the

estimated K_ρ range is noticeably high when compared with $K_\rho = 10^{-4}$ to 10^{-3} $\mathrm{m^2\,s^{-1}}$ measured in a highly tidally mixed channel (e.g. Kokubu et al. 2013). These rough estimates of mixing efficiency and diffusivities are based on the assumption that the sardine school can generate large energy-containing eddies in a stratified ocean, the same as that in the nearly homogeneous tank experiment. Note, however, that because stratification can support internal waves and suppress turbulent eddies, the scale of the eddies could be smaller than that found in this study.

5.4.6 Implications of large-scale mixing

While the results from this study contain uncertainty due to the small number of samples, we provide a rough estimate of sardine impact on ocean mixing at scales of local seas. We consider a case off the west coast of the United States where mixing processes and sardine biomass are well studied. We assume that the results from our study are applicable to Pacific sardine *Sardinops sagax*, whose characteristics such as body shape, body length, and wet weight, are similar to *S. melanostictus* (Whitehead 1985). The estimated biomass of *S. sagax* off the west coast of the USA is roughly 1 million t, where the area under consideration is 400 000 $\mathrm{km^2}$, and standard length and wet weight of the sardine are 0.20 m and 0.10 kg on average (Hill et al. 2014). Based on average wet weight and estimated biomass, the population abundance is roughly 10^{10} individuals. We now assume that all the individuals form schools whose dimensions are roughly 100 to 300 $\mathrm{m^2}$ in area and 5 to 10 m in height for each school (Castillo & Robotham 2004), and that the distribution of the individuals form hexagonal close-packing of equal spheres, whose radius is equal to the average body length $r \sim 0.20$ m (see Eqs. 5.A4 & 5.A5 in '5.6.2 Estimation of $n\,/\,V$'): the population density is approximately 22.1 ind. $\mathrm{m^{-3}}$. Dividing population abundance by population density, the total volume of the schools is 4.5×10^8 $\mathrm{m^3}$, which can be converted to mass by multi plying typical seawater density in the upper 100 m in the ocean, 1028 kg $\mathrm{m^{-3}}$ (Thorpe 2005). Thus, the total water mass that the schools occupy is 4.7×10^{11} kg. Multiplying the total water mass by turbulent kinetic energy dissipation rates with a range of $\varepsilon \sim 10^{-5}$ to 10^{-4} $\mathrm{W\,kg^{-1}}$, where we use a lower limit as reported by Gregg & Horne (2009) and an upper limit as measured in this study, the total kinetic energy dissipation is 4.7 to 47.0 MW. This estimation is comparable with or higher than the kinetic energy dissipation of 8.3 MW generated by internal wave breaking in the Monterey Canyon (Jachec et al. 2006), where diapycnal turbulent mixing actively occurs (Kunze et al. 2002).

Therefore, biomixing may not be negligible in certain parts of the world ocean.

5.5 Conclusion

We successfully collected microstructure data from inside a school of Japanese sardines *Sardinops melanostictus* in an aquarium tank where we were able to 'watch' sequences of biomixing. The average turbulent kinetic energy dissipation rate inside the school was $\varepsilon = 2.3 \times 10^{-4}\,\mathrm{W\,kg^{-1}}$, while $\varepsilon = 6.7 \times 10^{-6}\,\mathrm{W\,kg^{-1}}$ was the average background value outside the school. Our experiment using video cameras first revealed that the fishes exhibited avoidance behavior to the approaching microstructure profiler, suggesting that it is very challenging to measure true biologically induced turbulence without any artificial influences. Most of the turbulence measurements inside the sardine school were the result of the fish undergoing short bursts of speed in an effort to avoid the oncoming profiler. On the other hand, the school exhibited relatively fast and long-lasting synchronized swimming when they were being fed. Here, their swimming behavior was dominated by feeding motions, whereas the school manifested avoidance behavior in regard to the profiler, keeping about 1 m from the instrument. Turbulent shear spectra for the avoidance behavior showed a power decline in the lower ($< L^{-1}$) wavenumber ranges against the Nasmyth spectrum, consistent with Gregg & Horne (2009), while spectra for the feeding behavior exhibited no power decline, similar to physically induced turbulence. For the avoidance case, the largest scale of turbulent kinetic energy that the sardine could produce was roughly its individual body size L, consistent with Visser (2007). On the other hand, the largest scale was at least 1 m, as large as the sardine school thickness of approximately 1 m, for the feeding case. However, at the level of turbulent kinetic energy dissipation rates, there was no noticeable difference between avoidance behavior and feeding behavior. Although the results from this study contain some uncertainty due to the small number of deployments, the data clearly show that fish schools are able to generate turbulent eddies as large as their school thickness and cause efficient turbulent mixing similar to naturally occurring turbulence.

Chapter 6

Conclusion and outlook

6.1 Conclusion

The field data obtained from the cabled observatory (OCEANS) in Izu-Oshima Island revealed the evidence that zooplankton avoid elevated currents and subsequent turbulence. The plankton camera (CPICS) detected 17 zooplankton taxa, in which 9 taxa appeared only during night time (strong migrator), 6 taxa appeared at both during day time and night time but preferred night time (moderate migrator). The last 2 taxa were non-motile. The strong migrators were mostly composed of demersal zooplankton, such as Ostracoda and Mysida. The moderate migrators were mostly composed of pelagic zooplankton, such as Calanoida and Larvacea. The acoustic backscatter signals obtained from Aquadopp were positively correlated with the migrator abundance (r^2 = 0.39 to 0.50, $p<0.01$; depending on the layer). The optic backscatter signals measured by a turbidity sensor also showed positive correlation with the migrator abundance (r^2 = 0.79, $p<0.01$). Abundance of the strong migrator showed negative correlation with wave orbital velocity (r^2 = 0.32, $p<0.01$), current velocity (r^2 = 0.20, $p<0.01$), and near-bed turbulence (r^2 = 0.10, $p<0.01$). The negative correlations against the physical disturbances were found in both the acoustic and the optic backscatters during night time in summer and fall. Day-time abundance of the moderate migrator also showed negative correlation with wave orbital velocity (r^2 = 0.08, $p<0.01$), where the low correlation may be due to the low number of the samples. Since the strong migrator (about 70% of zooplankton) was mostly demersal zooplankton, it was suggested that near-bed hydrodynamic disturbances prevented their migration from the bottom and consequently suppressed their DVM.

While the zooplankton avoidance against ambient flow disturbance was clearly shown by the filed data, additional field observations were carried out using

only acoustic instruments. The purposes of the experiments were 1) to confirm reproducibility of the avoidance phenomenon and 2) to eliminate a potential bias due to positive phototaxis of zooplankton against visible light from optic sensors (e.g. the turbidity/fluorescence sensor, the plankton camera). Two ADCP moorings data sets were used in this study: one near Izu-Oshima Island and the other off Eilat, Israel. Both data sets consistently showed that the acoustic backscatter intensity increased during night time. Only signals from zooplankton were extracted by using a newly developed special filter which utilized the differences among backscatter intensities from each beam. The acoustic backscatter signals from the both sites were significantly reduced when current velocity increased. The trends found at the both sites were surprisingly similar, while the two sites were physically separated and had very different environments. This consistency indicates that the generality of zooplankton avoidance against increased current velocity.

The influence of zooplankton aggregation due to positive phototaxis on the turbidity data was confirmed by the laboratory tank experiments. The experiments showed that zooplankton individuals were attracted by visible light emitted from a fluorescence sensor, and the optic backscatter signals from zooplankton individuals appeared as elevated turbidity. When currents were artificially generated in the tank individuals actively aggregated toward accumulated around the light source were flushed away. The turbidity data were negatively correlated with the current velocity ($r^2 = 0.40$, $p<0.01$). Hence, the negative correlations found by the cabled observatory may be simply explained by the phototactic behavior. However, given the results from the ADCP filed data, the suppression of zooplankton DVM due to ambient currents and turbulence should real.

Turbulence generated from sardine school was confirmed by a large tank experiment. Turbulence kinetic energy dissipation rates were significantly increased in the sardine school (2.3×10^{-4} W kg^{-1} on average), where the background dissipation rate in the tank was 6.7×10^{-6} W kg^{-1} on average. When the sardines showed a quick and non-continuous motion to avoid the instrument, the turbulent shear spectra had a power decline at the low wavenumbers (large scales), suggesting the school did not input kinetic energy in the large scales. On the other hand, when the sardines showed a fast and long-lasting motion for feeding, the turbulent shear spectra followed the Nasmyth empirical spectra, suggesting the school input kinetic energy in the scales larger than the individual sardine. The results suggest that biomixing by fish school potentially contribute to the ocean mixing.

There have never been comprehensive discussions on the interactions

between animals and flows in the ocean, while each phenomenon (e.g. biomixing, turbulence avoidance of zooplankton) has been studied separately. Based on the results from this study and previous studies, the interactions are here summarized (Fig. 6.1). Large animals, such as pelagic fishes, generate turbulent eddies during their biological activities (swimming, feeding, mating) (Fig. 6.1). While the disturbance by the animals have been recognized as a negligible source for the ocean mixing (Visser 2007), this study first time suggested that a fish school can generate eddies large enough to induce significant mixing (Chapter 5). The fish-generated turbulence may cause non-trivial mixing in the coastal regions where their population is generally large (Fig. 6.1).

Microscale turbulence generated by both biological and physical processes is always accompanied by microscale water deformation that is detectable by zooplankton (Kiørboe 2008). When zooplankton sense water deformations, they generally show avoidance reactions (Chapters 2 and 3) (Seuront et al. 2004, Gallager et al. 2004, Kiørboe 2008). High levels of ambient turbulence diminish the probability of the reproduction of an individual zooplankton (Visser et al. 2009). Hence, the avoidance is always reasonable even if the individual zooplankton cannot distinguish whether turbulence was induced by predator (fish) or not (Fig. 6.1). This study first time suggested that this individual-based strategy (avoidance) by zooplankton changes their spatial distribution and consequently modifies their DVM (Chapters 2 and 3). On the other hand, a recent study demonstrated that vertical migrations by zooplankton aggregation generate turbulence and mix up the water column (Houghton et al. 2018).

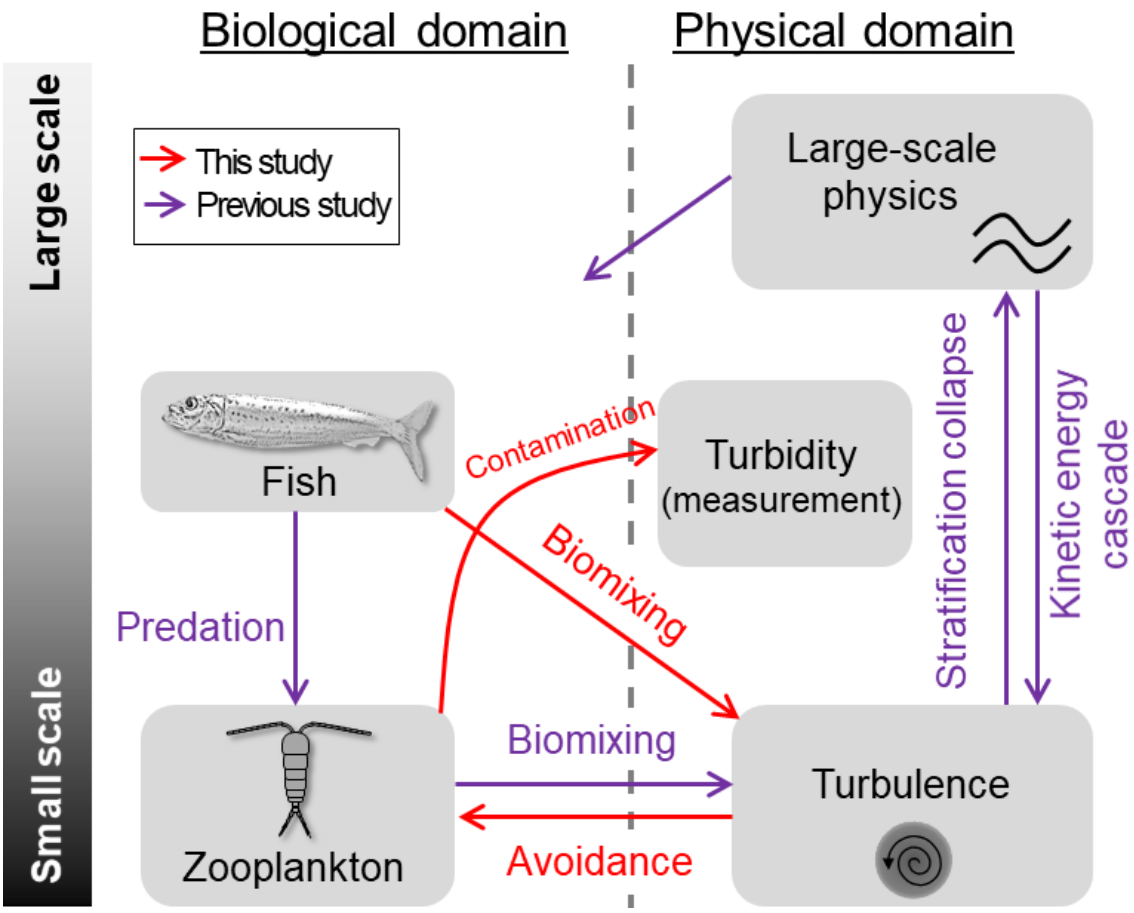

Fig. 6.1. A schematic summarizing the interactions between marine animals and physical phenomena, based on the results from this study (red arrows) and previous studies (black arrows).

6.2 Outlook

A newly developed cabled observatory with a novel plankton camera was used in this study, and the observed data provided new knowledges about the interactions between marine animals and environmental flow fields. Turbidity/fluorescence sensor is widespread and used for the purposes of coastal engineering and environmental assessment; the biological effect on turbidity data will be an important technical issue. Mooring systems and cabled observatories are important technics to observe ocean ecology and surrounding environment simultaneously for long time and find new biological phenomena as presented in Chapter 2 and 3. To observe natural biological conditions, we need to devise how to use optical sensors (fluorescence sensors, underwater cameras) in the ocean; for example, use infrared light which is not visible by most marine animals, or measure fluorescence and turbidity after seawater suction inside instrument's body to hide light source from zooplankton. Quantifying biomixing by fish school as well as zooplankton aggregation would be important in understanding coastal physical processes. As shown in Chapter 5, marine animals would change their motion/behavior in response to instrument itself. Hence, fluid motions around animal bodies should be measured remotely, without disturbing their motion. Particle image velocimetry (PIV) successfully measured fluid motions around zooplankton swarm in previous studies but has not been used for fish school in the context of biomixing. Flexible uses of conventional instruments are expected to understand interactions between fluid and marine animals.

References

Ainslie MA, McColm JG (1998) A simplified formula for viscous and chemical absorption in sea water. The Journal of the Acoustical Society of America 103:1671

Al-mutairi H, Landry MR (2001) Active export of carbon and nitrogen at Station ALOHA by diel migrant zooplankton. Deep-Sea Research II 48:2083–2103

Bonicelli J, Tyburczy J, Tapia FJ, Finke GR, Parragué M, Dudas S, Menge BA, Navarrete SA (2016) Diel vertical migration and cross-shore distribution of barnacle and bivalve larvae in the central Chile inner-shelf. Journal of Experimental Marine Biology and Ecology 485:35–46

Buskey EJ, Swift E (1985) Behavioral responses of oceanic zooplankton to simulated bioluminescence. Biol Bull 168:263–275

Brierley AS, Fernandes PG, Brandon MA, Armstrong F, Millard NW, McPhail SD, Stevenson P, Pebody M, Perrett J, Squires M, Bone DG, Griffiths G (2002) Antarctic Krill Under Sea Ice: Elevated Abundance in a Narrow Band Just South of Ice Edge. Science 295:1890–1892

Brierley AS (2014) Diel vertical migration. Current Biology 24(22):R1074–R1076

Campos EJD, Velhote D, da Silveira ICA (2000) Shelf break upwelling driven by Brazil Current cyclonic meanders. Geophysical Research Letters 27(6):751–754

Capet X, McWilliams JC, Molemaker MJ, Shchepetkin AF (2008) Mesoscale to Submesoscale Transition in the California Current System. Part I: Flow Structure, Eddy Flux, and Observational Tests. Journal of Physical Oceanography 38:29–43

Carlson DF, Fredj E, Gildor H (2014) The annual cycle of vertical mixing and restratification in the Northern Gulf of Eilat/Aqaba (Red Sea) based on high temporal and vertical resolution

observations. Deep-Sea Research I 84:1–17

Castillo J, Robotham H (2004) Spatial structure and geometry of schools of sardine (*Sardinops sagax*) in relation to abundance, fishing effort, and catch in northern Chile. ICES J Mar Sci 61:1113–1119

Catton KB, Webster DR, Kawaguchi S, Yen J (2011) The hydrodynamic disturbances of two species of krill: implications for aggregation structure. J Exp Biol 214:1845–1856

Cherry RD, Higgo JJW, Fowler SW (1978) Zooplankton fecal pellets and element residence times in the ocean. Nature 274:246–248

Constantin S, Doxaran D, Constantinescu S (2016) Estimation of water turbidity and analysis of its spatio-temporal variability in the Danube River plume (Black Sea) using MODIS satellite data. Continental Shelf Research 112:14–30

Dam HG, Roman MR, Youngbluth MJ (1995) Downward export of respiratory carbon and dissolved inorganic nitrogen by diel-migrant mesozooplankton at the JGOFS Bermuda time-series station. Deep-Sea Research I 42(7):1187–1197

Dewar WK, Bingham RJ, Iverson RL, Nowacek DP, St. Laurent LC, Wiebe PH (2006) Does the marine biosphere mix the ocean? J Mar Res 64:541–561

Dickey T, Marra J, Granata T, Langdon C, Hamilton M, Wiggert J, Siegel D, Bratkovich A (1991) Concurrent High Resolution Bio-optical and Physical Time Series Observations in the Sargasso Sea During the Spring of 1987. Journal of Geophysical Research 96:8643–8663

Drost EJF, Lowe RJ, Ivey GN, Jones NL (2018) Wave-current interactions in the continental shelf bottom boundary layer of the Australian North West Shelf during tropical cyclone conditions. Continental Shelf Research 165:78–92

Echelman T, Fishelson L (1990) Surface zooplankton dynamics and community structure in the Gulf of Aqaba (Eilat), Red Sea. Marine Biology 107:179–190

Ferrari R, Wunsch C (2009) Ocean circulation kinetic energy: reservoirs, sources, and sinks. Annu Rev Fluid Mech 41:253–282

Flagg CN, Smith SL (1989) On the use of the Acoustic Doppler Current Profiler to measure zooplankton abundance. Deep-Sea Res 36:455–474

Fofonoff NP, Millard Jr. RC (1983) Algorithms for computation of fundamental properties of seawater. UNESCO Tech. Pap. mar. Sci. 44

Gallager SM, Yamazaki H, Davis CS (2004) Contribution of fine-scale vertical structure and swimming behavior to formation of plankton layers on Georges Bank. Mar Ecol Prog Ser 267:27–43

Garrido S, van der Lingen CD (2014) Feeding biology and ecology. In: Ganias K (ed) Biology and ecology of sardines and anchovies. CRC Press, Boca Raton, FL

Garrido S, Marçalo SA, Zwolinski J, van der Lingen CD (2007) Laboratory investigations on the effect of prey size and concentration on the feeding behaviour of *Sardina pilchardus*. Mar Ecol Prog Ser 330:189–199

Genin A, Lazar B, Brenner S (1995) Vertical mixing and coral death in the Red Sea following the eruption of Mount Pinatubo. Nature 377:507–510

Goda Y, Kudaka M (2007) On the role of spectral width and shape parameters in control of individual wave height distribution. Coastal Engineering Journal 49(3):311–335

Gregg MC, Horne JK (2009) Turbulence, acoustic backscatter, and pelagic nekton in Monterey Bay. J Phys Oceanogr 39:1097–1114

Grossmann MM, Gallager SM, Mitarai S (2014) Continuous monitoring of near-bottom mesoplankton communities in the East China Sea during a series of typhoons. J Oceanogr 71(1):115–124

Hara I (1987) Swimming speed of sardine school on the basis of aerial survey. Nippon Suisan Gakkai Shi 53:223–227

Hasegawa D, Yamazaki H, Lueck RG, Seuront L (2004) How islands stir and fertilize the upper ocean. Geophys Res Lett 31, L16303.1–4

Haury LR, Yamazaki H (1995) The dichotomy of scales in the perception and aggregation behavior of zooplankton. Journal of Plankton Research 17(1):191–197

Heidelberg KB, Sebens KP, Purcell JE (2004) Composition and sources of near reef zooplankton on a Jamaican forereef along with implications for coral feeding. Coral Reefs 23:263–276

Hill KT, Crone PR, Demer DA, Zwolinski J, Dorval E, Macewicz BJ (2014) Assessment of the pacific sardine resource in 2014 for U.S.A. management in 2014–15. In: NMFS SPO (ed) NOAA Technical Memorandum NMFS, 531. NOAA NMFS Offices and Science Centers, Seattle, WA

Hoerner SF (1965) Fluid-dynamic drag. Self-published, Midland Park, NJ

Holzman R, Ohavia M, Vaknin R, Genin A (2007) Abundance and distribution of nocturnal fishes over a coral reef during the night. Mar Ecol Prog Ser 342:205–215

Houghton IA, Koseff JR, Monismith SG, Dabiri JO (2018) Vertically migrating swimmers generate aggregation-scale eddies in a stratified column. Nature 556:497–500

Huntley ME, Zhou M (2004) Influence of animals on turbulence in the sea. Mar Ecol Prog Ser 273:65–79

Incze LS, Hebert D, Wolff N, Oakey N, Dye D (2001) Changes in copepod distributions associated with increased turbulence from wind stress. Mar Ecol Prog Ser 213:229–240

Jachec SM, Fringer OB, Gerritsen MG, Street RL (2006) Numerical simulation of internal tides and the resulting energetics within Monterey Bay and the surrounding area. Geophys Res Lett 33:L12605.1–4

Jafar-Sidik M, Gohin F, Bowers D, Howarth J, Hull T (2017) The relationship between Suspended Particulate Matter and Turbidity at a mooring station in a coastal environment: consequences for satellite-derived products. Oceanologia 59(3):365–378

Jékely G, Colombelli J, Hausen H, Guy K, Stelzer E, Nédélec F, Arendt D (2008) Mechanism

of phototaxis in marine zooplankton. Nature 456:395–399

Katija K, Dabiri JO (2009) A viscosity-enhanced mechanism for biogenic ocean mixing. Nature 460:624–626

Katija K (2012) Biogenic inputs to ocean mixing. The Journal of Experimental Biology 215:1040–1049

Kiørboe T (2008) A mechanistic approach to plankton ecology. Princeton: Princeton University Press

Kiørboe T (2013) Attack or Attacked: The Sensory and Fluid Mechanical Constraints of Copepods' Predator–Prey Interactions. Integrative and Comparative Biology 53(5): 821–831

Kokubu Y., Yamazaki H, Nagai T, Gross ES (2013) Mixing observations at a constricted channel of a semi-closed estuary: Tokyo Bay. Cont Shelf Res 69:1–16

Kunze E, Rosenfeld LK, Carter GS, Gregg MC (2002) Internal waves in Monterey Submarine Canyon. J Phys Oceanogr 32:1890–1913

Kunze E, Dower JF, Beveridge I, Dewey R, Bartlett KP (2006) Observations of biologically generated turbulence in a coastal inlet. Science 313:1768–1770

Kunze E (2011) Fluid mixing by swimming organisms in the low-Reynolds-number limit. Journal of Marine Research 69:591–601

Kunze E (2019) Biologically generated mixing in the ocean. Annual Review of Marine Science 11:215–226

Lienesch PW, Matthews WJ (2000) Daily fish and zooplankton abundances in the littoral zone of Lake Texoma, Oklahoma-Texas, in relation to abiotic variables. Environmental Biology of Fishes 59:271–283

Lindell D, Post AF (1995) Ultraphytoplankton succession is triggered by deep winter mixing in the Gulf of Aqaba (Eilat), Red Sea. Limnol Oceanogr 40(6):1130–1141

Loperfido JV, Just CL, Papanicolaou AN, Schnoor JL (2010) In situ sensing to understand diel turbidity cycles, suspended solids, and nutrient transport in Clear Creek, Iowa. Water Resources Research 46:W06525

Lopes RM (1994) Zooplankton distribution in the Guaraú River estuary (south-eastern Brazil). Estuarine, Coastal and Shelf Science 39(3):287–302

Lorke A, Probst WN (2010) In situ measurements of turbulence in fish shoals. Limnol Oceanogr 55:354–364

Ma X, Johnson KB (2017) Comparative phototaxis of calanoid and harpacticoid copepods. Mar Biol 164:26

MacKenzie BR, Kiørboe T (2000) Larval fish feeding and turbulence: a case for the downside. Limnology and Oceanography 45(1):1–10

Mackie GO, Mills CE (1983) Use of the Pisces IV submersible for zooplankton studies in coastal waters of British Columbia. Can J Fish Aquat Sci 40:763–776

Manasrah R, Raheed M, Badran MI (2006) Relationships between water temperature, nutrients and dissolved oxygen in the northern Gulf of Aqaba, Red Sea. Oceanologia 48(2):237–253

Masunaga E, Fringer OB, Kitade Y, Yamazaki H, Gallager SM (2017) Dynamics and Energetics of Trapped Diurnal Internal Kelvin Waves around a Midlatitude Island. Journal of Physical Oceanography 47:2479–2498

McManus MA, Cheriton OM, Drake PJ, Holliday DV, Storlazzi CD, Donaghay PL, Greenlaw CF (2005) Effects of physical processes on structure and transport of thin zooplankton layers in the coastal ocean. Mar Ecol Prog Ser 301:199–215

McPhee-Shaw EE, Sternberg RW, Mullenbach B, Ogston AS (2004) Observations of intermediate nepheloid layers on the northern California continental margin. Continental Shelf Research 24:693–720

Meester LD, Dumont HJ (1989) Phototaxis in *Daphnia*: Interaction of hunger and genotype.

Limnol Oceanogr 34(7):1322–1325

Melo PAMC, Silva TA, Neumann-Leitão S, Schwamborn R, Gusmão LMO, Porto Neto F (2010) Demersal zooplankton communities from tropical habitats in the southwestern Atlantic. Marine Biology Research 6:530–541

Misund OA, Coetzee JC, Fréon P, Gardener M, Olsen K, Svellingen I, Hampton I (2003) Schooling behavior of sardine *Sardinops sagax* in False Bay, South Africa. Afr J Mar Sci 25:185–193

Monismith SG, Genin A (2004) Tides and sea level in the Gulf of Aqaba (Eilat). Journal of Geophysical Research 109:C04015

Munk WH (1966) Abyssal recipes. Deep-Sea Research 13:707–730

Nikora V (1999) Origin of the "-1" spectral law in wall-bounded turbulence. Phys Rev Lett 83:734–736

Noss C, Lorke A (2012) Zooplankton induced currents and fluxes in stratified waters. Water Quality Research Journal 47:276–286

Oakey NS, Elliott JA (1982) Dissipation within the surface mixed layer. J Phys Oceanogr 12:171–185

Osborn TR (1980) Estimates of the local rate of vertical diffusion from dissipation measurements. J Phys Oceanogr 10:83–89

Patria M, Wiese K (2004) Swimming in formation in krill (Euphausiacea), a hypothesis: dynamics of the flow field, properties of antennular sensor systems and a sensory–motor link. Journal of Plankton Research 26(11):1315–1325

Price JF, Mooers CNK, van Leer JC (1978) Observation and simulation of storm-induced mixed-layer deepening. Journal of Physical Oceanography 8:582–599

Pujiana K, Moum JN, Smyth WD, Warner SJ (2015) Distinguishing ichthyogenic turbulence from geophysical turbulence. Geophysical Research: Oceans 120:3792–3084

Reidenbach MA, Monismith SG, Koseff JR, Yahel G, Genin A (2006) Boundary layer turbulence and flow structure over a fringing coral reef. Limnol Oceanogr 51(5):1956–1968

Rice SP, Johnson MF, Mathers K, Reeds J, Extence C (2016) The importance of biotic entrainment for base flow fluvial sediment transport. Journal of Geophysical Research:Earth Surface 121(5):890–906

Ross T, Lueck R (2005) Estimating turbulent dissipation rates from acoustic backscatter. Deep Sea Res I 52:2353–2365

Rothschild BJ, Osborn TR (1988) Small-scale turbulence and plankton contact rates. Journal of Plankton Research 10:465–474

Rousseau S, Kunze E, Dewey R, Bartlett K., Dower J (2010) On turbulence production by swimming marine organisms in the open ocean and coastal waters. J Phys Oceanogr 40:2107–2121

Saita T, Shiki S, Tai A, Shigeta S, Yano S, Komatsu T (2009) Evaluation of vertical mixing by *in situ* measurements off the coast of shimabara peninsula, JSCE Proceedings of Hydraulic Engineering 53:1471–1476

Sanders R, Henson SA, Koski M, De La Rocha CL, Painter SC, Poulton AJ, Riley J, Salihoglu B, Visser A, Yool A, Bellerby R, Martin AP (2014) The Biological Carbon Pump in the North Atlantic. Progress in Oceanography 129:200–218

Sarmiento JL, Gruber N. (2006) Carbon cycle CO_2, and climate. In *Ocean Biogeochemical Dynamics*, pp. 392–457. Princeton, NJ: Princeton Univ. Press

Sato M, Klymak JK, Kunze E, Dewey R, Dower JF (2014) Turbulence and internal waves in Patricia Bay, Saanich Inlet, British Columbia. Cont Shelf Res 85:153–167

Sengupta A, Carrara F, Stocker R (2017) Phytoplankton can actively diversify their migration strategy in response to turbulent cues. Nature 543:555–558

Seuront L, Yamazaki H, Souissi S (2004) Hydrodynamic Disturbance and Zooplankton

Swimming Behavior. Zoological Studies 43(2):376–387

Shanks AL, MacMahan J, Morgan SG, Reniers AJHM, Jarvis M, Brown J, Fujimura A, Griesemer C (2015) Transport of larvae and detritus across the surf zone of a steep reflective pocket beach. Mar Ecol Prog Ser 528:71–86

Shay T J, Gregg MC (1986) Convectively driven turbulent mixing in the upper ocean. J Phys Oceanogr 16:1777–1798

Simmons SM, Parsons DR, Best JL, Orfeo O, Lane SN, Kostaschuk R, Hardy RJ, West G, Malzone C, Marcus J, Pocwiardowski P (2010) Monitoring suspended sediment dynamics using MBES. Journal of Hydraulic Engineering 136(1):45–49

Simoncelli S, Thackeray SJ, Wain DJ (2018) On biogenic turbulence production and mixing from vertically migrating zooplankton in lakes. Aquatic Sciences 80:35

Smyth WD, Moum JN, Caldwell DR (2001) The efficiency of mixing in turbulent patches: inferences from direct simulations and microstructure observations. J Phys Oceanogr 31:1969–1992

Sommer U, Berninger UG, Böttger-Schnack R, Cornils A, Hagen W, Hansen T, Al-Najjar T, Post AF, Schnack-Schiel SB, Stibor H, Stübing D, Wickham S (2002) Grazing during early spring in the Gulf of Aqaba and the northern Red Sea. Mar Ecol Prog Ser 239:251–261

Soulsby RL (1995) Bed shear-stresses due to combined waves and currents. In: Advances in coastal morphodynamics 4 Delft Hydraulics Delft (pages 4–23 to 4–23)

Soulsby RL (2006) Simplified Calculation of Wave Orbital Velocities. HR Wallingford Ltd., Wallingford, U. K

Sprules WG, Stockwell JD (1995) Size-based biomass and production models in the St Lawrence Great Lakes. J. Mar. Sci. 52:705–710

Steinberg DK, Landry MR (2017) Zooplankton and the ocean carbon cycle. Annu Rev Mar Sci 9:413–444

Storz UC, Paul RJ (1998) Phototaxis in water fleas (*Daphnia magna*) is differently influenced by visible and UV light. J Comp Physiol A 183:709–717

Stukel MR, Ohman MD, Benitez-Nelson CR, Landry MR (2013) Contributions of mesozooplankton to vertical carbon export in a coastal upwelling system. Mar Ecol Prog Ser 491:47–65

Swart DH (1974) Offshore sediment transport and equilibrium beach profiles. Delft Hydraul. Lab. Publ. No. 131.

Takata H, Kuma K, Isoda Y, Otosaka S, Senjyu T, Minagawa M (2008) Iron in the Japan Sea and its implications for the physical processes in deep water. Geophysical Research Letters 35:L02606

Tanaka M, Nagai T, Okada T, Yamazaki H (2017) Measurement of sardine-generated turbulence in a large tank. Mar Ecol Prog Ser 571:207–220

Thorpe SA (2005) The turbulent ocean, Cambridge University Press, Cambridge

Thorpe SA (2007) An introduction to ocean turbulence, Cambridge University Press, Cambridge

Tranter DJ, Bulleid NC, Campbell R, Higgins HW, Rowe F, Tranter HA, Smith DF (1981) Nocturnal Movements of Phototactic Zooplankton in Shallow Waters. Marine Biology 61:317–326

Trowbridge JH (1998) On a technique for measurement of turbulent shear stress in the presence of surface waves. Journal of Atmospheric and Oceanic Technology 15(1):290–298

UNESCO (1981) Tenth report of the joint panel on oceanographic tables and standards. UNESCO Tech Pap Mar Sci 36, UNESCO, Paris, p 25

van den Lingen CD (1994) Effect of particle size and concentration of the feeding behavior of adult pilchard *Sardinops sagax*. Mar Ecol Prog Ser 109:1–13

van den Bremer TS, Breivik Ø (2017) Stokes drift. Phil. Trans. R. Soc. A 376:20170104

Vanhaecke P, Tackaert W, Sorgeloos P (1987) The biogeography of *Artemia*: an updated review. Artemia research and its applications, Vol. 1. Morphology, genetics, strain characterization, toxicology (ed. by P. Sorgeloos, D.A. Bengtson, W. Decleir and E. Jaspers), pp. 129–155. Universa Press, Wetteren, Belgium.

Visser AW, Saito H, Saiz E, Kiørboe T (2001) Observations of copepod feeding and vertical distribution under natural turbulent conditions in the North Sea. Marine Biology 138:1011–1019

Visser AW (2007) Biomixing of the oceans? Science 316:838–839

Visser AW, Mariani P, Pigolotti S (2009) Swimming in turbulence: zooplankton fitness in terms of foraging efficiency and predation risk. Journal of Plankton Research 31(2):121–133

Wardle CS, Soofiani NM, O'Neill FG, Glass CW, Johnstone ADF (1996) Measurements of aerobic metabolism of a school of horse mackerel at different swimming speeds. J Fish Biol 49:854–862

Weihs D (1977) Effects of size on sustained swimming speeds of aquatic organisms. In: Pedley TJ (ed) Scale effects in animal locomotion. Academic Press, New York, p 333–338

Whitehead PJP (1985) Clupeoid fishes of the world. part I - Chirocentridae, Clupeidae and Pristigasteridae. FAO, Rome

Wiberg PL, Sherwood CR (2008) Calculating wave-generated bottom orbital velocities from surface-wave parameters. Computers & Geosciences 34:1243–1262

Wiles PJ, Rippeth TP, Simpson JH, Hendricks PJ (2006) A novel technique for measuring the rate of turbulent dissipation in the marine environment. Geophysical Research Letters 33:L21608

Wilhelmus MM, Dabiri JO (2014) Observations of large-scale fluid transport by laser-guided plankton aggregations. Physics of fluids 26:101302

Wunsch (2002) What is the thermohaline circulation? Science 298:1179–1181

Yahel R, Yahel G, Berman T, Jaffe JS, Genin A (2005) Diel pattern with abrupt crepuscular changes of zooplankton over a coral reef. Limnol Oceanogr 50(3):930–944

Yamazaki H, Osborn TR, Squires KD (1991) Direct numerical simulation of planktonic contact in turbulent flow. Journal Plankton Research 13(3):629–643

Yamazaki H, Squires KD (1996) Comparison of oceanic turbulence and copepod swimming. Mar Ecol Prog Ser 144:299–301

Yurista PM, Yule DL, Balge M, VanAlstine JD, Thompson JA, Gamble AE, Hrabik TR, Kelly JR, Stockwell JD, Vinson MR (2014) A new look at the Lake Superior biomass size spectrum. Can. J. Fish. Aquat. Sci. 71:1324–1333

Zhang X, Dam HG (1997) Downward export of carbon by diel migrant mesozooplankton in the central equatorial Pacific. Deep-Sea Research II 44:2191–2202

Zhu X, Takasugi Y, Nagao M, Hashimoto E (2000) Diurnal cycle of sound scatters and measurements of turbidity using ADCP in Beppu Bay. Journal of Oceanography 56:559–565